Title
Spatially Resolved Charge Transfer in Molecular Nanostructures at the Surface of Gate Tunable Graphene Devices

Author
Tsai, Hsinzon

Publication Date
2017

Peer reviewed|Thesis/dissertation

Spatially Resolved Charge Transfer in Molecular Nanostructures at the Surface of Gate Tunable Graphene Devices

by

Hsin-Zon Tsai

A dissertation submitted in partial satisfaction of the

requirements for the degree of

Doctor of Philosophy

In

Physics

in the

Graduate Division

of the

University of California, Berkeley

Committee in charge:
Professor Michael F. Crommie, Chair
Professor Feng Wang
Professor Junqiao Wu

Fall 2017

Spatially Resolved Charge Transfer in Molecular Nanostructures at the Surface of Gate Tunable Graphene Devices

by

Hsin-Zon Tsai

Abstract

Spatially Resolved Charge Transfer Molecular Nanostructures at the Surface of a Gate Tunable Graphene Device

By

Hsin-Zon Tsai

Doctor of Philosophy in Physics

University of California, Berkeley

Professor Michael F. Crommie, Chair

The ability to modify the electronic properties of monolayer graphene via charge-donating or charge-accepting molecules creates new opportunities for fabricating nano-scale hybrid devices. Introducing donor and acceptor molecules to a graphene surface induces charge transfer and creates localized Coulomb potentials. Combined with an electrostatic back-gate on a graphene/BN device, it is possible to engineer a variety of electrostatic potentials for studying fundamental electronic phenomena. In this dissertation, we discuss local probe investigation of such phenomena in graphene/molecule hybrid systems using scanning tunneling microscopy and atomic force microscopy.

We first describe the procedures for fabricating atomically clean graphene/BN field effect transistors (FETs) for molecular self-assembly and local probe studies. Using these graphene/BN FETs, we are able to adjust the energy alignment of aromatic molecular orbital levels with respect to the Fermi level. These molecules are weakly coupled to the graphene and show clear vibronic resonances in their energy spectra. By choosing a more electronegative molecule, fluorinated TCNQ, with orbital levels closer to the Dirac point, we are able to demonstrate charge-state switching in single molecules. The electric field-induced energy shift of the molecular levels is influenced here by gate-dependent screening effects arising from the graphene substrate. Additionally, we find that inert fatty acid islands deposited on the surface can help to stabilize single molecules for local probe characterization.

Such control of single molecules on a device surface allows us to create more complex self-assembled molecular nanostructures using bottom up techniques. Inert fatty acid islands, for example, are used to act as a template for the self-assembly of one-dimensional molecular arrays. These arrays are electrically charged by applying an electrostatic back-gate to the graphene/BN FET, thus generating strong one-dimensional Coulomb potentials. Such Coulomb potentials are

found to induce new localized Dirac fermion states. The formation of these states are explained by an atomic collapse picture whereby an electron cannot form stable bound states around an isolated Coulomb potential, but rather spirals inward toward the center of the impurity. Self-assembly processes also lead to the formation of densely-packed, charged two-dimensional molecular islands on the graphene surface. The formation mechanism of these islands is explained by work function heterogeneity on the surface, a mechanism unique to poorly screened substrates like graphene. This work reveals new fundamental behavior for Coulomb potentials anchored to graphene surfaces at different length scales and geometries, enabling the engineering of 2D potential landscapes and electron wave-functions in graphene devices.

To my parents.

Contents

List of Figures

Acknowledgments

This dissertation would not have been possible without the help of many people. First, I would like to thank my adviser Professor Mike Crommie for supporting me during my graduate study. He has taught me how to think about problems with intuitive physical pictures and he has been very patient in training me to present my thoughts in public speaking and scientific writing. Also, he has given me a lot of opportunities and resources to try and explore new research directions.

I would also like to express my special thanks to Alexander Riss, Sebastian Wickenburg, Jiong Lu and Arash Alahgholipour Omrani. Alexander Riss has strong scientific instinct. I have learned how to ask the right questions from him. Sebastian Wickenburg is a very organized and careful person. He has taught me how to analyze research problems in detail. Jiong Lu has extensive knowledge of surface science and experimental design. He has shown me how to find the proper resources to solve problems. Arash Alagholipour Omrani is good at handson works and designing tools for experiments. His experience in fabrication and instrumentation has helped me a lot in improving experimental setup.

Miguel Moreno Ugeda, Jairo Velasco Jr., Aaron Bradley, Kacey Meaker, Dillon Wong, Juwon Lee Giang D Nguyen, Zahra Pedramrazi, Chen Chen, Yi Chen, Dan Rizzo, Franklin Liou, and Andrew Shunichi Aikawa have helped me overcome various experimental and theoretical challenges. Many undergraduate students have made contribution to device fabrication including Salman Kahn, Griffin Fischer Rodgers, Patrick Forrester, Yi-Shiou Duh, Jin Chen, Youngkyou Kim, Won-Woo Choi, and Chad Germany. Many visitors also provided help in sample preparation including Erik Piatti, Jakob Jørgensen, Yun Zhou, Sergio Pezzini, Sajjad Tollabimazraehno, and Caihong Jia.

The work presented in this dissertation involved extensive and stimulating collaboration with chemists and theorists. Professor Felix Fischer and his group members helped synthesize charge transfer molecules for UHV deposition on graphene. Professor Steven Louie and his group members Liang Z. Tan and Johannes Lischner helped us interpret our experimental data in molecular nanostructures. Professor Marvin Cohen and his group member Sinisa Coh, Hyungju Oh, and Young-Woo Son provided a model for molecular self-assembly. Professor Vitor Manuel Pereira and his group member Alpin Novianus Tatan explained electron localization in graphene induced by molecular charge impurity.

Administrative support was also very important for the completion of this dissertation. Anne Takizawa, Donna K. Sakima, Elaine S. Quiter, and Lisa Partita helped me with all the paperwork and bureaucratic details.

Finally, I want to thank my family for their support throughout all these years.

1 Introduction

Nanotechnology not only allows us to make electronics smaller and lighter, but also provides numerous opportunities for creating novel properties that do not exist in bulk materials due to quantum confinement. By investigating the fundamental building blocks of nature down to the single atom or molecule scale, we can observe how the properties of materials evolve as we increase the complexity of their structure from the bottom-up. This knowledge will help us to fully explore and engineer nanomaterials as they are integrated into new devices and architectures.

Quantum confinement and enhanced many-body interactions at the nanoscale in low-dimensional materials give rise to many unique optical, electronic and magnetic properties. For example, graphene is a two-dimensional material that has the highest known carrier mobility as well as micrometer-scale spin coherence lengths due to weak electron-phonon and spin-orbit couplings [1-5]. This makes it ideal for high frequency and spin-based logic. Additionally, the massless Dirac fermions in graphene and their ballistic transport properties make graphene ideal as a platform for investigating relativistic quantum mechanics and electron optics [6-8]. On the other hand, organic molecules have flexible chemical and electronic structure which makes them desirable for modifying the electronic properties of two-dimensional material platforms.

Since graphene has a large surface area, it can be easily functionalized by organic molecules. Molecules on graphene can introduce uniform charge transfer doping, as well as periodic Coulomb potentials and spin patterns [9-12]. The atomically flat surface of graphene not only provides a good platform for molecular self-assembly, but also possesses weak van der Waals coupling to the molecules, thus inducing less hybridization with their molecular electronic structure[13]. Graphene also provides gate tunability for adsorbed molecules [14]. The work in this dissertation aims to investigate the molecule-graphene interface and characterize the electronic properties of the molecule-graphene system. We used a gate-tunable graphene platform to control the molecular charge occupation number and self-assembly behavior of molecules on the surfaces.

When we change the carrier concentration in graphene by applying an electrostatic back gate voltage, we are able to tune the molecular orbital energy with respect to the Fermi level. This allows us to inject single electrons into individual molecules and self-assembled molecular nanostructures. This enables the manipulation of single electron spins in the emerging field of graphene-based spintronics. Additionally, graphene acts as a tunable dielectric layer, which can change the screening behavior of a Coulomb potential as a function of carrier density. This can be beneficial for tuning electron-electron interactions within nanostructures on graphene. By using a molecular template, we can fabricate linear molecule arrays on a graphene surface. Molecular arrays generate one-dimensional Coulomb potentials and induce supercritical quasi-localized states for Dirac fermions. In comparison to typical non-relativistic semiconductor dopant states, this novel quantum phenomenon is associated with the relativistic atomic collapse picture, where an electron-hole pair cannot form stable bound states around the nucleus, but rather spiral towards the nucleus. We have also explored charged two-dimensional molecular

islands on a poorly screened graphene surface. The charged two-dimensional molecular island can be used to generate atomically sharp P-N junctions on the surface and to guide current flow on graphene devices with electron optics.

1.1 Graphene Introduction

Graphene is a single layer of carbon atoms covalently bonded in a 2D honeycomb lattice. It was predicted by Philip Wallace in 1947 that graphene has a linear energy-momentum dispersion with zero band gap[15]. In 2004, Geim and Novoselov successfully isolated monolayer graphene on an insulating surface and verified the linear energy-momentum dispersion [16]. Experiments have also shown many unique properties including ballistic electron transport and high electron mobility in graphene. Due to their linear energy-momentum dispersion, electrons in graphene can be modeled as 2D massless Dirac fermions, which allows the exploration of relativistic quantum physics within this material[17]. In this section, I will present the basic electronic properties of graphene from the tight-binding model[18].

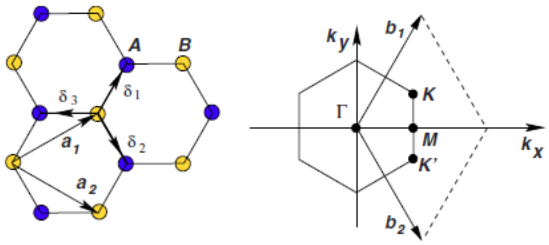

Figure 1.1: Graphene lattice unit cell. The image on the left is the graphene lattice in real space, where a_1 and a_2 are the real space lattice vectors and δ_1, δ_2, δ_3 are the nearest neighbor vectors. On the right is the first Brillouin zone, where b_1 and b_2 are the reciprocal lattice vectors. Adapted from Ref. 17.

The basis of a graphene lattice contains two carbon atoms. The atoms of graphene can thus be broken up into sets of atoms that each form a triangular sublattice, denoted as sublattice A and B. The distance between nearest carbon atoms in the A and B sublattice is $a \sim 1.42$Å. The primitive cell lattice vectors (a_1,a_2) and reciprocal lattice vectors (b_1,b_2) are

$$a_1 = a\left(\frac{3}{2}, \frac{\sqrt{3}}{2}\right), a_2 = a\left(\frac{3}{2}, -\frac{\sqrt{3}}{2}\right), b_1 = \frac{2\pi}{a}\left(\frac{1}{3}, \frac{1}{\sqrt{3}}\right), b_2 = \frac{2\pi}{a}\left(\frac{1}{3}, -\frac{1}{\sqrt{3}}\right). \quad (1.1)$$

The energy bands near the Fermi level are composed of out-of-plane $2p_z$ orbitals of the carbon atoms. The tight binding Bloch wavefunction can be written as,

$$\psi(r) = \sum_R e^{-ik\cdot R}\left[C_A\varphi_A(r-R) + C_B\varphi_B(r-R+\delta_{1,2,3})\right], \quad (1.2)$$

where φ_A and φ_B are normalized $2p_z$ atomic orbitals centered on the A sublattice and B sublattice, respectively. The summation in the Bloch wavefunction is for all lattice sites. C_A and C_B denote the amplitude of the wave function on each sublattice where $|C_A|^2 + |C_B|^2 = 1$. The vector $\delta_{1,2,3}$ pointing to the three nearest neighbors are

$$\delta_1 = a\left(\frac{1}{2}, \frac{\sqrt{3}}{2}\right), \delta_2 = a\left(\frac{1}{2}, -\frac{\sqrt{3}}{2}\right), \delta_3 = a(-1,0). \tag{1.3}$$

The energy of the electronic bands can be calculated with $H|\psi >= E|\psi >$, which we can express as

$$\begin{pmatrix} H_{AA} & H_{AB} \\ H_{BA} & H_{BB} \end{pmatrix} \begin{pmatrix} C_A \\ C_B \end{pmatrix} = E \cdot S \begin{pmatrix} C_A \\ C_B \end{pmatrix}, \tag{1.4}$$

where S, H_{ij} are defined below. Assuming the p_z wave functions between the neighboring atoms are orthogonal, i.e. $\langle \varphi_A(r-R)|\varphi_B(r-R+\delta)\rangle$=0, and considering only nearest neighbor hopping, we can simplify the integral to

$$S =< \varphi_A(r)|\varphi_A(r) >=< \varphi_B(r)|\varphi_B(r) >= N, \tag{1.5}$$

$$H_{AA} =< \varphi_A(r)|H|\varphi_A(r) >= H_{BB} =< \varphi_B(r)|H|\varphi_B(r) >= \varepsilon_0, \tag{1.6}$$

$$\begin{aligned} H_{AB} &=< \varphi_A(r-R)|H|\varphi_B(r-R+\delta) > \\ &= t\left[e^{-ik_x a} + e^{ik_x \frac{1}{2}a + ik_y \frac{\sqrt{3}}{2}a} + e^{ik_x \frac{1}{2}a - ik_y \frac{\sqrt{3}}{2}a}\right], \end{aligned} \tag{1.7}$$

$$\begin{aligned} H_{BA} &=< \varphi_B(r-R+\delta)|H|\varphi_A(r-R) > \\ &= t\left[e^{ik_x a} + e^{-ik_x \frac{1}{2}a + ik_y \frac{\sqrt{3}}{2}a} + e^{-ik_x \frac{1}{2}a - ik_y \frac{\sqrt{3}}{2}a}\right]. \end{aligned} \tag{1.8}$$

We can set the ε_0 to zero as the energy reference point. We obtain the eigenenergies

$$\begin{aligned} \mathrm{E}_{\pm} &= \pm t\sqrt{1 + 4\cos\left(\frac{\sqrt{3}}{2}k_y a\right)cos\left(\frac{3}{2}k_x a\right) + 4cos^2\left(\frac{\sqrt{3}}{2}k_y a\right)}, \\ &= \pm t\sqrt{3 + 4\cos\left(\frac{\sqrt{3}}{2}k_y a\right)cos\left(\frac{3}{2}k_x a\right) + cos\left(\sqrt{3}k_y a\right)}. \end{aligned} \tag{1.9}$$

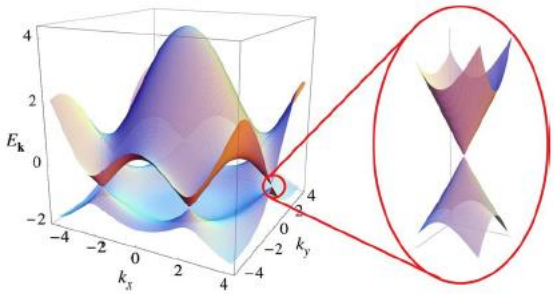

Figure 1.2: Graphene band structure. Graphene energy-momentum dispersion with π* and π connecting at the K and K' points. Adapted from Ref. 17.

We observe that the sublattice orbitals form π^* and π bands around the Fermi level which become the conduction and valence bands of graphene. It is useful to focus on the electronic structure around the reciprocal lattice points K and K'

$$\mathrm{K} = \frac{2\pi}{a}\left(\frac{1}{3}, \frac{1}{3\sqrt{3}}\right), \mathrm{K}' = \frac{2\pi}{a}\left(\frac{1}{3}, -\frac{1}{3\sqrt{3}}\right). \tag{1.10}$$

By plugging this momentum into H_{AB} and H_{BA} and expanding the exponential term to linear order around K and K', we obtain

$$\frac{3}{2}ta\begin{pmatrix} 0 & -k_y - ik_x \\ -k_y + ik_x & 0 \end{pmatrix}\begin{pmatrix} C_A \\ C_B \end{pmatrix} = E\begin{pmatrix} C_A \\ C_B \end{pmatrix} \; and \; \mathrm{E}_{\pm} = \pm\frac{3}{2}ta|k| \equiv \pm\hbar v_F|k|. \tag{1.11}$$

This shows the electronic structure around the K and K' points follows a linear dispersion, where the point of intersection is referred to as the Dirac point. The total number of states and the density of states in graphene per unit area can be calculated using this energy-momentum dispersion as follows,

$$\mathrm{N} = \frac{4(\pi k^2)}{\left(\frac{2\pi}{L}\right)^2} \; and \; DOS = \frac{1}{L^2}\frac{\partial N}{\partial E} = \frac{\partial}{\partial E}\frac{k^2}{\pi} = \frac{\partial}{\partial E}\frac{1}{\pi}\left(\frac{E}{\hbar v_F}\right)^2 = \frac{2E}{\pi(\hbar v_F)^2}. \tag{1.12}$$

This shows the density of states also varies linearly with respect to the Fermi level. The charge density and Fermi level shift induced by a gate voltage is

$$\mathrm{n} = e\frac{N}{L^2} = \frac{e}{\pi}\left(\frac{E}{\hbar v_F}\right)^2 = \varepsilon E_g = \varepsilon\frac{V_g}{d} = \; and \; E = \hbar v_F\sqrt{\frac{\varepsilon\pi}{ed}V_g} = \hbar v_F\sqrt{\frac{\pi C}{eA}V_g} \tag{1.13}$$

$$\text{where } \mathrm{C} = \varepsilon A/d.$$

We can see that the Fermi level has a square root dependence on gate voltage. A typical electrostatic back gate can induce a shift in the Dirac point of around 400 meV, which corresponds to an induced carrier density of around $3 \times 10^{12}\ cm^{-2}$. By fitting the curve of gate voltage versus Fermi energy, we can extract the Fermi velocity from experiment. The typical

Fermi velocity of electrons in graphene is around $1.1 \times 10^6\ m/s$, around 300 times smaller than the speed of light. In a transport measurement, we can also extract the global mobility μ from the conductance

$$\sigma = n\mu = \varepsilon \frac{V_g}{d}\mu \ \ \Rightarrow \ \ \mu = \frac{d}{\varepsilon}\frac{\sigma}{V_g} = \frac{A}{C}\frac{\sigma}{V_g}. \tag{1.14}$$

In experiment, a good quality graphene sample can reach a carrier mobility of around $5 \times 10^4\ cm^2V^{-1}s^{-1}$. This value is around 50 times higher than silicon, which makes graphene suitable for high frequency circuits.

1.2 Atomic collapse resonance

Relativistic quantum mechanics predicts that when an atom has enough charge in its nucleus it will force the electrons around it to move with a speed in the ultra-relativistic regime. As the Coulomb attraction exceeds the angular momentum of the electron, the electron will spiral inward toward the nucleus while a positron (hole) will escape to infinity. This novel quantum state around the nucleus is called an atomic collapse resonance.[19-21]. In graphene, electrons behave like relativistic particles with a small Fermi velocity (300 times less than speed of light) and the effective structure constant is near unity. It is thus possible to approach the limit of supercritical nuclear charge by using localized Coulomb impurities to induce this atomic collapse state [6, 22, 23]. The Coulomb impurities can be adsorbed atoms or molecules with charge transfer to graphene. Without a band gap, the atomic collapse state will be quasi-bounded around the charge impurity with a finite lifetime, and can eventually tunnel into the graphene continuum band. Here I will present a basic semiclassical orbital stability analysis for the Dirac-Kepler problem.

For a Coulomb potential in graphene, we can write the energy of a nearby electron as

$$E = pv_F - \frac{Ze^2}{r}, \tag{1.15}$$

where v_F is the Fermi velocity. To analyze the orbital stability, we need to consider the motion in the radial direction. This requires that we separate the momentum in the radial direction and azimuthal direction

$$p = \frac{1}{v_F}\left(E + \frac{Ze^2}{r}\right) \ and \ p^2 = {p_r}^2 + {p_\theta}^2 = {p_r}^2 + \left(\frac{L}{r}\right)^2, \tag{1.16}$$

$${p_r}^2 = \frac{1}{{v_F}^2}\left(E + \frac{Ze^2}{r}\right)^2 - \left(\frac{L}{r}\right)^2, \tag{1.17}$$

The solution where ${p_r}^2 = 0$ sets the critical value for the classical turning point of the state, resulting in

$$E = \frac{v_F L - Ze^2}{r}, \tag{1.18}$$

Defining a critical threshold where E=0 and imposing the Heisenberg uncertainty condition $pr = r\,L/r \sim \hbar$, results in the critical nuclear charge

$$\mathrm{Z} = \frac{v_F L}{e^2} \sim \frac{v_F \hbar}{e^2} = \frac{1}{\alpha}. \tag{1.19}$$

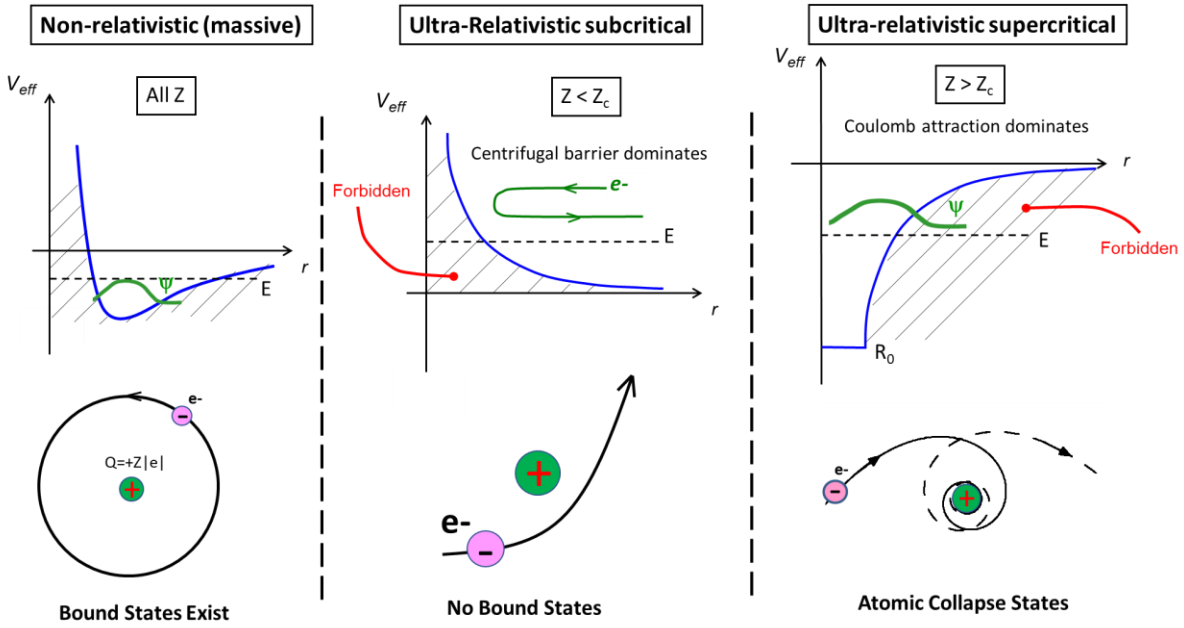

Figure 1.3: Orbitals in a Coulomb potential. The left panel represents the bound state in a hydrogen model. The middle panel represents the subcritical condition for an ultra-relativistic hydrogen atom. The right panel represents the supercritical condition for an ultra-relativistic hydrogen atom where the atomic collapse state forms.

When $\mathrm{Z} < \frac{v_F \hbar}{e^2}$ we get $\mathrm{E} \propto 1/r$, and so no bound states will form, and the electron will scatter from the Coulomb potential. This is called the subcritical regime. When $\mathrm{Z} > \frac{v_F \hbar}{e^2}$ we get $\mathrm{E} \propto -1/r$, and the electron will spiral into the center of the nucleus while emitting a positron (hole). This is called the supercritical regime. The supercritical regime can be achieved by packing multiple charge impurities together until the reach the threshold potential strength at the graphene surface.

1.3 Scanning tunneling microscopy and spectroscopy

Based on the concept of quantum tunneling, scanning tunneling microscopy (STM) allows us to investigate the topography and electronic structure of materials in the vicinity of the STM tip down to the atomic level. The first scanning tunneling microscope was developed by Binning, Rohrer, Gerber, and Weibel in 1981[24, 25]. The basic setup of a scanning tunneling microscope consists of a sharp metal tip attached to a set of piezo drives that operate in the x/y/z directions.

When the tip is positioned less than 1nm away from a conductive surface with finite bias voltage, electrons from the metal tip can tunnel to the surface with exponential sensitivity to the tip-sample distance. An image of the surface can be constructed by scanning the tip over it and measuring the tunneling current at each location.

The theoretical picture of quantum tunneling was developed by Bardeen, Tersoff and Hamann[26, 27]. The transition rate of a single electron eigenstate can be calculated using Fermi's golden rule[28, 29].

$$W_{i\to f} = \frac{2\pi}{\hbar}\left|\langle\psi_f|H'|\psi_i\rangle\right|^2\delta(E_f - E_i). \tag{1.20}$$

Let us first consider the case where the initial state of the electron is in the tip and the final state is in the sample, where the tunneling matrix element is $M_{s,t} \equiv \langle\psi_s|H'|\psi_t\rangle$. In the elastic tunneling regime, the transition of the electron between tip and sample conserves energy and the tunneling rate is.

$$W_{t\to s} = \frac{2\pi}{\hbar}\left|M_{s,t}\right|^2\delta(E_F - E). \tag{1.21}$$

The total tunneling rate depends on the number of states participating in tunneling from the tip to the sample. In order to properly measure the electronic structure of the sample, we usually calibrate our tip to have a relatively uniform density of states at all energies. The continuum of energy states in the tip can be approximated by an integral over a constant tip density of state ρ_t. The sample states can be evaluated by a sum over discrete delta functions. The equation becomes

$$W_{t\to s} = \frac{2\pi}{\hbar}\sum_s\int_{-\infty}^{\infty}\left|M_{s,t}\right|^2\delta(E_F - E)\rho_t\, dE. \tag{1.22}$$

In addition to accounting for the density of states, we also need to consider the electron/hole occupancy around the Fermi level, which can be written as a Fermi-Dirac distribution. The electron will be tunneling from a filled tip state into an empty sample state.

$$W_{t\to s} = \frac{2\pi}{\hbar}\rho_t\sum_s\int_{-\infty}^{\infty}\left|M_{s,t}\right|^2\delta(E_F - E)\left[1 - \left(\frac{1}{e^{\frac{E-E_F}{kT}}+1}\right)\right]\left(\frac{1}{e^{\frac{E-E_F}{kT}}+1}\right) dE. \tag{1.23}$$

We can define the Fermi-Dirac distribution $f(E) = \left(\frac{1}{e^{\frac{E-E_F}{kT}}+1}\right)$. When we apply a bias V on the sample, we will shift the band structure of the sample by eV, which will shift the energy reference of the Fermi-Dirac distribution and the density of states with respect to the Fermi level.

$$W_{t\to s} = \frac{2\pi}{\hbar}\rho_t\sum_s\int_{-\infty}^{\infty}\left|M_{s,t}\right|^2\delta(E - eV - E_F)[1 - f(E - eV)\,]f(E)\;dE. \tag{1.24}$$

Similarly, we can write the transition rate for electrons tunneling from sample back to the tip,

$$W_{s\to t} = \frac{2\pi}{\hbar}\rho_t \sum_s \int_{-\infty}^{\infty} \left|M_{t,s}\right|^2 \delta(E - eV - E_F)[1 - f(E)\,]f(E - eV)\; dE. \tag{1.25}$$

Hence, the total tunneling current can be written as

$$I = -e(W_{s\to t} - W_{t\to s}) \tag{1.26}$$
$$= \frac{2\pi}{\hbar}\rho_t \sum_s \int_{-\infty}^{\infty} \left|M_{s,t}\right|^2 \delta(E - eV - E_F)\,[f(E) - f(E - eV)]dE.$$

Approximating the Fermi-Dirac distribution as step function for low temperature experiments,

$$I = \frac{2\pi}{\hbar}\rho_t \sum_s \int_0^{eV} \left|M_{t,s}\right|^2 \delta(E - eV - E_F)\, dE. \tag{1.27}$$

Bardeen has given the form to calculate the matrix element by treating the sample Hamiltonian as a perturbation for the tunneling process, under the elastic tunneling condition $E_s = E_t$ and zero tip bias [26]

$$M_{s,t} = \int {\psi_s}^* H' \psi_t dr = \int {\psi_s}^* \left(E_s - \frac{p^2}{2m}\right)\psi_t dr = \int {\psi_s}^* \left(E_t - \frac{\hbar^2}{2m}\nabla^2\right)\psi_t dr \tag{1.28}$$
$$= \frac{\hbar^2}{2m}\int (\psi_t \nabla^2 {\psi_s}^* - {\psi_s}^* \nabla^2 \psi_t) dr.$$

According to Tersoff and Hamann, we can approximate a tip state using a wave function with spherical symmetry[27].

$$\psi_t = \frac{e^{-\kappa r}}{4\pi r}, \tag{1.29}$$

Setting the tip center at the origin, the tunneling matrix element becomes

$$M_{s,t} = C e^{(-\kappa z)} \psi_s(z = 0). \tag{1.30}$$

This will give us the tunneling current,

$$I(V) \propto e^{(-2\kappa z)} \sum_s \int_0^{eV} |\psi_s(z = 0)|^2 \delta(E - eV - E_F)\, dE \tag{1.31}$$

When we scan with a constant current, the STM feedback will change the tip-sample distance to map out the sample density of states for states integrated from the Fermi level to the bias voltage. This gives us the topography of the sample. Scanning tunneling spectroscopy can also be carried out by measuring the differential conductance.

$$\left(\frac{dI}{dV}\right)_{V=V'} \propto \sum_s |\psi_s(z = 0)|^2\, \delta(E - eV - E_F) = LDOS(E_F + eV). \tag{1.32}$$

At constant tip-sample separation, the differential conductance is proportional to the sample local density of states at set bias voltage. The spatial distribution of a state can then be mapped out by scanning the tip at constant height and bias while recording the differential conductance across the surface.

1.4 Atomic force microscopy and Kelvin probe force microscopy

Atomic force microscopy (AFM) offers another way to investigate the physical properties of a surface nanostructure at the atomic scale through the detection of atomic force interaction. Atomic force microscopy was first developed by Binnig *et al.* in 1986[30]. The most common atomic force interaction includes the electrostatic force, van der Waals force, and Pauli repulsion interaction. These force interactions are detected by measuring amplitude, phase, or frequency changes of a tip mounted on an oscillator. The qPlus AFM design developed by Franz Giessibl enables stable concurrent detection of tunneling current and atomic force interaction[31, 32]. Using carbon monoxide functionalized qPlus tips, Meyer *et al.* found that it is possible to resolve chemical bonds with enhanced Pauli repulsion interaction[33]. This technique allows us to investigate the chemical and electronic structure of a nanomaterial concurrently.

The theory of atomic force detection with frequency-modulated AFM was developed by Giessibl in 1997[34]. Assuming a tip oscillating above a sample surface with a minimum distance d and amplitude A_0, we can write the time dependent oscillation amplitude as

$$q(t) = q_{os}(t) + d + A_0 \;\; where \;\; q_{os}(t) \equiv A_0 \cos(2\pi f_0 t)\,, f_0 \equiv \frac{1}{2\pi}\sqrt{\frac{k}{m^*}}. \tag{1.33}$$

The Hamiltonian of the oscillator is

$$H_0 = \frac{p^2}{2m^*} + \frac{k{q_{os}}^2}{2} \quad and\ p \equiv m^* \frac{dq_{os}}{dt}. \tag{1.34}$$

Approximating the tip-sample interaction as an inverse power law perturbation

$$F_{ts}(q) = -Cq^{-n}, \Delta H = \int F_{ts}(q)dq = -\frac{C}{(n-1)q^{n-1}} \; for\ n > 1. \tag{1.35}$$

Using the Hamilton-Jacobi formalism, we will define a new variable, the action J and phase angle β, with which we rewrite the kinematic variables as

$$q_{os}(t) \equiv \sqrt{\frac{2f_0 J}{k}} \sin 2\pi\big(f_0 t + \beta(t)\big)\,, p(t) \equiv \sqrt{\frac{J}{2\pi^2 k f_0}} \cos 2\pi\big(f_0 t + \beta(t)\big). \tag{1.36}$$

By inspection, we can find that without the perturbation,

$$J = \frac{k{A_0}^2}{2f_0}, \beta = \frac{1}{4}. \tag{1.37}$$

When there is a perturbation J and β can be viewed as generalized momentum and position related to the Hamiltonian by

$$\frac{dJ}{dt} = -\frac{\partial H}{\partial \beta}; \quad \frac{d\beta}{dt} = \frac{\partial H}{\partial J}. \tag{1.38}$$

When the tip-sample interaction is much smaller than the restoring force, we can write the frequency shift of the oscillator as,

$$\Delta f = \langle \frac{d\beta}{dt} \rangle = \langle \frac{\partial H}{\partial J} \rangle \sim \langle \frac{\partial \Delta H}{\partial J} \rangle = \langle \frac{\partial \Delta H}{\partial q_{os}} \frac{\partial q_{os}}{\partial J} \rangle = \langle -F_{ts} \frac{q_{os}}{2J} \rangle = -\frac{f_0}{{kA_0}^2} \langle F_{ts} q_{os} \rangle. \tag{1.39}$$

Considering the time average over a full period $T_0 = 1/f_0$, we define $x \equiv 2\pi f_0 t$

$$\begin{aligned} \Delta f &= \frac{f_0}{{kA_0}^2} \frac{1}{T_0} \int_0^{T_0} \frac{CA_0 \cos(2\pi f_0 t)}{\{d + A_0 + A_0[cos(2\pi f_0 t)]\}^n} dt, \\ &= \frac{1}{2\pi} \frac{f_0}{{kA_0}^2} \frac{C}{d^n} \int_0^{2\pi} \frac{CA_0 \cos(x)}{\left\{1 + \frac{A_0}{d}[1 + cos(x)]\right\}^n} dx. \end{aligned} \tag{1.40}$$

At small amplitudes,

$$\begin{aligned} \Delta f &= \frac{1}{2\pi} \frac{f_0}{{kA_0}^2} \frac{C}{d^n} \int_0^{2\pi} CA_0 \cos(x) \left\{1 - n\frac{A_0}{d}[1 + cos(x)]\right\} dx, \\ &= -n\frac{f_0}{2k}\frac{C}{d^{n+1}} = -\frac{f_0}{2k}\frac{\partial F_{ts}}{\partial q}. \end{aligned} \tag{1.41}$$

The final equation yields that the frequency shift is proportional to the force gradient with respect to the tip-sample distance. The common force interaction can be modeled as a Lennard-Jones potential with the form

$$\begin{aligned} V_{LJ}(z) \propto \left[\left(\frac{z_m}{z}\right)^{12} - \left(\frac{z_m}{z}\right)^6\right], \; F_{LJ}(z) \propto -12\left[\frac{{z_m}^{12}}{z^{13}} - \frac{{z_m}^6}{z^7}\right], \\ \Delta f_{LJ}(z) \propto \left[13\frac{{z_m}^{12}}{z^{14}} - 7\frac{{z_m}^6}{z^8}\right]. \end{aligned} \tag{1.42}$$

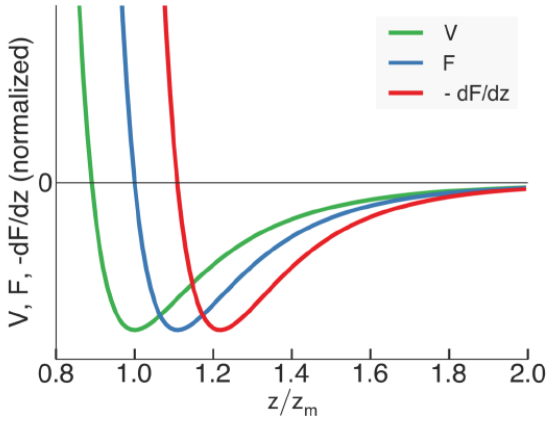

Figure 1.4: Lennard-Jones potential, force, and frequency shift

In the repulsive regime, the interaction is dominated by the short-range Pauli repulsion interaction. In the attractive regime, the interaction is dominated by long-range van der Waals and electrostatic interactions. The chemical structure of a molecule can be resolved by bringing the tip into the repulsive regime. When the tip is above an atom or chemical bond with high electron density, the short-range Pauli repulsion interaction will generate a large signal due to orbital overlap with the between sample atom and probe atoms.

The long-range electrostatic interaction can be used to measure work function alignment as a result of charge transfer by performing Kelvin probe force microscopy. As we apply a bias on the tip, the oscillation frequency will change as a result of the long-range electrostatic interaction. The voltage dependence of the electrostatic force can be modeled with,

$$\Delta q = C(z)(V_{CPD} - V_b), \quad \text{e}V_{CPD} = W_s - W_t. \tag{1.43}$$

The contact potential difference is defined by the work function difference between tip and sample. The corresponding electrostatic energy, force, and frequency shift are

$$E(z) = \frac{1}{2}C(z)(V_{CPD} - V_b)^2, F(z) = -\frac{1}{2}\frac{\partial C(z)}{\partial z}(V_{CPD} - V_b)^2, \tag{1.44}$$
$$\Delta f = -\frac{f_0}{2k}\frac{\partial^2 C(z)}{\partial z^2}(V_{CPD} - V_b)^2.$$

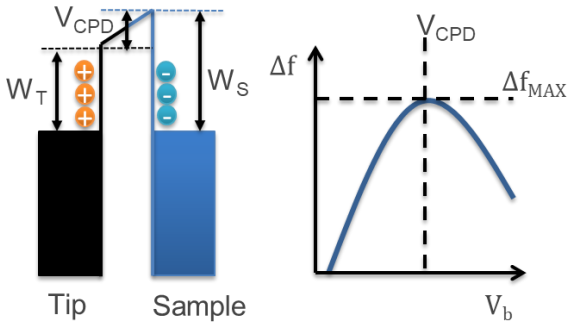

Figure 1.5: Kelvin probe force microscopy. The image on the left shows the work function difference and the image on the right shows the contact potential difference from the bias versus frequency curve.

We can align the work function between the tip and sample by applying a sample bias equal to the local contact potential difference. When the work function between the tip and sample is aligned, there is no charge at the tip-sample junction, and the electrostatic interaction is minimal, which can be detected by the frequency shift of the oscillator.

1.5 Tip-induced charging

Since the metal tip used in local probe techniques has a different work function compared to the probed surface, the work function difference will create an electric field when the tip is positioned on top of the sample. This electric field will induce charge accumulation and shift the electronic band energy with respect to the sample Fermi level at the vicinity of the tip[35]. As the tip electric field brings a localized impurity state across the Fermi level of the sample, it causes a change in conductance and atomic force interaction between the tip and the sample.

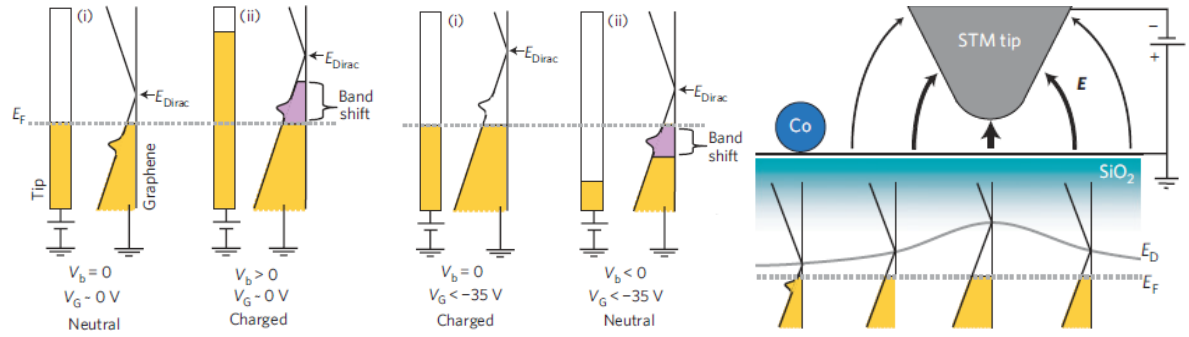

Figure 1.6: Tip induced charging and band bending. The left image shows how the tip induces the electronic band to shift up and cause the impurity to be discharged, the middle image shows how the tip electric field causes the impurity to be charged. The right image shows how tip induced band bending causes the molecules to be discharged at a particular lateral distance away from the impurity. Adapted from Ref. 34.

Fig. 1.6 shows an example of a localized impurity state hybridized with graphene bands. Since dielectric screening in graphene is weak, the tip electric field will cause band bending

around the tip, which changes the energy of both the graphene band and the localized impurity state. As the electric field brings the state across the Fermi level, the electrostatic potential will suddenly change around the impurity. The screening response around the impurity due to change of the electrostatic potential causes a discontinuity in the conductance. Since the energy of such localized states is sensitive to a change of the electric field, changing the tip bias will result in a sharp peak in the differential conductance. When the localized impurity state is above/below the Fermi level, we can use the tip electric field to charge/discharge the impurity. When the state is brought closer to the Fermi level by the back-gate voltage, it becomes easier to change the charge state of the impurity. This causes the charging peak to move in the opposite direction compared to the impurity state in the spectroscopy as gate voltage is increased.

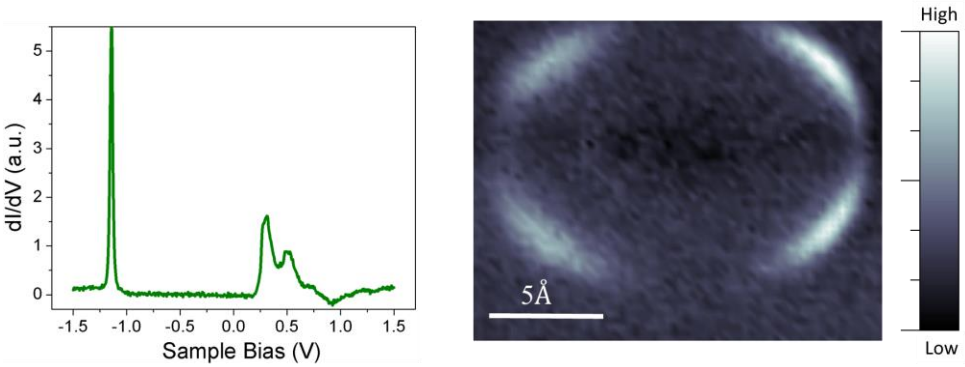

Figure 1.7: Scanning tunneling spectroscopy of a charge peak in LDOS and the charging ring in real space. The image on the left shows a charging peak of a charged impurity at negative sample bias near -1V. The image on the right shows the spatial distribution of the tip-induced charging by taking a differential conductance map.

Similar charging behavior can occur as we change the lateral distance between the tip and localized impurity. The tunneling conductance will abruptly change when we bring the tip to a threshold radius from the impurity. This will result in a ring-like feature around the impurity due to a change in conductance. The charging effect can also be detected by measuring the atomic force interaction directly. The change in the electrostatic force will cause a discontinuity in frequency as we vary the bias of the tip. As we take constant-height maps while measuring the frequency, the discontinuity in frequency will also form a ring-like structure on the surface, which resembles the charging phenomenon in the STM mode.

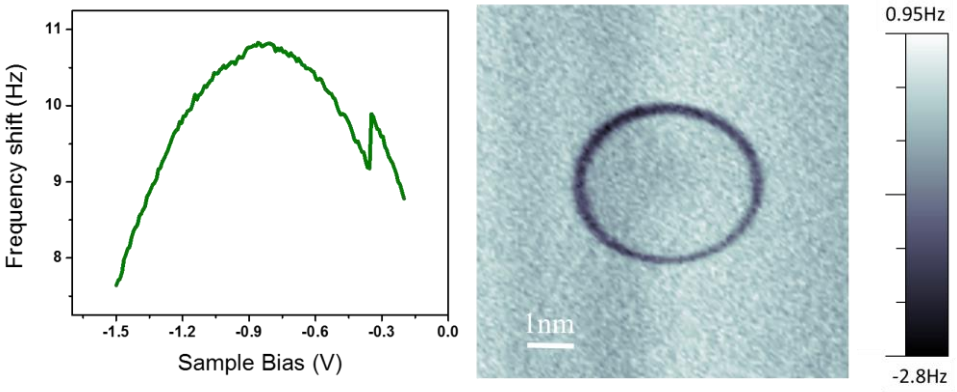

Figure 1.8 Kelvin probe force microscopy and constant height frequency modulated AFM map of a molecule charging. The image on the left shows a Kelvin probe force microscopy spectrum with a molecule charged near -0.3V. The electrostatic force interaction will shift the parabola up or down dependent on the polarity of the charge. The image on the right shows a charging ring detected by constant-height frequency-modulated AFM.

1.6 Inelastic tunneling in graphene

The Dirac cones in graphene are located at the K and K' points in reciprocal space. Hence, elastic tunneling to the K point near the Fermi level is suppressed[36]. However, we can raise the bias so that the electron can first tunnel into an empty state in the graphene σ* band near the Γ point through a virtual transition and then relax into a lower energy state by exciting a phonon. This tunneling mechanism is much more efficient due to the out-of-plane phonon mode at the K and K'points[37]. As a result, the tunneling conductance is much larger above the phonon excitation energy, which we measured to be 63meV at 5K. In contrast, the suppression of the conductance below the excitation energy forms a gap-like feature with finite conductance from the elastic channel.

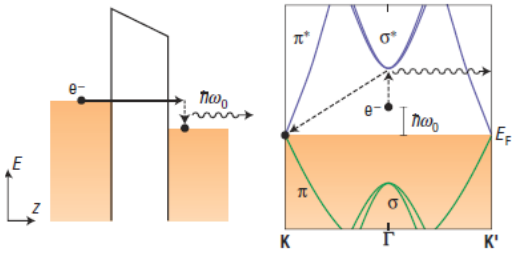

Figure 1.9: Phonon assisted inelastic tunneling tip into graphene Dirac point. The left image shows the energy diagram for the inelastic tunneling process. A phonon is released during the process. The right image shows the electron will gain momentum as it releases a phonon and tunnels into the K or K' point. Adapted from Ref. 35.

Such inelastic tunneling momenta can be evaluated by measuring the decay constant in the tunneling experiment. In a tunneling experiment, the LDOS will decay exponentially in vacuum:

$$LDOS \propto e^{(-2\kappa z)} \; where \; \kappa = \sqrt{\frac{2m\phi}{\hbar^2} + {k_\parallel}^2}, \tag{1.45}$$

where $k_\parallel$ here corresponds to the crystal momentum at the K and K' point parallel to the surface. In order for an electron with energy lower than the threshold energy to tunnel into the K and K' point, it would need to absorb a phonon. However, at low temperatures, there are few phonons available, hence inelastic tunneling is suppressed.

2 Graphene/BN device fabrication

Graphene/BN heterostructures provide an ideal platform for high mobility electron transport and molecular self-assembly. However, surface contaminants can significantly reduce the electron mobility due to impurity scattering and influence molecular self-assembly by raising the surface diffusion barrier. In this chapter, we will discuss the methods for preparing atomically-clean graphene surfaces for local probe study and high-performance graphene devices. When we place graphene on a BN/SiO2 dielectric surface, we can control the carrier density of graphene by applying a bias voltage across the dielectric layer. It also enables us to adjust electron-electron correlation effects through impurity charging and screening on the surface.

This chapter presents our procedures for fabricating atomically-clean graphene/BN heterostructure field effect transistor (FET) devices. Gate tunable graphene/BN FET devices are composed of channel material (graphene), dielectric material (BN/SiO2), contact material (Ti/Au) and the device package (sample mounting and wire bonding). We will discuss some challenges and strategies of fabricating devices and characterizing their electronic structure with local probe microscopy. The content here is based on our published paper: H.S. Jung et al., "Fabrication of Gate-tunable Graphene Devices for Scanning Tunneling Microscopy Studies with Coulomb Impurities", *J. Vis. Exp.* 101, e52711 (2015)[38].

2.1 Methods

The fabrication of a back-gated graphene device decorated with Coulomb impurities (*e.g.* charged Ca atoms) is outlined. The device consists of elements in the following order (from top to bottom): calcium adatoms and clusters, graphene, hexagonal boron nitride (h-BN), silicon dioxide (SiO_2), and bulk silicon (**Figure 2.1**). h-BN is an insulating thin film, which provides an atomically flat and electrically homogeneous substrate for the graphene.[2, 39, 40] h-BN and SiO_2 act as dielectrics, and bulk Si serves as the back-gate.

To fabricate the device, graphene is first grown on an electrochemically polished Cu foil[41, 42], which acts as a clean catalytic surface for the chemical vapor deposition (CVD)[41-44] of graphene. In a CVD growth, methane (CH_4) and hydrogen (H_2) precursor gases undergo pyrolysis to form domains of graphene crystals on the Cu foil. These domains grow and eventually merge together, forming a polycrystalline graphene sheet.[44] The resulting graphene is transferred onto the target substrate, an h-BN/SiO_2 chip (prepared by mechanical exfoliation[45] of h-BN onto an SiO_2/Si(100) chip), *via* poly(methyl methacrylate) (PMMA) transfer.[46-48]In the PMMA transfer, the graphene on Cu is first spin-coated with a layer of PMMA. The PMMA/graphene/Cu sample then floats on an etchant solution (*e.g.* $FeCl_3$ (aq)[48]), which etches away the Cu. The unreacted PMMA/graphene sample is fished with an h-BN/SiO_2 chip and subsequently cleaned in an organic solvent (*e.g.* CH_2Cl_2) and Ar/H_2 environment [45, 49] to remove the PMMA layer. The resulting graphene/h-BN/SiO_2/Si sample is then wire-bonded to electrical contacts on an ultra-high-vacuum (UHV) sample plate and

annealed in an UHV chamber. Finally, the graphene device is deposited *in situ* with Coulomb impurities (*e.g.* charged Ca atoms) and studied by STM.[7, 14, 35, 50]

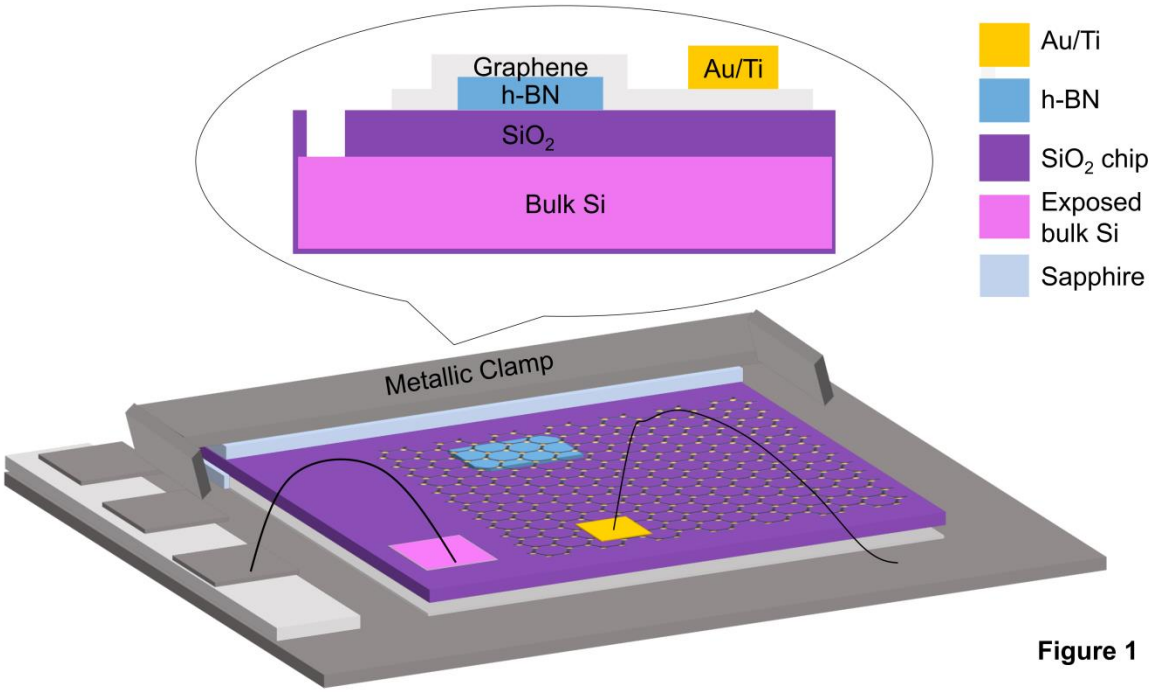

Figure 2.1: Schematic of a gate-tunable graphene device. Graphene is grounded to the sample plate while Si layer connects to a gate electrode through wire-bonding.

Figure 2.1 illustrates a schematic of a back-gated graphene device. A wire-bonded Au/Ti contact to the UHV sample plate grounds the graphene electrically, while wire-bonding the Si bulk to an electrode connected to an external circuit back-gates the device. By back-gating a device, a charge state of a Coulomb impurity at a given sample bias (which is controlled by the STM tip) can be easily tuned to a different charge state. [7, 35, 50]

Figure 2.2. outlines the steps for fabricating a gate-tunable graphene device. A Cu foil is first electrochemically polished to remove its protective surface coating and modify its growth seed density.[42, 43] After electrochemical polishing, the Cu foil should appear shinier under the naked eye than before as its surface becomes smoother. The electrochemically polished Cu foil then acts as a catalytic substrate for CVD growth of graphene. Graphene is then transferred onto an h-BN/SiO_2 substrate *via* PMMA transfer. The resulting sample is cleaned in an Ar/H_2 atmosphere and characterized (**Figure 2.3**). Subsequently, it is assembled into a back-gated device.

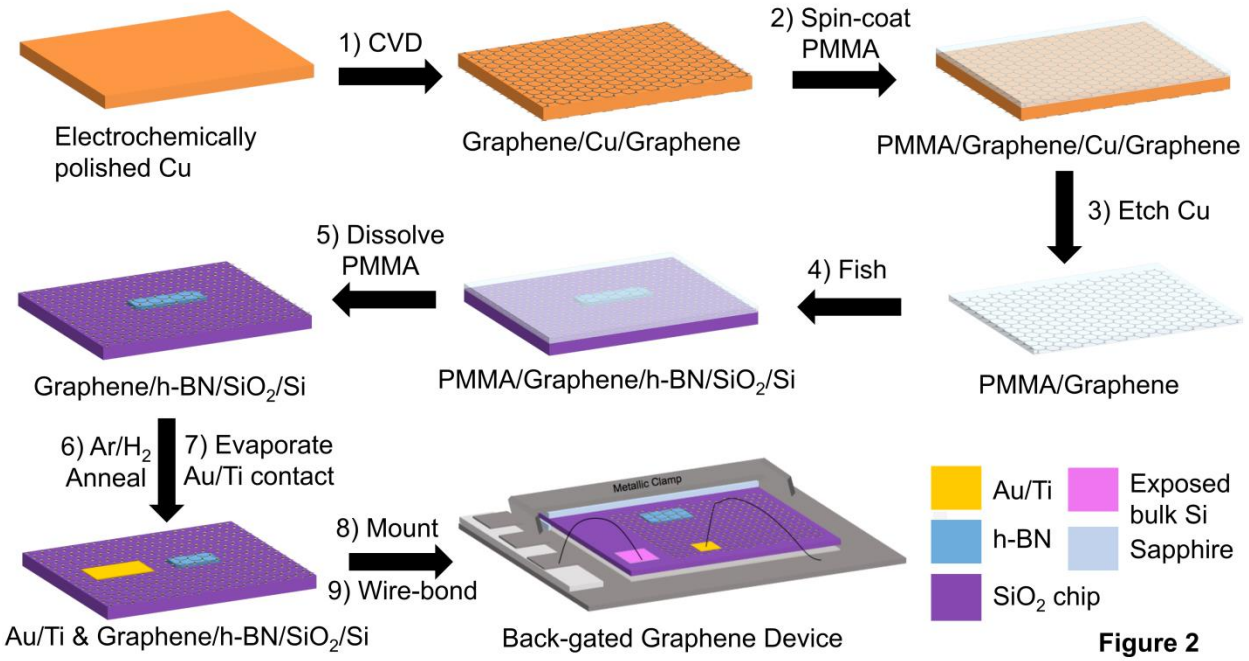

Figure 2.2: Process schematic of gate-tunable graphene device fabrication. The steps of fabricating a gate-tunable graphene device include: 1) CVD graphene growth on an electrochemically polished Cu foil, 2) – 5) PMMA transfer of graphene onto a h-BN/SiO_2 chip, 6) Ar/H_2 annealing, 7) evaporation of Au/Ti contact, 8) mounting onto an UHV sample plate, and 9) wire-bonding.

Before the sample is assembled into a back-gated device, the graphene surface is characterized by an optical microscope (**Figure 2.3a**), Raman spectroscopy (**Figure 2.3b**), and AFM (**Figure 2.3c**). With an optical microscope image, it is easy to examine the cleanliness, continuity, and the number of graphene layers throughout the entire sample. With a Raman spectrum, the number of graphene layers and defect level can be evaluated by examining the I_G:I_{2D} peak intensity ratio and D peak intensity, respectively.[51] With an AFM image, various features – cleanliness, uniformity, surface roughness, *etc*. – of the sample can be reliably evaluated at a small length scale (<500 nm). A good sample should appear clean, continuous, uniform, and monolayer under both optical microscope and AFM images. Moreover, a good sample should exhibit a minimal D peak intensity (a sign of minimal defect) and less than 1:2 ratio of I_G:I_{2D} peak intensity ratio (a sign of monolayer) under Raman spectroscopy.[51]

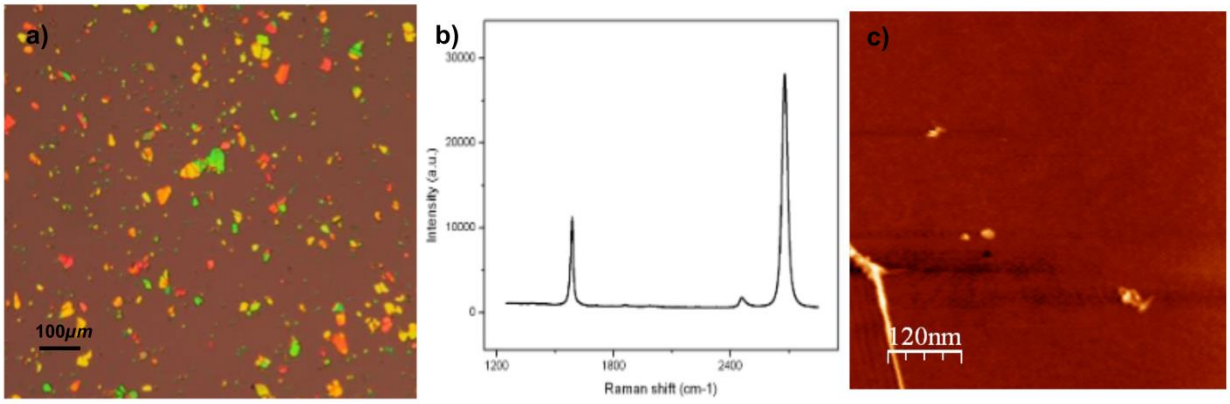

Figure 2.3: Pre-STM characterization of a graphene/h-BN/SiO2 heterostructure. a) Optical microscope image of graphene/h-BN/SiO_2 heterostructure. b) Raman spectrum of graphene/SiO_2 region. Raman spectrum of graphene is characterized by D (~1350 cm^{-1}), G (~1580 cm^{-1}), and 2D (~2690 cm^{-1}) peaks.[51] c) Atomic force microscope (AFM) image of graphene/h-BN/SiO_2 region. This image is a height map taken with tapping mode AFM.

Before the device can be characterized under a STM, a STM tip must be calibrated on a Au(111) surface to decouple the STM tip states from the sample's surface states as much as possible. This process of decoupling is very crucial for a reliable STM study because without the tip calibration, the differential conductance *dI/dV* spectrum will appear convoluted due to a strong coupling between the tip states and the sample's surface states: in other words, STM data taken from an uncalibrated tip may not represent the real property of the sample. To calibrate the tip, the STM tip is repetitively pulsed/poked into a Au(111) surface until a high resolution image of herringbone reconstruction (**Figure 2.4a**) can be obtained and a *dI/dV* spectrum appears comparable to the standard Au(111) *dI/dV* spectrum (**Figure 2.4b**). The *dI/dV* spectrum should exhibit a sharp step at $V_{sample} \approx -0.5$ V, which represents the onset of the Au(111) surface state. Moreover, the *dI/dV* spectrum should exhibit no anomalous peaks and dips, which may appear as artifacts when performing *dI/dV* measurements on a graphene.

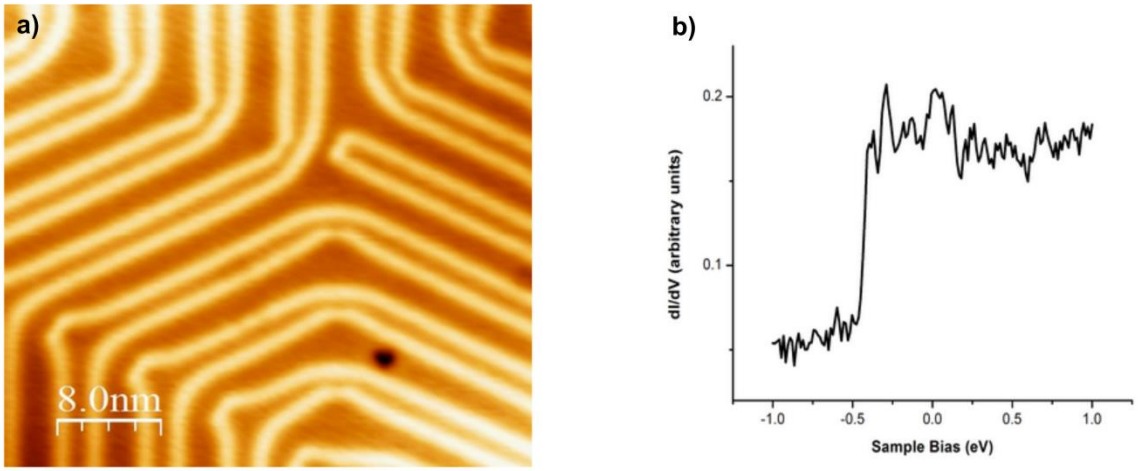

Figure 2.4: STM characterization of Au(111) surface for STM tip calibration. a) Topography of Au(111) surface. b) Standard *dI/dV* spectrum of Au(111) surface.

After the tip calibration, the sample surface is examined with STM. **Figure 2.5a** shows a Moiré pattern for graphene/h-BN, which arises from a mismatch in the lattice constants of graphene and h-BN. The wavelength of a Moiré pattern depends on the angle of rotation between the graphene and underlying h-BN lattices: smaller the twist angle, greater the wavelength. Appearance of Moiré patterns confirms the presence of clean graphene on a h-BN substrate. Once the sample surface is examined, Ca ions are deposited onto graphene, whose topography is shown in **Figure 2.5b**. A Moiré pattern appears in the background of the image. Once charged Ca atoms are successfully deposited, the STM tip can construct artificial nuclei consisting of multiple charged Ca dimers by pushing each dimer into small clusters.

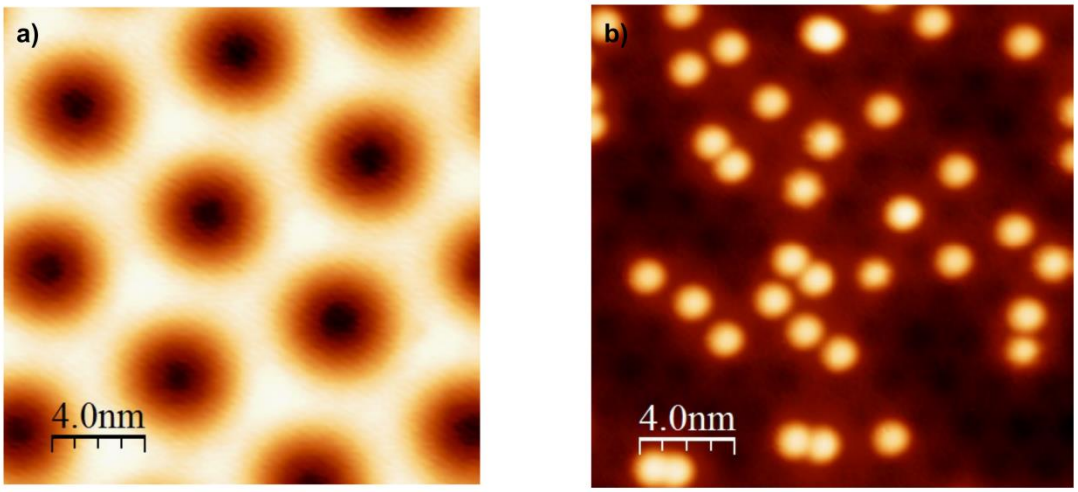

Figure 2.5: STM Topography of Coulomb impurities on graphene. a) Moiré pattern for graphene/h-BN. b) Ca adatoms on graphene.

For STM characterization, critical goals of the graphene device fabrication include: 1) growing monolayer graphene with a minimal number of defects, 2) obtaining a large, clean, uniform, and continuous graphene surface, 3) assembling a graphene device with high resistance between the graphene and the gate (*i.e.* no "gate leakage"), and 4) depositing individual Coulomb impurities.

2.2 Discussion

The first goal is governed by the CVD process, during which graphene grows on a Cu foil. Although there are multiple substrate candidates (*e.g.* Ni, Ru, Ir, Pt, Co, Pd, *etc.*), Cu is well known to produce monolayer graphene most selectively due to its extremely low carbon solubility.[44] Nevertheless, selectively growing monolayer graphene can still be difficult and inconsistent due to a wide range of factors.[41-44] Although electrochemical polishing certainly provides a better substrate condition for graphene growth, our AFM characterizations have shown that the Cu surface remains non-uniform and rough on the microscopic level. Moreover, the level of contamination from chemical residue may vary from foil to foil. Annealing parameters are essential for consistently providing a clean and uniform Cu surface during growth. Annealing the Cu at a high temperature (1050 ℃) near its melting point (1085 ℃) with a high flow of hydrogen (~200 sccm) seems to provide a consistently clean and uniform Cu surface with large Cu domains.[41] The growth temperature, pressure regime, and CH_4:H_2 flow rate ratio can then be systematically optimized until monolayer graphene with a minimal number of defects is obtained.

The second goal – obtaining a large, clean, uniform, and continuous graphene surface – is governed by the PMMA transfer and Ar/H_2 annealing. Although there are a number of different graphene transfer methods (*e.g.* dry PMMA/PDMS transfer[47], wet PDMS transfer[43], *etc.*), PMMA transfer with $FeCl_3$ (aq) etchant solution[48] has consistently yielded the most continuous/uniform graphene surfaces. However, this method leaves a high density of chemical residue on the graphene surface. To resolve this issue, the spin-coating rate and time are first optimized to make the PMMA layer as uniform as possible. Multiple cleaning steps with ultra-pure water baths are introduced to remove chemical residue from the graphene's back surface before fishing it out with an h-BN/SiO_2 chip. Lastly, PMMA curing parameters (e.g. temperature, time, *etc.*) are optimized to facilitate the residual of PMMA with CH_2Cl_2. From these efforts, relatively clean samples, as seen by an optical microscope, have been transferred consistently. No variation in the PMMA transfer method, however, can completely clean up the graphene surface as it always leaves a thin layer of PMMA. To obtain an atomically clean surface (STM studies require clean regions >100 nm^2), a series of annealing procedures must be performed. Ar/H_2 annealing can effectively remove a majority of the PMMA layer. After Ar/H_2 annealing,[29] the graphene surface appears to be clean under inspection by ambient AFM (**Figure 2.3**). Yet, a thin PMMA layer undetectable by ambient AFM still covers the graphene surface, which requires further *in situ* UHV annealing to remove. It is important to keep in mind that post-transfer annealing can only clean a relatively residue-free surface only; a sample's ultimate cleanliness depends mainly on the transfer.

The third goal – assembling a graphene device without any gate leakage – is governed by the sample mounting and wire bonding steps. When mounting the device on a sample plate, it is critical to electrically disconnect the device from the rest of the sample plate with sapphire flakes; the only electrical contact between the sample plate and the device should be the wire-bonds. Wire-bonding introduces the risk of breaking the device if excessive power is supplied as any form of fracture in the SiO_2 layer (regardless of how small) may lead to gate leakage. Wire-bonding parameters must thus be optimized ahead of time. Because gate leakage may occur not only in the device but also throughout the STM chamber, a large amount of time and resources may be wasted to identify and fix the leakage source. It is important to minimize the risk of gate leakage while assembling a graphene device.

The fourth goal – depositing individual Coulomb impurities – is governed by the calibration steps prior to the deposition. It is imperative to optimize the deposition parameters in the UHV test chamber (and additionally on the Cu(100) surface *in situ*) for a controlled deposition. Purity of the deposition needs to be carefully evaluated with an RGA because random impurities will not only skew the deposition rate measured by QCM but also result in unwanted doping. If the device were irreversibly doped by an unknown impurity, the graphene's response to Coulomb impurities might be undesirably altered.

In addition to these challenges, an STM study may be limited in several ways. In a differential conductance measurement, it is impossible to completely decouple the tip electronic states from the sample states. Even with a well-calibrated tip, it may be challenging to determine the origin of a spectroscopic feature. Moreover, information gained from measurements carried out in UHV and a T = 4 K may not be relevant to devices operated in less ideal conditions.

That being said, STM has many advantages over other techniques. It has not only a high energy resolution (few meV) but also a high spatial resolution (~Å). For comparison, ARPES has a relatively lower spatial resolution (> 1 μm), but a comparable energy resolution (few meV). STM can also be used to manipulate the position of individual atoms on a device to create novel charge configurations. For example, Yang *et al.* created artificial nuclei of charged Ca dimers on a back-gated graphene device with an STM tip and imaged/characterized an atomic collapse state on the graphene surface.[7] With these advantages in mind, STM is one of the most powerful and reliable techniques for characterizing the spatially dependent response of graphene to various perturbations in a well-controlled environment.

STM studies of gate-tunable graphene devices deposited with Coulomb impurities are valuable not only for testing fundamental theories but also for understanding hybrid graphene device applications. They can experimentally verify fundamental predictions about the behavior of massless Dirac fermions in novel systems, which exhibit significantly different behavior compared to charge carriers in conventional systems.[23, 52-54]

Furthermore, such studies can reveal some of graphene's most unexpected characteristics[7], which leads to a deeper understanding of charge carriers in relativistic regimes. New insight into the physical laws that govern graphene systems will be highly beneficial for precision tuning of the properties of hybrid graphene devices. [7, 14, 35, 50]

3 Self-assembled monolayer on graphene/BN device

Monolayer graphene exhibits poor screening, which allows application of an electric field to molecular layers on top of graphene. The gate tunability of self-assembled monolayer molecules allows us to access different molecular orbitals at a fixed bias voltage. Additionally, a graphene/BN surface often has weaker substrate interaction with molecules compared with metals, this suppress the molecule hybridization with the substrate. For example, self-assembled molecular monolayers can preserve the intrinsic vibronic states in their electronic structure.

This chapter presents our results of the gate-tunable electronic structure of self-assembled monolayer molecules on graphene/BN FET devices. We have deposited benzene-derived molecules onto a graphene/BN surface. We found that these molecules self-assemble into a hexagonal lattice at a large scale with high uniformity. Scanning tunneling spectroscopy reveals the LUMO state and the vibronic states of the molecules. By applying a gate voltage, we can shift the Fermi level with respect to the molecular orbital. The content here is based on our published paper: A. Riss et al., "Imaging and Tuning Molecular Levels at the Surface of a Gated Graphene Device", *ACS Nano* **8**, 5395 (2014)[14].

3.1 Introduction

Combining organic molecules with graphene creates new opportunities for fabricating hybrid devices with tailored properties. Previous experiments have shown that electronic[9, 55-71], magnetic,[11, 60, 72] and optical[73-75] characteristics, as well as chemical reactivity[74, 76, 77] of graphene devices can be tuned through molecular adsorption. Such measurements have been performed primarily using electrical conductivity and optical spectroscopy techniques. These measurements, however, do not directly yield local microscopic information regarding the hybrid graphene/molecule interface. Additional electronic structure information on molecule/graphene systems in non-gated configurations has been provided by STM [11, 13, 67, 68, 78-83] and photo-emission spectroscopy [61, 66, 67, 71, 80, 84, 85] experiments, including measurement of the energy location of molecular orbitals. These measurements, however, preclude the hybrid molecule/graphene electronic structure from being electrostatically tuned through the use of a back-gate, and molecular vibronic properties in these systems remain poorly understood[83].

Here we describe a single–molecule resolved STM study of a molecular monolayer absorbed onto a back-gated graphene device that allows both characterization and gate-induced modification of adsorbate properties. 1,3,5-tris(2,2-dicyanovinyl)benzene (CVB) molecules were adsorbed onto a graphene device in UHV and studied via STM spectroscopy at cryogenic temperatures. Hybridized electronic levels of individual CVB molecules on graphene were imaged, and the electronic states were observed to exhibit unexpectedly strong vibronic

satellites. The hybridized vibronic electronic structure of the CVB molecules rigidly shifted in energy as a voltage was applied to the device back-gate, thus allowing the electronic local density of states (LDOS) at fixed sample bias to be switched between different molecular orbitals. Identification of the experimentally observed molecular orbitals was facilitated via density functional theory (DFT)-based simulations which accurately reproduce the orbital structure imaged by STM. The DFT simulations also allow identification of the vibronic satellites through calculation of the CVB electron-phonon coupling. Although CVB molecules exhibit a broad spectrum of vibrational modes, only C-H rocking modes of the CVB molecules having an energy close to 200 meV are seen to contribute significantly to the molecule/graphene electron–phonon coupling. The energy of these modes is in good agreement with the energy spacing of vibronic satellites observed experimentally for CVB on graphene.

3.2 Self-assembled monolayers topography and spectroscopy

Figs. 3.1b-d show STM images of a monolayer-high self-assembled island of CVB molecules on graphene/BN. The Moiré pattern arising from interaction between the graphene lattice and the underlying BN lattice is clearly visible (Figs. 3.1b,c) even though the graphene is covered with a layer of molecules. The molecules form a hexagonal lattice with a lattice constant of $a = 1.13 \pm 0.01$ nm, and isolated defects having triangular shape can be observed. The close-up STM image in Fig. 3.1d shows a spiral-like electronic LDOS associated with the molecules (the opposite chirality was also observed in different islands). The presence of single-molecule vacancies (Figs. 3.1b,c) allows us to assign the location of CVB molecules in the film.

dI/dV spectra were measured while holding the STM tip above the CVB monolayer. Spectra were essentially featureless over the range $-0.5\ \text{V} < V_S < +1.6\ \text{V}$, but for $V_S > 1.6$ V clear resonance features were observed (Fig. 3.2a). For $V_S < -0.5$ V the CVB molecules tended to jump to the STM tip, and so clear STM spectra at sample voltages lower than −0.5 V could not be obtained. The Dirac point of the underlying graphene substrate could be seen when the tip–height was lowered by 4 Å relative to the typical dI/dV measurement tip-height (Fig. 3.2a inset), but this usually led to CVB molecules jumping to the STM tip (thus limiting our low-tip-height measurement capability). The empty state spectrum for larger tip–heights, however, was quite stable up to nearly 3 V, as seen in the spectrum of Fig. 3.2a (this spectrum was reproduced with numerous different tips and samples). Four pronounced peaks can be seen in the spectrum, labeled 1–4. By fitting numerous spectra with Gaussian peaks, we obtain the following energy locations for the four peaks ($E = |e|\ V_S$): $E_1 = 1.86 \pm 0.02$ eV, $E_2 = 2.06 \pm 0.02$eV, $E_3 = 2.28 \pm 0.02$eV, and $E_4 = 2.68 \pm 0.03$eV. The energy differences between peaks 1–2 and peaks 2–3 are similar, whereas the energy difference between peaks 3-4 is twice as big: $E_2\text{-}E_1 = 0.20 \pm 0.03$ eV, $E_3\text{-}E_2 = 0.22 \pm 0.03$ eV and $E_4\text{-}E_3 = 0.4 \pm 0.04$ eV. dI/dV maps taken at sample biases covering the range of the first three peaks ($1.85\ \text{V} < V_S < 2.4\ \text{V}$) show no significant differences in the spatial distribution of the electronic LDOS (Fig. 3.2b, first two panels). However, the dI/dV map obtained at the energy of the fourth peak ($V_S = 2.65$ V) shows a significantly different spatial distribution of the electronic LDOS (Fig. 3.2b, third panel).

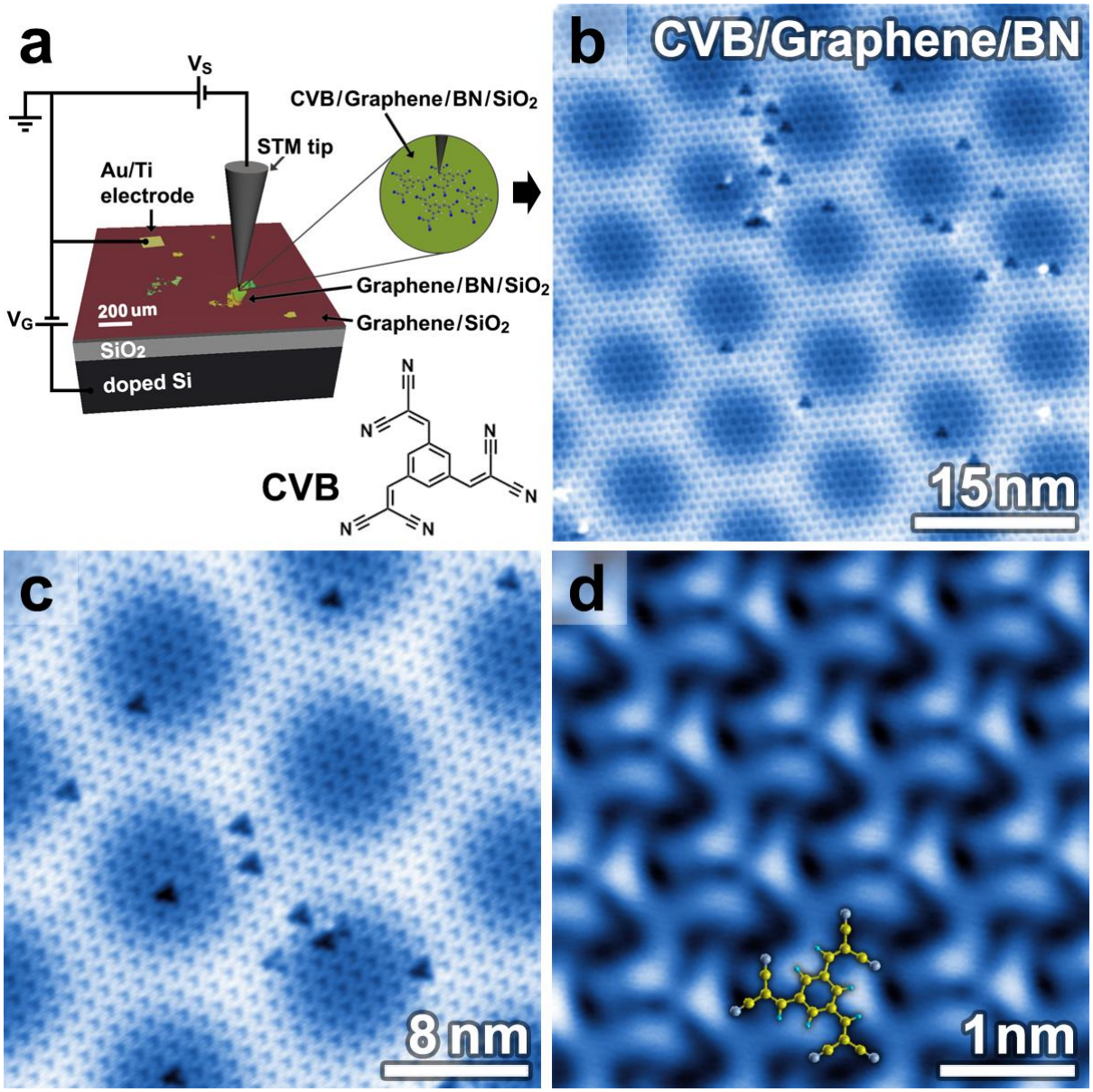

Figure 3.1: CVB molecules on a graphene/BN/SiO2 FET device. **(a)**: Sketch of the back-gated graphene device used in these STM/STS measurements, as well as a model of the CVB molecule. **(b)-(d)** STM images of a monolayer of CVB molecules on graphene/BN show the hexagonal lattice of the CVB molecules at different zoom values (V_S = 2.0 V, I = 10 pA, T = 4 K). Isolated vacancies are observed in (b) and (c).

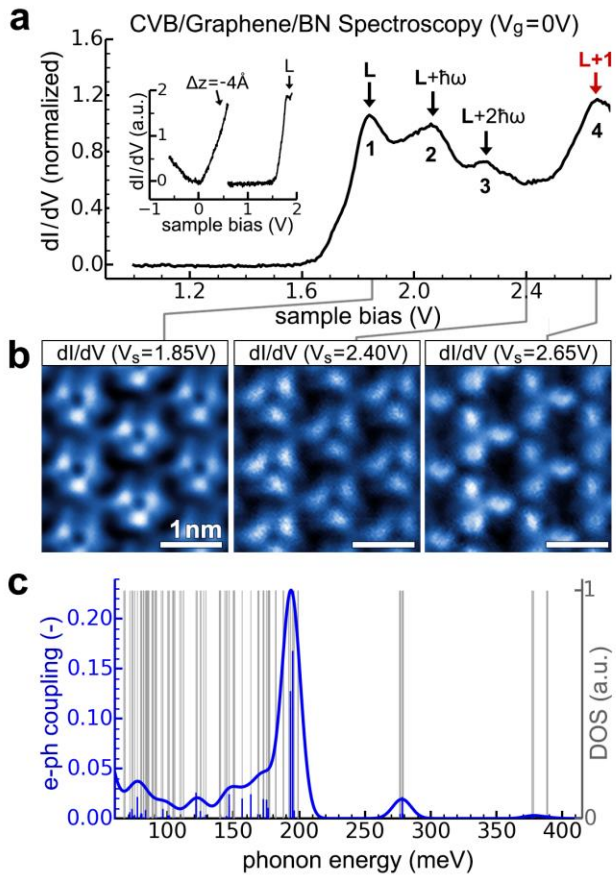

Figure 3.2: STM Spectroscopy of CVB/graphene/BN reveals vibronic response. **(a)** dI/dV spectrum measured with STM tip held above a monolayer of CVB molecules on a graphene/BN FET device ($V_G = 0$). Spectrum is featureless over range –0.5 V < V_S < 1.6 V, but shows four clear molecule-induced resonances (marked 1-4) in the range 1.6 V < V_S < 2.8 V (junction set-point parameters V_S = 2.7 V, I_t =160 pA; the spectrum is normalized by its value at 2.6 V). Inset shows a section of the dI/dV spectrum over the range -0.6 V< V_S < 0.6 V where the tip has been lowered by 4 Å relative to other spectra (junction set-point parameters: V_S = 0.6 V, I_t = 40 pA). Here the Dirac point can be observed at $V_S \approx 0$ V ($V_G = 0$ V). Inset also shows onset of peak 1 (0.6 V < V_S < 1.9 V) for typical junction set-point parameters: V_S = 1.9 V, I_t = 40 pA. Peaks 1 and 4 are interpreted as LUMO and LUMO+1, respectively, while peaks 2 and 3 are interpreted as vibronic satellites of the LUMO (see text). **(b)** Experimental dI/dV maps obtained at voltages V_S = 1.85, 2.4 and 2.65 V ($V_G = 0$ V). dI/dV maps taken in range 1.85 V < V_S < 2.4 V probe the local density of states (LDOS) of peaks 1-3 and look very similar. The dI/dV map taken at V_S = 2.65 V probes peak 4 and yields a LDOS pattern that is different from the pattern observed for peaks 1-3. **(c)** Calculated density of states (DOS) of vibrational modes of CVB molecules on graphene (grey lines), as well as the electron-phonon coupling strength between the CVB vibrational modes and the CVB LUMO state (vertical blue lines). The blue curve shows the calculated electron-phonon coupling broadened with a Gaussian function of width 16 meV.

3.3 Gate tunable electronic structure of self-assembled monolayer

One of the unique aspects of this study is that we were able to perform STM spectroscopy and imaging while modifying the molecule/graphene electronic doping using an electrostatic back-gate. Fig. 3.3a shows dI/dV spectra taken on a CVB monolayer island at two different back-gate voltages (V_G). The black trace shows the spectrum acquired at $V_G = 0$ V while the red trace shows the spectrum taken at a gate voltage of $V_G = 60$ V. The red trace is rigidly shifted by ~ 0.2 V toward lower sample bias, but does not exhibit any other significant changes in its features. We see a similar gate–dependent shift in the Dirac point energy via STM spectroscopy for these graphene devices without molecular layers[86], corresponding to a change in the carrier concentration from $n = 4 \times 10^{10}$ cm^{-2} ($V_G = 0$ V) to $n = 4 \times 10^{12}$ cm^{-2} ($V_G = 60$ V). Next, we acquired dI/dV maps at a fixed sample bias of $V_S = 2.4$ V, but for different gate voltages V_G. The dI/dV map acquired at $V_G = 0$ V (Fig. 3.3b) shows the same features as observed at biases corresponding to peaks 1–3 (Fig. 3.2b, first two panels), but the dI/dV map acquired at $V_G = 60$ V (Fig. 3.3c) exhibits a significantly different LDOS that is similar to what was observed previously for peak 4 (Fig. 3.2b, third panel). The LDOS at this fixed energy with respect to E_F is clearly being toggled between two different molecular orbitals via application of a positive gate voltage (this orbital switching is reversible and has no hysteresis).

We are able to understand our gate–dependent local electronic structure measurements of the hybrid CVB/graphene system through the use of first-principles simulations. The main questions we address here concern the origin and behavior of spectroscopic peaks 1–4 (Figs. 3.2,3.3). To answer these questions we performed density functional theory (DFT) calculations of the combined CVB/graphene network using the PBE exchange correlation functional together with a semi–empirical dispersion correction to take into account van der Waals interaction between the molecules and graphene[87, 88]. After correcting for electron-electron and electron-phonon interactions, we obtained a HOMO-LUMO energy gap of 6.3 eV and a (LUMO)-(LUMO+1) energy gap of 0.8 eV. Although our experimental energy range does not allow us to experimentally verify the HOMO-LUMO gap, we note that the theoretical (LUMO)-(LUMO+1) energy almost perfectly matches the experimental energy difference between peaks 1–4 (ΔE_{14} = 0.82 ± 0.04 eV). This suggests that peak 1 is the CVB/graphene LUMO and that peak 4 is the LUMO+1 state. To further test this hypothesis we calculated the theoretical LDOS of the LUMO and LUMO+1 states and compared it to the experimental dI/dV maps measured at the energies of peaks 1–4. The theoretical LDOS of these different states (Fig. 3.3d,e) is in good agreement with the experimental LDOS maps (first panel and third panel in Fig. 3.2b), thus providing additional strong evidence that peaks 1 and 4 correspond to the system LUMO and LUMO+1 (this procedure also allowed us to confirm the molecular orientation shown in Figs. 3.1 and 3.3).

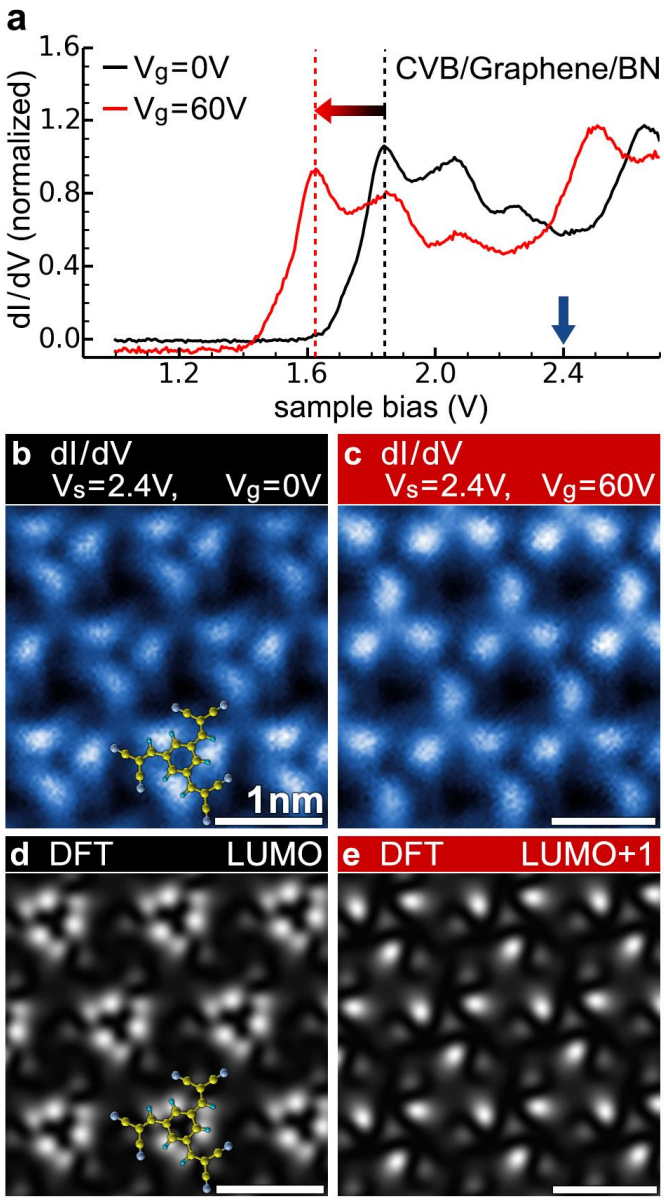

Figure 3.3: Gate-induced shift of the electronic levels of CVB molecules on a graphene/BN FET device. **(a)** dI/dV spectra of CVB/graphene/BN at two different gate voltages: $V_G = 0$ V (black trace) and $V_G = 60$ V (red trace). Increasing the gate voltage to $V_G = 60$ V causes a rigid downward shift of the molecular electronic resonances by 0.2 eV, consistent with the gate-induced shift seen in the Dirac point for graphene/BN devices without adsorbed molecules (spectra are normalized by their respective values at $V_S = 2.6$ V). **(b)** Experimental dI/dV map obtained with $V_S = 2.4$ V and $V_G = 0$ V. **(c)** Same as (b) except that $V_G = 60$ V. **(d)** Theoretical local density of states map of CVB/graphene LUMO state calculated using DFT. **(e)** Same as (d) except for LUMO+1 state. These maps show that changing the device gate voltage allows the STM to access different molecular orbitals for a fixed sample bias.

3.4 Vibrational state of self-assembled monolayer spectrum

An important remaining question is the origin of peaks 2 and 3, which do not appear in the calculated DOS obtained via DFT. These peaks clearly have some relation to the LUMO state, since their experimental dI/dV maps are essentially identical to the dI/dV map for peak 1 (Fig. 3.2b), and they strongly resemble the theoretical LDOS map that was calculated for the LUMO state (Fig. 3.3d). We believe that these additional peaks (#2 and #3) arise due to the existence of vibronic modes of the CVB molecule on graphene. Such modes reflect entanglement between the electronic and vibrational states of a molecule, and have been seen previously in STM spectroscopy of molecules that are decoupled from a metallic substrate[89-91] (single–particle vibronic modes are quenched by direct molecular coupling to a metallic electrode[89, 91]). The spacing between vibronic satellites can be interpreted as the quantum of vibrational energy ($\hbar\omega$) for the molecular vibrational state that is entangled with the electronic orbital. Vibronic states do not appear in DFT calculations of electronic levels because the Born-Oppenheimer assumption prevents mixing of electronic states with vibrational modes.

In order to test this hypothesis, we calculated the theoretical vibrational modes for CVB molecules on graphene, as well as the electron–phonon coupling that exists between the molecular LUMO state and each vibrational mode. While the molecular vibrations are expected to span a wide energy range, the question we seek to answer is whether strong electron–phonon coupling exists for any modes having energy similar to the energy difference between peaks 1 and 2 (0.2 eV) as well as between peaks 2 and 3 (0.22 eV). The grey lines in Fig. 2c show the theoretical vibrational modes of CVB on graphene, calculated within the framework of DFT perturbation theory. As expected, they span a wide energy range, up to 400 meV. The calculated electron–phonon coupling strength between these modes and the CVB LUMO state can be seen as the bold blue trace in Fig. 3.2c (see Supplementary Information Eq. SI-6 for a detailed definition of this quantity). The electron–phonon coupling shows a strong peak at the modes near 200 meV, in good agreement with the experimental value of ΔE_{12} and ΔE_{23} which have an average value of 210 meV. From the calculation we are able to determine that the modes with high electron-phonon coupling at 200meV mainly involve C-H rocking vibrations (which have representations A_1', E_1', and E_2' of the C_{3h} point group) suggesting that this particular vibration is the origin of the vibronic satellites observed experimentally as peaks 2 and 3.

3.5 Theoretical model of electron-phonon coupling

In order to understand the results of STM spectroscopy of molecular systems exhibiting strong electron-phonon coupling, we must be able to calculate the electronic local density of states (LDOS) under these conditions. Here we describe how we are able to calculate the LDOS for molecular adsorbates using density functional theory (DFT) and the 1st order cumulant approximation for the electron-phonon coupling.

The electronic LDOS $\rho(\vec{r},E)$ is related to the measured STM tunneling conductance by

$$\frac{dI}{dV} \propto \rho(\vec{r},E) = -2ImG(\vec{r},E)\,,$$

where G is the electronic Green's function. G is obtained by solving the Hamiltonian

$$H = \sum_j E_j c_j^+ c_j + \sum_\nu \omega_\nu a_\nu^+ a_\nu + \sum_{i\,j\nu} M_{i\,j\nu}\, c^+ c\left(a_\nu^+ + a_\nu\right),$$

where c_j^+, c_j are electron creation and annihilation operators and a_ν^+, a_ν are phonon creation and annihilation operators. We neglect dependence on electron wavevector k, as well as phonon wavevector q. This is based on the observation that the electron and phonon bandwidths are both relatively small. We have also checked that the electron-phonon matrix elements do not change appreciably with wavevector.

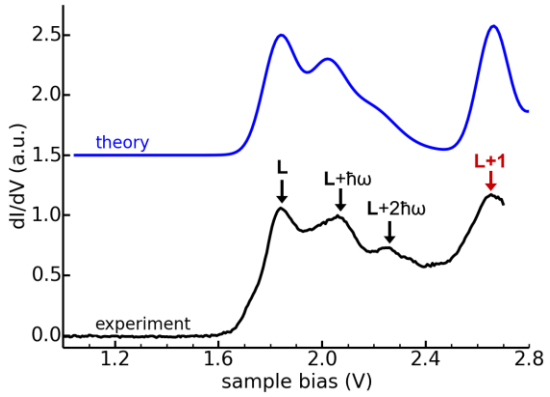

Figure 3.4: Simulated spectral function and experimental scanning tunneling spectrum. Simulated spectral function for the LUMO and LUMO+1 of BTC/graphene within the cumulant expansion framework (blue), and experimentally acquired dI/dV spectrum of BTC/graphene/BN (black). The experimental dI/dV spectrum shows resonances associated with the LUMO ("L"), its vibronic excitations ("L+ħω" and "L+2ħω", respectively), and the LUMO+1 ("L+1").

3.6 Discussion

This vibronic interpretation of the dI/dV spectrum also helps to explain the gate-dependent orbital switching observed in dI/dV maps obtained at a fixed tip-sample bias of V_S = 2.4 V. Here a gate voltage of V_G = 0 V yields a dI/dV map reflecting the LUMO density (Figs. 3.3b,d) while a gate voltage of V_G = 60 V yields a dI/dV map reflecting the LUMO+1 density (Figs 3.3c,e). Within a vibronic picture the fixed tip-sample bias at V_G = 0 V probes the peak 3 resonance which is a vibronic LUMO satellite, whereas gating at V_G = 60 V shifts the tunnel current to the peak 4 resonance which reflects the LUMO+1 state. Electrostatic gating thus allows a fixed tip-sample bias to switch between imaging the LUMO and LUMO+1 orbitals.

In conclusion, we have shown that CVB molecules adsorbed onto a graphene/BN device self-assemble into a hexagonal lattice and develop vibronic peaks that correspond to the A_1', E_1',

and E_2' rocking modes of the CVB carbon-hydrogen bonds. The fact that vibronic peaks can be so readily resolved in the molecule/graphene spectra shown here suggests that substrate-induced lifetime broadening is weak on graphene due to electronic decoupling of adsorbed molecules[89, 91]. Gating the hybrid molecule/graphene device allows electronic switching between two different molecular states (LUMO and LUMO+1) for a fixed tip-sample bias voltage. Extensions of this approach can be envisioned that might allow gate-controlled changes in molecular functionality for hybrid graphene devices to be explored at the single-molecule level.

4 Gate tunable single molecule on graphene

Graphene/BN FET devices enable tuning of molecular orbital energies for self-assembled monolayers through electrostatic gating. This platform allows us to fabricate gate-tunable single-molecule junctions and to control the molecule charge states. However, to switch between such states, we need the energy of the molecular orbital to be within the reach of device's gate tunability. F_4TCNQ, a strong electron acceptor, has a molecular orbital energy close to the Dirac point of graphene. F_4TCNQ can thus be charged when we tune the Fermi level of the graphene device.

This chapter presents our study on controlling the charge states of single molecules on a graphene/BN FET device. We fabricated a three terminal device with the graphene surface acting as an electrical contact and as a gate tunable platform for single molecules. However, these single molecules are unstable on the graphene surface due to weak van der Waals interaction with the graphene. To stabilize these single molecules, we first deposited electronically inert fatty acid molecular islands as an anchor for F_4TCNQ single molecules. We then deposit F_4TCNQ molecules on the graphene/BN FET device. Atomic force microscopy and scanning tunneling spectroscopy reveal the adsorption configuration and the energy of the molecular orbitals. By applying an electric field through a back gate, we can reversibly switch the single molecules between neutral and negative charge states. The electric field also changes the screening behavior of the graphene substrate, which causes renormalization of the molecular orbital energies as a function of gate voltage. The content here is based on our published paper: S. Wickenburg et al., "Tuning charge and correlation effects for a single molecule on a graphene device", *Nature Communications* 7, 13553 (2016)[92].

4.1 Introduction

Creating electronic devices that use single molecules as active elements is a key goal of modern nanotechnology[93-101]. Future progress in this area, however, hinges on developing a better understanding of the fundamental properties of individual molecules in complex electronic environments[95-100, 102-104]. Molecules have been integrated into gated three-terminal electrical devices in the past, allowing continuous tuning and characterization of molecular electronic properties[94-100, 102, 103, 105-109]. Precise interpretations, however, have been made more difficult in these experiments by the fact that local chemical structures have not been well-characterized due to an inability to image individual molecules in device junctions. Single molecules with well-characterized chemical structure, on the other hand, have been studied via two-terminal scanning tunneling microscopy (STM) techniques where electronic properties are *not* tunable via a third external gate electrode[103, 104, 107, 110-113] (as opposed to internal gating/doping generated by local impurity configurations [104, 112, 114]). Some progress has been made at introducing gate electrodes into scanned probe measurements of molecular systems,[14] but gate-tunable control of single-molecule charge states has not yet been demonstrated. Here we combine STM and non-contact atomic force microscopy (nc-AFM) to demonstrate gate-tunable control of the charge state of individual, well-characterized tetrafluoro-

tetracyanoquinodimethane (F_4TCNQ) molecules at the surface of a graphene field effect transistor (FET). This system allows the substrate Fermi energy (E_F) to be continuously tuned all the way through the lowest unoccupied molecular orbital (LUMO) energy of a single F_4TCNQ molecule. Using STM spectroscopy we have determined the gate-dependent energetic evolution of the LUMO level (E_L) and its associated vibronic modes relative to the graphene Dirac point (E_D). We show that the energy alignment between E_L and E_D changes as the substrate charge carrier density is tuned by gating, indicating the presence of electron-electron interactions that renormalize the molecular quasiparticle energy. This is attributed to gate-tunable image-charge screening in graphene and is corroborated by *ab initio* calculations. Our findings reveal that such tunable electronic correlation effects significantly renormalize the electron addition and removal energies for individual molecules incorporated into graphene devices.

4.2 Single molecule STM topography and AFM adsorption structure

The graphene FETs used here were made by transferring graphene grown via CVD techniques onto BN flakes supported by an SiO_2 layer at the surface of a doped Si wafer (the doped Si provides the FET back-gate)[14, 40]. Use of a BN substrate reduces charge inhomogeneity in graphene, allowing us to better probe intrinsic molecule/graphene electronic properties[40]. F_4TCNQ (Fig. 4.1a) was selected for this study because its LUMO state has been predicted to lie close to the graphene Dirac point[115] , thus facilitating molecular charge state tunability. Scanning probe measurements of molecule-decorated devices were performed at $T = 5$ K in ultra-high vacuum. Fig. 4.1b shows an STM image of individual F_4TCNQ molecules adsorbed onto the surface of a graphene/BN device at low coverage. F_4TCNQ exhibits a dog-bone-like shape that resembles the LUMO of an isolated F_4TCNQ molecule, similar to previous measurements of F_4TCNQ molecules on graphene/metal[116-119]. Individual F_4TCNQ molecules are not strongly pinned by the graphene/BN substrate, and so are prone to move quite easily when subjected to the local tip-induced electric fields required for high-resolution STM spectroscopy.

To overcome this problem, we devised an anchoring strategy to immobilize individual F_4TCNQ molecules by using electronically inert 10,12-pentacosadiynoic acid (PCDA) as a molecular anchor (Fig. 4.1a). We evaporated PCDA molecules onto graphene/BN just prior to deposition of F_4TCNQ molecules. Our STM images reveal that PCDA molecules self-assemble into ordered islands on graphene/BN that exhibit straight edges (Fig. 4.1c), consistent with previously reported behavior of PCDA on graphene/SiC[120]. Individual F_4TCNQ molecules anchor nicely to the edge of PCDA islands, as seen in Fig. 4.1c. These edge-anchored F_4TCNQ molecules were sufficiently stable for high-resolution STS and nc-AFM measurements. nc-AFM with a CO tip was used to determine the precise adsorption geometry of F_4TCNQ on the PCDA-functionalized graphene/BN surface, as shown in Fig. 4.1d. In such images contrast is caused by short-range chemical forces, and bright areas exhibiting high frequency shift tend to represent surface regions with higher electron density (such as atoms and chemical bonds[33, 34, 121-123]). The nc-AFM image in Fig. 1d thus reveals the "wire-frame" chemical structure and adsorption geometry of F_4TCNQ molecules attached to PCDA molecular anchors. Our results show that F_4TCNQ molecules align along the armchair direction of graphene and that there is no

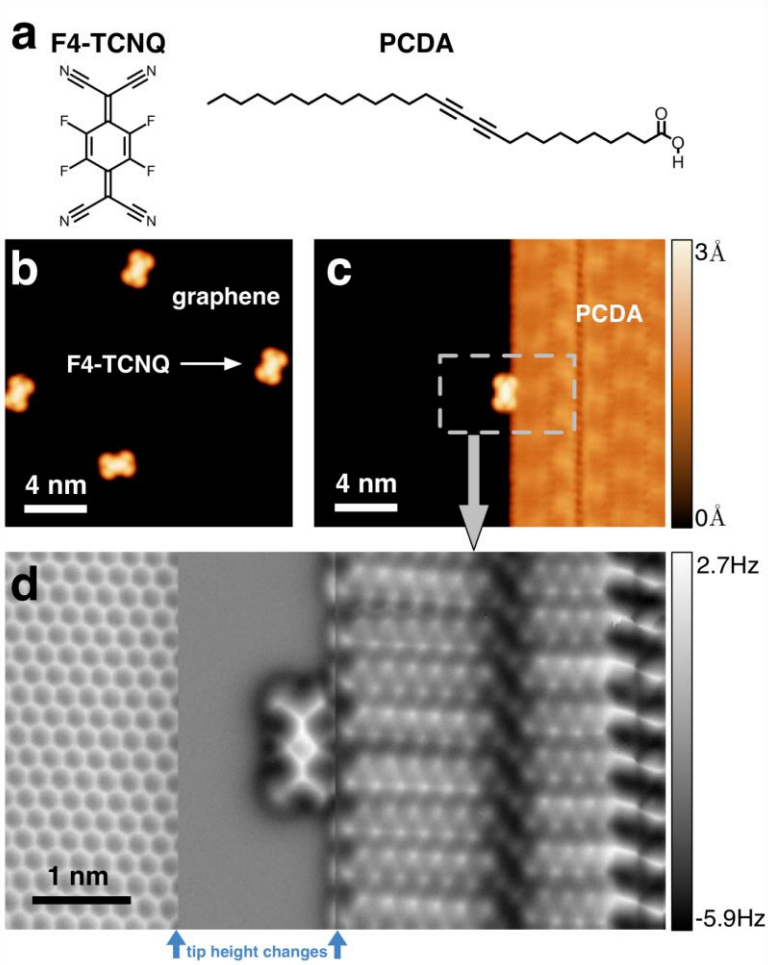

Figure 4.1: STM and nc-AFM images of F4TCNQ and PCDA on graphene reveals molecular adsorption geometry. **(a)** Chemical structure of F4TCNQ and PCDA molecules. **(b)** STM image of F4TCNQ molecules decorating graphene/BN substrate (V_s = 2 V, I_t = 5 pA). **(c)** Deposition of PCDA followed by deposition of F4TCNQ results in well-ordered PCDA islands with isolated F4TCNQ molecules adsorbed at the island edges (V_s = 2 V, I_t = 10 pA). **(d)** F4TCNQ molecular adsorption geometry is shown with single-chemical-bond resolution *via* nc-AFM (qPlus) with a CO-functionalized tip (f_0 =28.7 kHz, Q = 90 k, A = 60pm). The nc-AFM image was taken in constant height mode at three different heights by lowering the tip at the two positions marked by blue arrows (320 pm (left) and 70 pm (right)). Hydrogen atoms can be resolved in the PCDA molecules, as well as triple bonds. F4TCNQ molecules are seen to adsorb with their nitrogen and fluorine atoms close to the terminal hydrogen atoms of PCDA, indicating hydrogen bonding as a likely source of F4TCNQ stabilization. The honeycomb lattice of graphene is clearly resolved. (All images taken at T = 5K).

significant chemical interaction between F_4TCNQ and PCDA (the faint lines seen connecting the F_4TCNQ and PCDA molecules are a common feature for adsorbates bound by weak hydrogen and van der Waals interaction).[123-126]

4.3 F_4TCNQ electronic structure and vibronic mode

We measured the electronic structure of individual F_4TCNQ molecules anchored to PCDA on our graphene/BN devices through the use of STM spectroscopy. The F_4TCNQ electronic structure was not significantly affected by the nearby PCDA as indicated in Fig. 4.2. The inset to Fig. 4.3a shows a typical dI/dV spectrum measured over the range -0.4 V < V_S < 0.4 V (V_S is the sample voltage with respect to the tip) with the back-gate held at V_G = 0 V. Spectroscopy was acquired on the outer edges of the molecule to avoid inelastic tunneling effects [90]. Two broad peaks are visible in the V_S > 0 range, marked L and L'. These peaks are asymmetric, as seen in the adjacent high-resolution dI/dV spectrum in Fig. 4.3a. For V_S < 0 only one peak is seen, marked "charging", which is significantly sharper than the V_S > 0 peaks.[35, 50, 113] The L peak (V_s > 0) is derived from the F_4TCNQ LUMO state. The charging peak (V_s < 0), on the other hand, does not directly indicate a feature in the molecular density of states but rather occurs due to tip-induced band bending as the tip electric field pulls the LUMO state below the Fermi energy (V_S = 0), causing it to fill with charge.[35, 50, 113, 127, 128] We attribute the asymmetric structure of the L and L' peaks to vibronic sidebands, as has been observed in other systems[14, 89-91]. In order to extract the experimental energies of the vibrations involved, we fit the

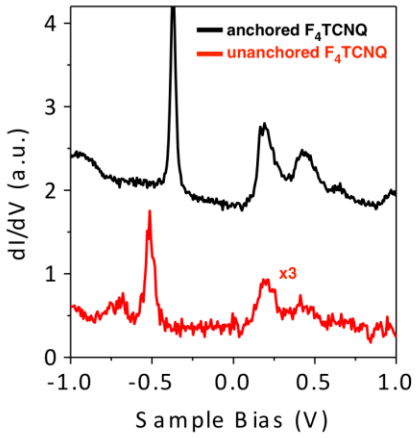

Figure 4.2: Comparison of anchored and free F4TCNQ. Spectroscopy of anchored (to PCDA) and unanchored F4TCNQ molecules on graphene/BN is qualitatively similar. However, for unanchored molecules the initial tunneling current is chosen to be lower to avoid moving the molecule during measurement, resulting in lower signal-to-noise ratio and shifted charging peak. Initial tunneling parameters: Vs = 1 V, It = 15 pA, VAC = 8 mV (anchored), Vs = 1 V, It = 3 pA, VAC = 8 mV (unanchored).

F_4TCNQ spectrum to a sum of Gaussian peaks. The *L* feature is fit well by a peak located at E_L = 61 ± 6 meV (blue dashed line in Fig. 4.3a) along with five other satellite peaks evenly spaced every 37 ± 7 meV (orange dashed lines). The L' feature is similarly fit well by a peak located at $E_{L'}$ = 288 ± 23 meV (purple dashed line) with three additional satellite peaks evenly spaced every 37 ± 7 meV (orange dashed lines).

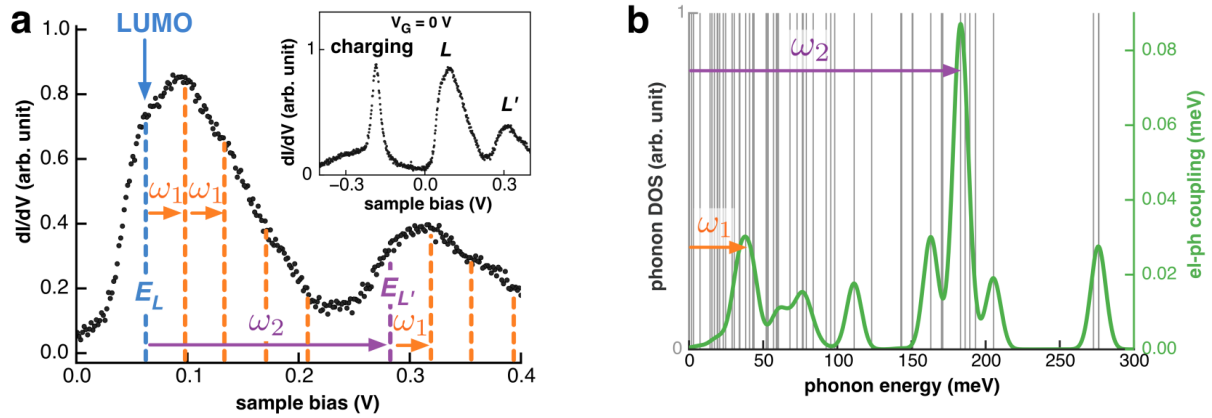

Figure 4.3: STS spectra of F4TCNQ molecules reveal vibronic modes. **(a)** d*I*/d*V* spectrum for a single F4TCNQ molecule on graphene/BN shows two main peaks spaced by ~ 227 meV for V_S > 0, and one peak for V_S < 0. Peaks for V_S > 0 originate from LUMO and vibronic modes while the peak at V_S < 0 originates from tip-induced charging of LUMO level. **(b)** *Ab initio* calculated energies of phonon modes for F4TCNQ/graphene (gray), as well as electron-phonon coupling strength between phonon modes and LUMO state (green curve, broadened by a 12 meV full-width Gaussian). The phonons with highest electron-phonon coupling occur at ω_1~ 34 meV and ω_2~ 183 meV.

To test our hypothesis regarding the vibrational origin and structure of the *L* and *L'* peaks, we calculated the hybridized molecular orbitals and vibrational modes of an F_4TCNQ molecule on graphene, as well as the associated electron-phonon coupling, from first principles. As shown in Fig. 4.3b, numerous vibrational modes exist in the range 0 < E < 300 meV. Calculation of the electron-phonon coupling for each of these modes, however, (Fig. 4.3b, green curve) shows that the strongest coupling occurs at $\omega_1 \approx 34$ meV and $\omega_2 \approx 183$ meV. These energies correspond to a uniaxial stretching mode with A_g symmetry (ω_1 = 34 meV) and a breathing mode of the inner carbon ring also having A_g symmetry (ω_2 = 183 meV). The calculated energies agree reasonably well with the experimental energy spacing of the peaks extracted from within the L and L' features of Fig. 4.3a (37 ± 7 meV) as well as the energy difference $E_{L'} - E_L$ = 227 ± 24 meV. A more detailed analysis involving a cumulant expansion to calculate the spectral function including vibronic modes also agrees with our measured spectra, supporting the vibronic interpretation of the spectral lineshape.

4.4 Gate tunable charge state of a single F_4TCNQ molecule

A unique aspect of this study is that we are able to reversibly control the charge state of a single F_4TCNQ molecule by continuously tuning the substrate Fermi level past the LUMO energy level via application of an electrostatic back-gate. Fig. 4.4 shows STM d*I*/d*V* spectra of a single anchored F_4TCNQ molecule at two different back-gate voltages (V_G). Here we label the empty and occupied LUMO orbital as $LUMO^0$ and $LUMO^-$, respectively. The blue curve acquired at V_G = -50V shows the LUMO level well above E_F and thus empty ($LUMO^0$), resulting in a neutral molecule at this gate voltage. In contrast, the red d*I*/d*V* trace acquired at V_G = +30 V shows the LUMO well below E_F and thus filled by an electron, causing the molecule to become negatively charged ($LUMO^-$). A notable difference between the red and blue curves is that the vibrational sidebands for the $LUMO^-$ state extend *downwards* to more negative V_S values compared to the sidebands for $LUMO^0$ which extend *upwards* to more positive V_S values. This can be explained by the fact that higher-energy electron-like vibronic excitations (for $LUMO^0$) occur at higher values of V_S, whereas higher-energy hole-like vibronic excitations (for $LUMO^-$) occur at lower values of V_S. Our first-principles calculation of the spectral function using a cumulant expansion[129] confirms this intuitive electron-hole symmetry and reproduces the observed vibronic spectra.

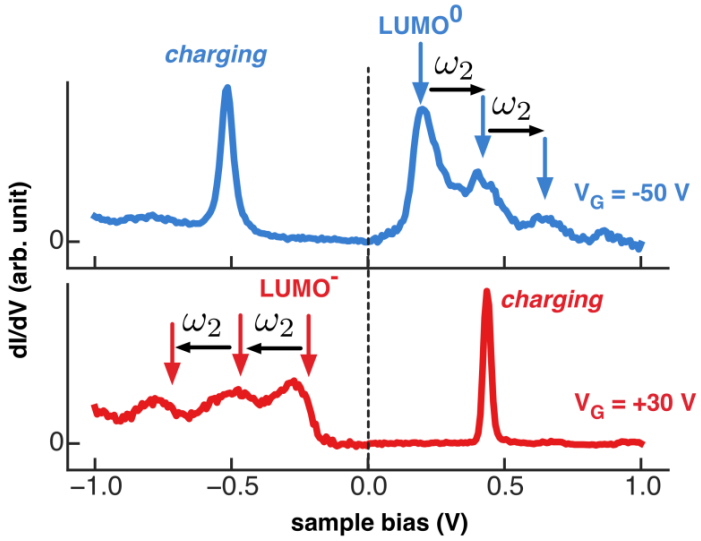

Figure 4.4: Gate tunable charge state of a single F4TCNQ molecule spectrum. dI/dV spectrum of F4TCNQ/graphene/BN for VG = -50V (blue) shows F4TCNQ vibronic states for a neutral molecule (LUMO0). dI/dV spectrum of the same molecule at VG = 30V (red) shows that vibronic states for a charged molecule (LUMO-) switch their energy alignment from increasing energy ordering to decreasing energy ordering when the charge state is switched by the gate (the portion of the blue (red) curve below (above) EF has been scaled by 0.4 (0.2) to fit on the plot). Initial tunneling parameters: It = 15 pA , Vs = 2 V, VAC = 8 mV).

Our ability to gate the substrate of an adsorbed molecule allows us to address the fundamental issue of the importance of electron-electron interactions for molecule/substrate systems. We do this by measuring how the energy level of the molecular orbital changes relative to the graphene band structure as E_F is swept by the gate. In the absence of electron-electron interactions we expect the position of the molecular level relative to E_D to be independent of E_F. If, on the other hand, electron-electron interactions play a significant role then we expect the LUMO energy (E_L) to shift relative to E_D as E_F is tuned. We measured this effect by acquiring d*I*/d*V* spectra both *on* a single F_4TCNQ molecule (to obtain E_L) and *off* the molecule (to obtain E_D) as a function of gate voltage. Fig. 4.5a shows a plot of the resulting "on molecule" d*I*/d*V*

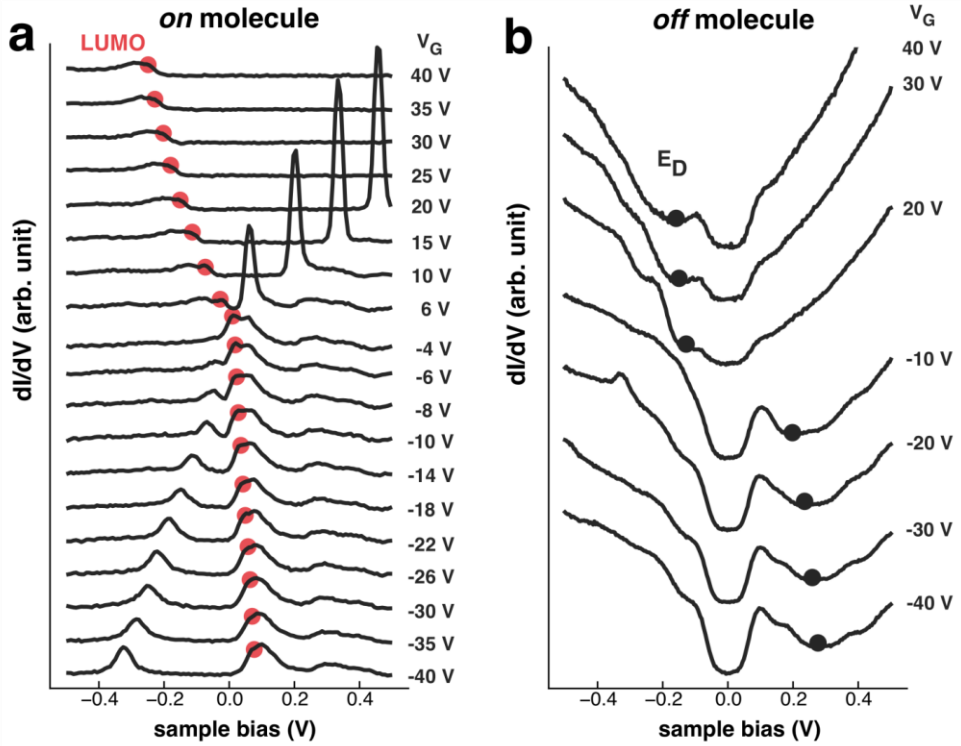

Figure 4.5: Gate-dependent STS of individual F4TCNQ molecule on graphene/BN. **(a)** d*I*/d*V* spectra obtained with STM tip held over a single F4TCNQ molecule recorded at different gate voltages show that the LUMO state and vibronic sidebands shift relative to E_F as the gate is swept. Red dots mark energy locations of the LUMO state at different gate voltages, extracted by fitting a sum of Gaussian peaks to the dI/dV spectra (initial tunneling parameters: I_t = 15 pA , V_s = 1 V, V_{AC} = 8 mV). **(b)** d*I*/dV spectra obtained with the STM tip held over a bare patch of graphene/BN near an F4TCNQ molecule (distance = 4 nm) recorded at different gate voltages show dependence of Dirac point energy (E_D) on gate voltage. Black dots mark Dirac point obtained by fitting inverted Gaussians to the minimum of each spectrum. Final E_D values are obtained by subtracting the inelastic phonon energy of 63meV from these measured features[36, 86] (initial tunneling parameters: I_t = 60 pA, V_s = 0.5 V, V_{AC} = 12 mV).

spectra as a function of gate voltage (-40 < V_G < +40), while Fig. 4.5b shows a plot of the "off molecule" spectra (i.e., for bare graphene). The on-molecule spectra show the molecular LUMO level continuously sweeping from an empty orbital state ($LUMO^0$) for $V_G < 0$ to a filled orbital state ($LUMO^-$) for $V_G > 0$. Similarly, the off-molecule spectra show the graphene Dirac point sweeping from above E_F for $V_G < 0$ (the p-doped regime) to below E_F for $V_G > 0$ (the n-doped regime). To extract the experimental gate-dependent values of E_L, we fit the dI/dV spectra in Fig. 4.5a with sums of Gaussians. The resulting LUMO energies are shown in Fig. 4.5a at the red dot locations. The gate-dependent E_D values were obtained from the spectra of Fig. 4.5b by fitting inverted Gaussians to the prominent local minimum of each spectrum (resulting in the black dots shown in Fig. 4.5b).

4.5 Gate tunable image charge effect of F_4TCNQ on a graphene device

Fig. 4.6 shows a direct comparison of the experimental E_D and E_L values as a function of gate voltage (because E_D is difficult to obtain for some gate voltages we use values here that are obtained by fitting a characteristic square root function to the data of Fig. 4.5b. For small gate

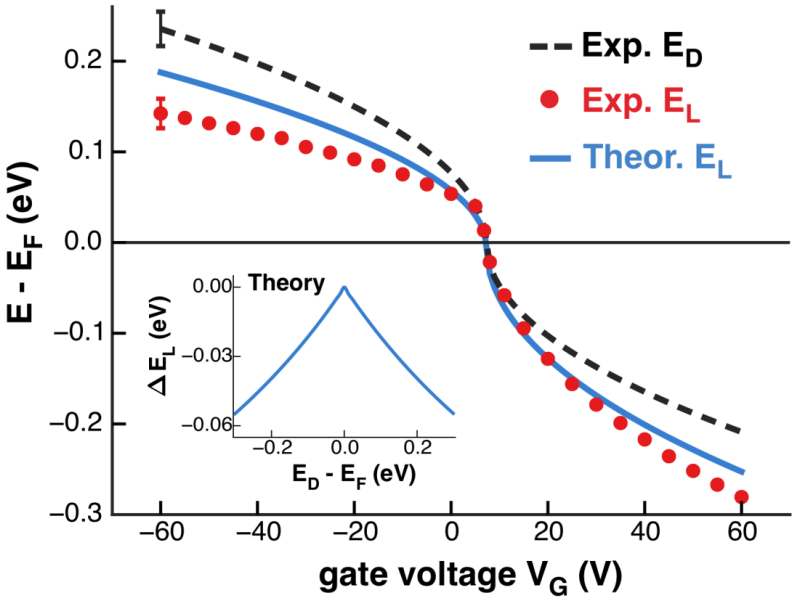

Figure 4.6: Energy positions of E_D and F_4TCNQ LUMO as a function of gate voltage. The dashed line indicates the position of E_D, the red dots indicates F_4TCNQ LUMO energy, and blue curve indicates the theoretically predicated energy. The experimental error in the LUMO energy is estimated as the mean half-width of the Gaussian fits to the F_4TCNQ spectra (16 meV). The experimental error in E_D is estimated using the fit of the measured E_D to the square root dependence of E_D vs. V_G (the rms of the fit residuals = 19 meV). **Inset**: theoretical energy renormalization of the LUMO level due to interaction of LUMO charge with induced graphene image charge as a function of E_F.

voltage (low charge carrier density) E_D and E_L are seen to lie almost directly on top of each other. When the gate voltage magnitude is increased (resulting in higher charge carrier density), however, the values diverge, separating by as much as 100 meV at the highest gate voltage (corresponding to a charge carrier density of ~3×10^{12} /cm^2 at V_G = 60 V). The energy difference between E_D and E_L (E_D - E_L) is seen to increase monotonically with increasing charge carrier density for both electrons and holes, suggesting that electron-electron interactions play a role in determining E_L for this adsorbate system. The observation that E_D-E_L does not depend on the polarity of graphene charge carriers rules out simple band bending as an explanation for the energy shift, since band bending would shift E_L to higher energies when E_L - E_F > 0, opposite to what is observed.[35, 113, 130]

We are able to explain this behavior as the result of Coulomb interaction between charge added to an F_4TCNQ molecular orbital (*via* tunneling) and the electronic polarization that it induces in the graphene substrate. This many-electron interaction always lowers the energy of a system since the interaction between charge added to an adsorbate and its image charge in the substrate is always attractive. Such effects are well known to reduce the energy gap between affinity and ionization levels for adsorbates on conventional substrates[105, 131-133]. For an adsorbate on graphene this effect is expected to be tunable since polarizability depends on the density of states at E_F, which is readily changed by gating a graphene device.

4.6 Calculation of the image charge effect

In order to estimate the expected magnitude of this effect for comparison to our data, we calculated how the F_4TCNQ LUMO energy level is renormalized via screening within many-body perturbation theory (standard DFT treatments of the Kohn-Sham eigenvalues do not take this non-local effect into account). This was accomplished by modeling an electron that has tunneled into the empty LUMO level as a point charge located a distance z^* above the graphene plane (z^* is estimated to be 3 Å from our *ab initio* calculations of F_4TCNQ/graphene, in reasonable agreement with the tip-height change during AFM measurements (Fig. 1d)). The point charge exposes the graphene substrate to a Coulomb potential, $\phi_{ext}(\vec{r})$, which induces screening charge density, $n_{ind}(\vec{r})$, in the graphene. We calculated $n_{ind}(\vec{r})$ and the change it causes to the electrostatic potential, $\phi_{ind}(\vec{r})$, within linear response theory using the RPA dielectric function of graphene[53] (the BN substrate was taken into account by choosing a background dielectric constant of $\epsilon_{bg} = 2$, see Supplementary Information). The screening-induced lowering of the LUMO energy, ΔE_L, was estimated by evaluating $\phi_{ind}(\vec{r})$ at the location of the point charge above the graphene surface thus yielding $\Delta E_L = -\frac{1}{2} e\phi_{ind}(z^*)$.[131] The inset to Fig. 4.6 shows the calculated ΔE_L values as a function of E_F. For $E_F = E_D$ the energy correction is smallest since graphene has no density of states at the Fermi level when E_F is aligned to the Dirac point. As E_F shifts away from E_D, the energy correction increases equally for both electron and hole-doping since the carrier RPA dielectric function for graphene is electron-hole symmetric. The near-linear dependence of ΔE_L on E_F stems from the linear graphene

density of states, $\rho(E)$, and the fact that the graphene electronic susceptibility is proportional to $\rho(E_F)$.

The renormalization of molecular levels due to image charge corrections caused by the presence of a (semi-infinite) substrate has been investigated by Neaton, Hybertsen and Louie[131]. These authors find that the correction of the quasiparticle levels of a molecule is given by

$$\Delta E_{QP} = -\frac{1}{2}\delta U \text{ , for a completely filled level}$$
$$\Delta E_{QP} = +\frac{1}{2}\delta U \text{ , for an empty level,}$$

with $\delta U = \langle \psi_M^2 | \Delta W | \psi_M^2 \rangle$ (ΔW denotes the change in the screened Coulomb interaction due to the presence of the substrate and ψ_M denotes the wave function of the molecular orbital). Typically, the presence of a substrate increases the screening and thus δU is *negative*.

Before we apply this theory to F4TCNQ on graphene, we discuss the image charge correction for a molecular level that is occupied by a single electron. The theory of Neaton, Hybertsen and Louie can be generalized to this case by noting that the energy needed to remove an electron from this system, i.e. the ionization potential (IP), equals the energy required to add an electron to the molecule with an empty level, i.e. its electron affinity (EA), because

$$E_{QP}^{IP}(N=1) = E^N - E^{N-1} = E^{\tilde{N}+1} - E^{\tilde{N}} = E_{QP}^{EA}(\tilde{N}=0).$$

The energy renormalization of the empty level E_{QP}^{EA}, however, is given by the theory of Neaton, Hybertsen and Louie [note that $E_{QP}^{IP}(N-1) = E_{QP}^{EA}(\tilde{N}=0)$ also without the substrate and therefore the substrate-induced renormalization must be the same for $E_{QP}^{IP}(N=1)$ and $E_{QP}^{EA}(\tilde{N}=0)$].

We illustrate the result of the previous paragraph for the case of F_4TCNQ on doped graphene. In the neutral F_4TCNQ molecule the LUMO is completely empty. We assume that the presence of an extra electron in the LUMO of the molecule (assumed to be located a distance z^* above the graphene plane) gives rise to an extra contribution to the total energy of $-|e|Q(\epsilon_F)/(2z^*)$, where $|e|$ denotes the absolute magnitude of the electron charge and $Q(\epsilon_F) > 0$ denotes the doping-dependent image charge induced in the graphene.

For negative gate voltages, the LUMO is empty. The cost of transferring an electron from the tip into the empty LUMO is given by

$$E(add\ electron) = E_{tot}(1\ el, \epsilon_F) - E_{tot}(0\ el, \epsilon_F) - \epsilon_F,$$

where $E_{tot}(1\ el, \epsilon_F)$ and $E_{tot}(0\ el, \epsilon_F)$ denote the total energy of the molecule plus graphene system with a singly occupied or an empty LUMO, respectively. We can approximate these total energies as

$$E_{tot}(0\ el, \epsilon_F) = E_{gra}(\epsilon_F) + E_{mol}(0\ el, \epsilon_F)$$

and

$$E_{tot}(1\ el, \epsilon_F) = E_{gra}(\epsilon_F) + E_{mol}(1\ el, \epsilon_F) - \frac{|e|Q(\epsilon_F)}{2z^*},$$

where E_{gra} denotes the energy of graphene without the molecule and E_{mol} denotes the energy of the molecule without the graphene. Inserting this into the equation for $E(add\ electron)$ yields

$$E(add\ electron) = E_{mol}(1\ el, \epsilon_F) - E_{mol}(0\ el, \epsilon_F) - \frac{|e|Q(\epsilon_F)}{2z^*} - \epsilon_F.$$

This demonstrates that the image charge interaction reduces the energy of transferring an electron from the tip to the molecule.

For positive gate voltages, the LUMO is occupied by one electron and the energy for transferring this electron from the LUMO to the tip is given by

$$\begin{aligned} E(remove\ electron) &= E_{tot}(0\ el, \epsilon_F) - E_{tot}(1\ el, \epsilon_F) + \epsilon_F \\ &= E_{mol}(0\ el, \epsilon_F) - E_{mol}(1\ el, \epsilon_F) + \frac{|e|Q(\epsilon_F)}{2z^*} + \epsilon_F, \end{aligned}$$

indicating that the image charge interaction increases the energy needed to remove the electron from the LUMO.

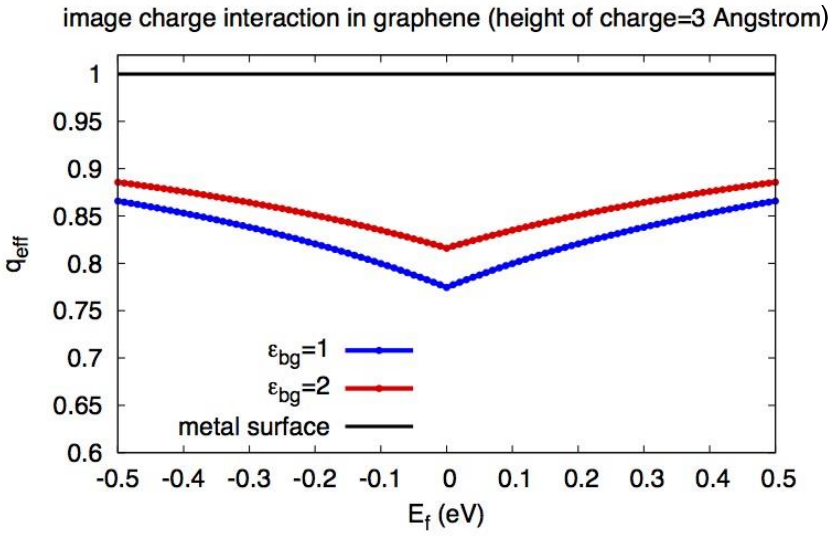

Figure 4.7: Size of image charge. The graphene image charge as function of the Fermi level for different substrates induced by a negative point charge located 3 Angstrom above the graphene plane. The blue curve shows the image charge for graphene in isolation ($\epsilon_{bg} = 1$) and the red curve shows the result for graphene on BN. For comparison, we also show the image charge of a metallic substrate (black line).

To calculate the size of the induced image charge in doped graphene, we model the extra electron in the LUMO level as a point charge located a distance z^* above the graphene plane (which is assumed to be perfectly two-dimensional) and find for the Fermi-level dependent quasiparticle energy

$$E_{QP}(\epsilon_F) - E_{QP}(\epsilon_F = 0) = -\frac{1}{2}[\delta U(\epsilon_F) - \delta U(0)]$$
$$= -\frac{1}{2}\int_0^\infty dq \left\{\epsilon_q^{-1}(|\epsilon_F|) - \epsilon_q^{-1}(0)\right\} e^{-2qz^*},$$

where ϵ_q denotes the graphene dielectric function, which depends only on the absolute magnitude of the Fermi energy. As a consequence, the LUMO level renormalization is symmetric around the Dirac point $\epsilon_F = 0$. Using the long wavelength limit of the dielectric function of graphene (see below), a simple scaling argument shows that $\Delta E_{QP}(\epsilon_F) = \epsilon_F\, F(k_F z^*)$ with k_F denoting the Fermi momentum. For small doping $k_F z^* \ll 1$ and $\Delta E_{QP}(\epsilon_F) \approx \epsilon_F\, F(0)$.

4.7 Discussion

In order to compare the calculated ΔE_L to spectroscopy taken on individual F_4TCNQ molecules, we can add it to our gate-dependent measurements of E_D (taking into account a small offset constant observed experimentally at charge neutrality). In the absence of any screening effects ($\Delta E_L = 0$), this would result in $E_L \approx E_D$ at every gate voltage (the simple "rigid shift" case). The Coulomb-induced renormalization effects described above, however, cause this procedure to result in a nontrivial shift of E_L with respect to E_D as a function of gate voltage. Figure 4 shows a plot of the resulting renormalized E_L value (blue curve) as a function of gate voltage compared to the experimental E_L values (red dots). For small gate voltages the renormalized E_L value coincides with E_D, but as the gate voltage (and carrier density) magnitude is raised the calculated E_L values fall increasingly downward compared to E_D, just as seen for the experimental E_L values. The model thus captures both the observed independence of the LUMO renormalization on the graphene carrier type (electrons or holes) and also reproduces the general magnitude of the molecular orbital energy change. The match is not perfect (the experimental drop in E_L tends to be larger than the calculated ΔE_L), but is reasonable considering that the calculation has no adjustable parameters. One possible source for the discrepancy between theory and experiment are intra-molecular electron-electron interactions, which are not accounted for in the simple image charge model. We have examined the effect of these interactions on the LUMO energy using an Anderson model approach and find that they do lead to additional LUMO energy renormalization, but smaller in magnitude than the image charge effects.

In conclusion, we have demonstrated reversible tuning of the charge state of individual F_4TCNQ molecules using an electrostatically back-gated graphene device. The molecular adsorption geometry was imaged via nc-AFM with single-chemical-bond resolution and the gate-dependent molecular electronic structure was determined via STM spectroscopy. We find that molecular vibronic modes can be switched from electron-like energy alignment to hole-like energy alignment depending on the tunable molecular charge state, in agreement with cumulant-expansion theory. We additionally observe a non-rigid shift in the LUMO energy relative to the Dirac point as a function of gate voltage that can be explained by many-electron interaction renormalization of the LUMO energy caused by tunable substrate polarization effects.

5 One-dimensional charged molecular array on graphene

A charged single molecule allows us to generate a localized Coulomb potential on the graphene surface. By engineering molecular self-assembly configurations, we can design periodic potentials with different geometries on the surface. When the density of charged molecules is above a critical threshold, it is predicted that a localized state for Dirac fermions on graphene can form. The localized state can be explained through the supercritical picture of Dirac fermions. The supercritical potential induced by negatively charged molecules can cause the electronic holes to spiral towards and then away from an artificial nucleus formed by the charged molecules.

This chapter presents our investigation of one-dimensional potentials on graphene formed by a linearly charged molecular array. Here, we use fatty acid molecular islands as a template to guide charged molecules into a self-assembled linear geometry. The charge states of the molecules are controlled by the electrostatic gate on a graphene/BN FET device. Molecular arrays with different spacing are achieved by controlling molecule deposition and desorption time. Scanning tunneling spectroscopy reveals that a new type of supercritical state emerges as we increase the charged molecule density along the linear array.

5.1 Introduction

Charge carriers in graphene behave as massless relativistic particles similar to electromagnetic waves, which make graphene a fertile playground not only for testing exotic relativistic quantum phenomena but also for realizing quantum electron optics. The future progress in this field hinges on the ability to create well-define electron resonant cavities allowing for the manipulation of electronic waves in graphene with a high accuracy. However, quantum engineering of electronic wavefunctions in mesoscopic-scale graphene remains a challenge owing to the difficulty in creating sharp electrostatic barriers on the order of electron coherence length. Mesoscale graphene pn-cavities have been successfully realized by patterning gate electrodes or positioning of a STM tips, which however suffer from the diffusive nature of potential landscape under electrostatic gates. Instead, manipulation of atomic-scale charge impurities in graphene have proven to be effective in engineering supercritical Coulomb potentials whereby charge carrier in graphene can be confined in atomic collapse states. Apparently there is a gap between mesoscale and atomic-scale quantum electronic confinement in graphene, which must be bridged to allow Moore's law to progress to the ultimate scale. Here, we report the bottom-up synthesis of a series of charge arrays on a gated graphene device. Each charge array adopts a 1D line geometry with a precision that has not been previously available in nanoscale systems. The molecular charge arrays undergo a transition from subcritical to supercritical regime as the packing density is increased. We found that supercriticality emerges below the critical spacing in molecular charge arrays. In addition, we demonstrate that a new

type of 1D supercritical state can be switched on/off by tuning the charge state of individual molecules in a controlled manner via electronic-field back-gating.

5.2 Fabrication of one-dimensional molecular arrays

Our experiments were performed on a FET device consisting of a CVD-grown graphene monolayer deposited on a hexagonal boron nitride (BN) flake, with both lying on a SiO_2 substrate whose doped bottom portion is used as a back-gate. The use of a BN substrate significantly reduces surface roughness and charge inhomogeneity in graphene[39], allowing us to probe the local electronic response of graphene to a charged molecular array with high precision. F_4TCNQ (Fig. 5.1a) was used in this study because its charge state can be conveniently and reliably switched on and off *via* the back-gate, as demonstrated in our previous study[92]. Scanning probe imaging and spectroscopy measurements of molecule-decorated graphene FET devices were performed at T = 4.6 K in ultra-high vacuum.

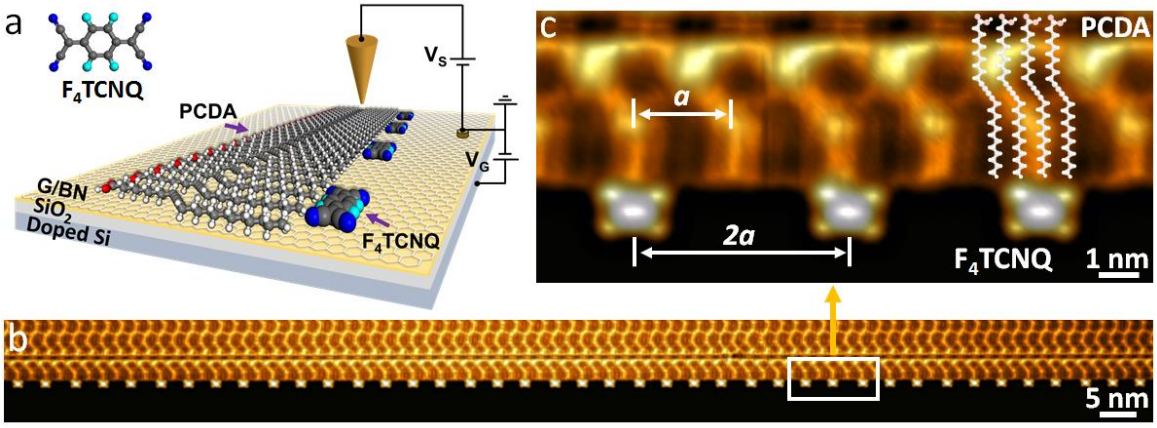

Figure 5.1 STM images of one-dimensional F_4TCNQ molecular arrays synthesized on a gated graphene device (a) Schematic illustration of an edge-templated synthesis of F_4TCNQ molecular arrays on a gated graphene FET device. (b) STM image of the formation of an equally-spaced F_4TCNQ molecular array (2a structure) along the edge of PCDA islands. (c) A close-up view of the edge-anchored F_4-TCNQ molecular array (2*a*) Note: *a* is the moiré lattice constant of the PCDA monolayer island on graphene/BN as indicated in c.

1D molecular charge arrays were fabricated with an edge-templated self-assembly protocol that allows the precise alignment of individual molecules. Electronically inert 10,12-pentacosadiynoic acid (PCDA), a linear chain-like molecule, was first chosen to self-assemble into ordered monolayer islands with straight edges that serve as an ideal 1D template for the patterning of F_4TCNQ molecular arrays (Fig. 5.1a). Our STM image reveals that these islands display a regular moiré pattern with a lattice constant of a ~ 1.92 nm, arising from the lattice mismatch between graphene and the PCDA film (Fig. 5.1c). When F_4TCNQ is subsequently deposited at room temperature, we consistently and reproducibly observe the preferential adsorption of individual molecules at the site of the PCDA edge that exhibits the bright

protrusion (moiré hump regions). Each F_4TCNQ lies flat on graphene, and a close-up STM image in Fig. 1c reveals its adsorption geometry and relevant length scales. The precise moiré undulation, together with the atomically sharp linearity of the edge, promotes the assembly of 1D molecular arrays that remain strictly periodic over a few hundreds of nanometers, as shown in Fig. 5.1b. Interestingly, this edge templating mechanism can be used to achieve arrays with a range of different periodicities (i.e., inter F_4TCNQ distance). The smallest that we discuss in this work is the relatively densely-packed array with an inter-molecular spacing (d) of ~3.85 nm, equivalent to twice the moiré lattice constant of the PCDA islands (thus termed as the "*2a"* charge array, cf. Fig 5.1c). Control over the dosage allows us to obtain higher periods, in multiples of a, as demonstrated in Figs. 5.3a-d for the cases up to "$d = 5a$". We thereby fabricated a series of molecular arrays with tunable linear density on a gated graphene device.

The unique aspect of this study is that, not only are we able to manipulate the linear density of the F_4TCNQ array with very high uniformity over large distances, but can also, simultaneously and reversibly, control the charge on each individual F_4TCNQ molecule by continuously moving E_F across the LUMO energy with the back-gate. The end results are, to the best of our knowledge, the first geometrically and electrostatically tunable arrays of charge on graphene. Scanning tunneling spectroscopy (STS) measurements taken directly above individual F_4TCNQ molecules reveal that each remains negatively charged for gate voltages in the range of $0 < V_G < 60$ V since the LUMO peak lies below E_F and is filled by one electron[92]. Moreover, the charge of F_4TCNQ is seen to remain stable in the range $V_G \geq 30$ V within our measurement conditions ($-0.5 < V_S < 0.5$ V) for various molecular arrays with a periodicity down to $2a$. In the following, unless otherwise specified, V_G has been set at 30 V which ensures that the molecular arrays under consideration are charged, with approximately one unit of charge per molecule.

5.3 Local spectroscopy in the near field of the array

To investigate whether and how these arrays of charge affect the Dirac quasi-particles in graphene, we probed the energy-dependent local density of states (LDOS) in the vicinity of several arrays through STS measurements (dI/dV) at different lateral distances from the center of a single F4-TCNQ molecule (Figs. 5.3e-h). dI/dV point spectra shown here were acquired at the same tip height to eliminate the exponential change in the differential conductivity that occurs with tip-sample distance and thus allow a direct quantitative comparison of the spectra at different locations. All our dI/dV spectra exhibit the wide gap feature (~130 meV) pinned at E_F characteristic of STS in graphene, and arising from phonon-assisted inelastic tunneling[36]. The local minima at a sample bias of around V_S = -0.18 V signal the neighborhood of the Dirac point energy (E_D). Taking the inelastic gap into account, this places the Fermi energy at E_F - $E_D \approx 85$ meV and corresponds to a carrier density of $n_e \approx 7.0\times10^{11}$ cm^{-2}. However, this should be taken as an estimate only because its placement right beside the characteristic resonant feature and on the verge of the inelastic gap makes a precise identification of E_D difficult.

In order to understand the behavior displayed by the curves in Figs. 5.3 e-h we should first discuss the features that an isolated molecule imprints in the dI/dV of graphene nearby. Traces taken at different distances from an isolated molecule are shown in Figure 5.2 and exhibit the characteristic particle-hole asymmetry and distance dependence theoretically expected for

graphene in the vicinity of a negatively charged Coulomb center [6, 22, 23, 134]. The asymmetry and distance dependence of d*I*/d*V* seen here near F_4TCNQ are the reflection with respect to E_F of the behavior well established in experiments involving positively charged impurities [7, 35, 50, 135]. The imprint of an isolated F_4CNQ in graphene under these gating conditions is therefore that of a (negatively) charged center which, from the profile of the traces, lies in the undercritical regime of a charged impurity in graphene[23, 92].

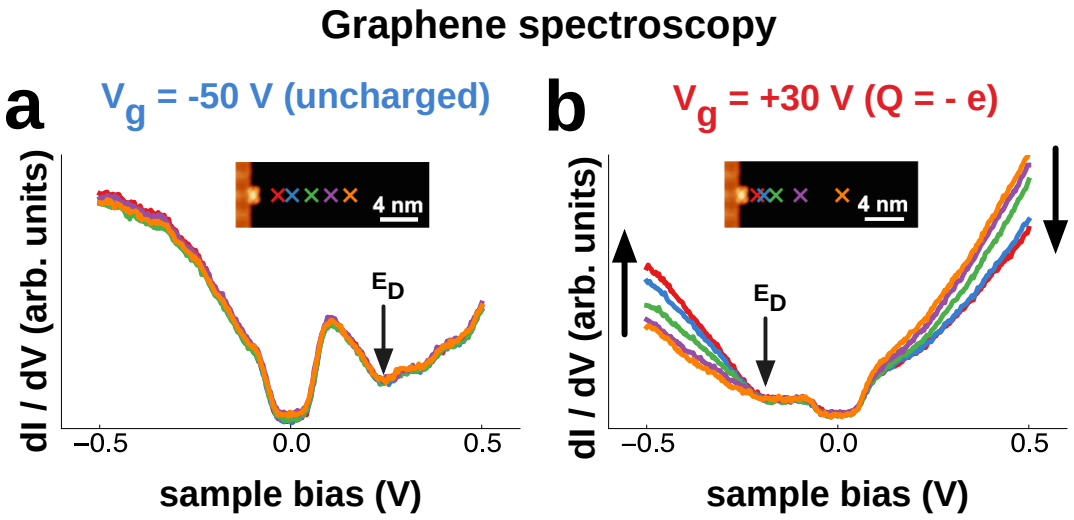

Figure 5.2: Graphene spectroscopy near a single molecule reveals the molecule charge state. (a) dI/dV on graphene near an F4TCNQ molecule at Vg = -50 V shows no distance dependence, indicating that the molecule is uncharged.[50] (b) For Vg = +30 V, dI/dV spectra on graphene show an asymmetry developing as the tip moves close to the molecule with dI/dV intensity decreasing above ED and increasing below ED. This is an indication of charge located at the molecule, which we determine to be $q \approx -e$ by comparison to previous results9 (initial tunneling parameters: It = 60 pA, Vs = 0.5 V, VAC = 12 mV).

When assembled in the one-dimensional arrays shown in Figs. 5.3a-d, the LDOS in adjacent regions of graphene is substantially modified with increasing charge packing density. The particle-hole asymmetry associated with the negative charges is clearly retained in all the array periodicities. However, whereas the electron-side of the d*I*/d*V* traces (positive sample bias, tunneling to unoccupied sample states) shows apparently little variation, the hole-side acquires a systematically higher spectral weight and develops a clear resonant structure near E_D as one progresses from the 5*a* (Fig. 5.3e) to the 2*a* arrays (Fig. 5.3h). This reconstruction of the LDOS decays rapidly with the distance to the array and is no longer noticeable beyond 10-15 nm. The local spectral traces near a 5*a* array are close to those of an isolated F_4TCNQ, which is consistent with an effective screening length of the Coulomb field arising from each molecule of $\lambda_S \sim 10$ nm

that we estimate for these graphene devices. On the contrary, in the densest 2*a* array (Fig. 5.3h), the resonance is prominently developed which strongly suggests the presence of localized states in those regions of graphene, and that these emerge as a result of increasing the linear charge density. Moving the tip vertically at a constant perpendicular distance to the array does not visibly change the shape of the traces (not shown), so that the effect depends only on the distance to the array, and not on whether a trace is taken right in front of a given molecule or elsewhere along a vertical line. These features cannot be attributed to molecular states: on the one hand, we are probing the tunneling conductance *on* graphene; on the other, the molecular states are much more tightly bound to the molecule and their spectral fingerprint in d*I*/d*V* is seen to vanish at distances beyond 1.25 nm from the F_4TCNQ center.

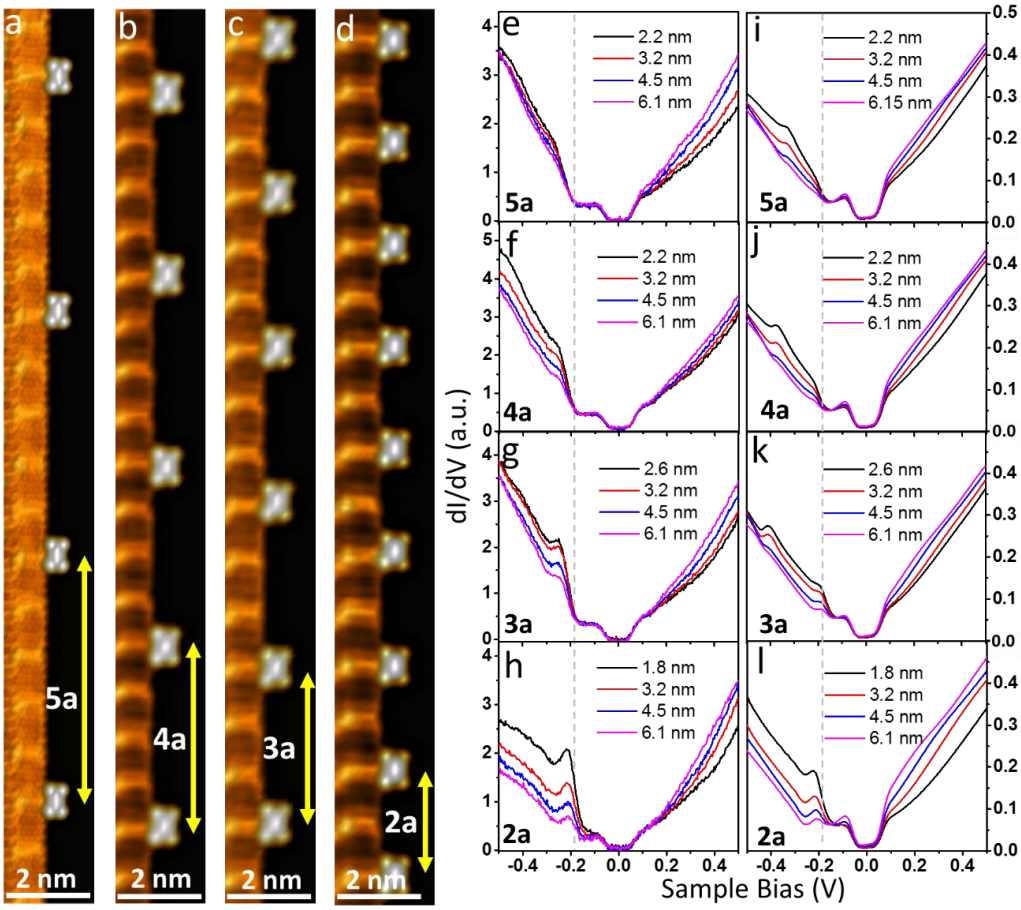

Figure 5.3 1D molecular charge arrays evolve from subcritical to supercritical regime. **(a-d)** STM images of 1D molecular array with tunable packing density: from 5a to 2a **(e-f)** *dI/dV* spectra measured at different distance away from the center of F_4TCNQ molecule in individual charged arrays. All the spectra were taken at the same back-gate voltage (Vg=30V). **(i-l)** theoretical calculated *dI/dV* spectra for graphene at the same distance from molecular charge arrays as in **(e)** to **(f)**. Q = 0.5 and kappa = 0.014 (screen length 7nm)

5.4 Induced quasi-bound supercritical states in graphene

We first investigated whether the experimental restructuring of the LDOS in the near-field can indeed be ascribed to the Coulomb potential created by the charge at each molecule, and its influence in graphene's electronic distribution. Towards that, we calculated the LDOS theoretically expected for a graphene sheet containing an array of point charges located at the centers of each molecule. We verified that there is no difference in the results between assuming point charges at the geometrical centers of each molecule or a uniform distribution extended over the area of each molecule (which is not surprising given that the distances where the LDOS is probed are larger than the size of the molecules, whence only the monopole contribution of the molecular charge density is relevant). The electrons in graphene were modeled within the well established single-orbital, nearest-neighbor tight-binding approximation in the honeycomb lattice. As there is an explicitly finite electron density under the conditions of Fig. 5.3, the Coulomb potential arising from each (molecular) point charge should be screened. We therefore consider the potential $V(r) = Ze^2F(r)/\kappa_e\kappa_g r$, where Z is the effective valence of one charged F4-TCNQ, κ_e is the dielectric constant contributed by the air/BN environment, κ_g the short-range part of graphene's dielectric constant [$\kappa_g \equiv \varepsilon(q\to\infty, \omega = 0)$], and $F(r)$ represents the screening function. In order to correctly capture the fact that in graphene the Coulomb potential remains unscreened at short distances and decays asymptotically as $\sim 1/r^3$ [136-139], we interpolate the real space screening function by the simpler dependence $F(r) = [1+(r/\lambda_s)^2]^{-1}$ (see supplementary information for details). The plots shown represent the best agreement with the experimental traces that was obtained using an effective valence per molecule of Z =0.86 (with $\kappa_g \simeq 2.6$ as given by the RPA at the interface between air and BN), and $\lambda_S = 10$ nm (supplementary information). Taking into account that our calculation is at the single-particle level without self-consistency in the potential or LDOS, this value obtained for Z is in good agreement with the expectation of a nominal unit of charge per F_4TCNQ at V_g = 30 V (as discussed earlier); the estimated screening length agrees well with the fact that, in the arrays of period "5a" ($\simeq 10$ nm) and higher, the dI/dV traces approximate those of an isolated molecule, implying that the Coulomb field from neighboring molecules is sharply reduced beyond these distances. Note also that, in the BN substrate, we estimate that a single Coulomb charge remains undercritical for $Z < 1.3$, tallying with our spectral observations in the vicinity of isolated F_4TCNQ molecules.

This analysis reveals that the densest arrays cause the appearance of what seem to be localized states in nearby graphene. This is surprising at first sight because the gapless nature of graphene's electronic spectrum precludes the existence of bound states. However, it has been predicted theoretically[6, 23] — and demonstrated experimentally[7] — that, since electrons in graphene behave effectively as massless relativistic particles with a much larger associated fine structure constant, Coulomb impurities can easily reach the so-called supercritical regime. One visible consequence of this regime is the marked spectrum reconstruction with the appearance of a series of quasi-bound states near the Dirac point. This effect is the graphene analogue of the famous problem of supercritical nuclei in quantum electrodynamics which predicts the collapse of bound electronic levels in the solutions of the relativistic wave equation for the hydrogen atom beyond a threshold value of the nuclear charge[19-21, 140, 141]. One peculiar aspect of these

states that arises from the Dirac nature of the electrons is that, despite their resonant nature, they are tightly localized in space, within a few lattice spacings, even in the absence of a band gap. It is therefore enticing to interpret the progressive modifications in d*I*/d*V* with decreasing array period as the crossing-over to the supercritical regime.

We have further assessed the degree of localization of these states within the same tight-binding model described above by exactly diagonalizing the single particle Hamiltonian, thereby having direct access to the electronic wavefunctions. As they imply a full diagonalization of the Hamiltonian, these calculations are restricted to smaller system sizes in comparison with those used to determine the LDOS, but large enough to still allow an unambiguous analysis of the array of period "2*a*". Quasi-localized states are seen to appear at energies in the vicinity of the Dirac point corresponding to the resonances in the LDOS traces. An example of one such state is shown in Fig. 4a, where the black dots mark the positions of the Coulomb charges and the colored dots represent the probability density at each lattice site (the local magnitude is reflected in both the size of the dot and its color). Unlike states at different arbitrary energies that are extended, the wavefunctions associated with these are visibly confined within a few lattice spacings, 1-2 nm to each side of the charged array. Significantly, its probability density is not strongly modulated along the vertical direction, which concurs with the observation that both our experimental and theoretical LDOS does not vary significantly along a vertical scan (not shown). We designate these states as "quasi-localized" to underline the fact that, despite being resonances and not true bound states, their wavefunctions are still rather tightly confined near the array.

5.5 Charging and discharging of the supercritical states

There is additional experimental evidence in favor of this picture of quasi-localized states being responsible for the resonances seen in d*I*/*dV* near the Dirac point. If the resonant peaks at energy E_R are to reflect quasi-bound states of graphene, they should track any changes in the position of graphene's Dirac point (E_D) as the latter is varied with the back gate. At the reference gate voltage $V_G = 30$ V, graphene is electron-doped and both its Dirac point and resonances lie at negative sample biases (Fig. 5.4). Decreasing V_G removes electrons and should cause these features to appear at progressively higher V_S in the d*I*/d*V* plots. Fig. 5.4a shows indeed such progression when $30 > V_G > 10$ V for the group of peaks labeled A. However, at around $V_G = 20$ V there is an evident discontinuity in this evolution: not only does the resonance seem to disappear, but a new, much sharper peak (labeled ***B*** in the figure) emerges at high bias (more negative), and with the opposite progression as V_G is reduced further. The disappearance of the resonance is natural in this experiment since at $V_G \approx 20$ V the resonance (and E_D) merges with the onset of the inelastic gap at $V_S \approx -65$ meV. Logically, these should re-emerge at positive V_S when the the Dirac point is raised above E_F, and they do, as documented by the onset of the broad peaks (labeled ***A***') near $V_S \gtrsim +65$ meV that are clearly visible for all the traces with $V_G < 17$ V. The features ***A*** and ***A'*** are thus simply tracking the position of the resonance at different V_G, and they differ only in that ***A*** refers to occupied and ***A***' to empty electronic states.

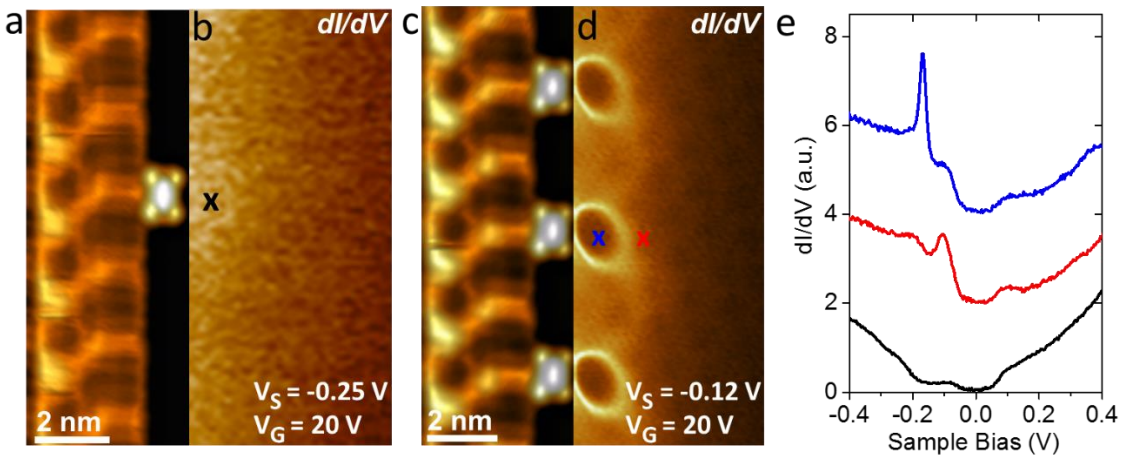

Figure 5.4: Spatial dependence of 1D supercritical states. (a) STM imaging of an isolated molecule in a diluted 4a charge array. (b) dI/dV mapping (VG = 20V and VS = -0.25 V) of nearby graphene regions. (c) STM imaging of 2a charge array (d) the corresponding dI/dV mapping (VG = 20V and VS = -0.12 V) of nearby graphene regions shows a series of charge rings (e) Gate-dependent spectra acquired at a lateral distance of 1.7 nm from the center of a charged F4-TCNQ molecule inside 2a array

The peaks ***B***, on the other hand, are peculiar and more revealing. Their opposite evolution with V_G signals charging and discharging events taking place under the influence of the tip, and are analogous to effects observed in STM measurements near isolated donors or acceptors present in the target system[127, 128, 142]. The unprecedented aspect here is that graphene, its BN substrate, and the interface are atomically clean, as is evident from our spectroscopic and topographic maps. Consequently, the charging events must be related to the local electronic structure of graphene itself, which is consistent with the existence of the quasi-localized states near the charged array. This is supported by our observation of the hallmark rings in the spatial maps of differential tunneling conductance shown in Fig. 5.3e, which are analogous to those well documented in systems with isolated impurities or adsorbates. These rings are clearly and reproducibly centered at positions considerably far from the F_4TCNQ for them to reflect charging events related to the molecules which remain stably charged in this range of V_G (supplementary information). Instead, they are direct evidence of the charging and discharging of the quasi-localized states whose wavefunctions have finite probability density in these regions as per the results of the model calculation shown in Fig. 5.5.

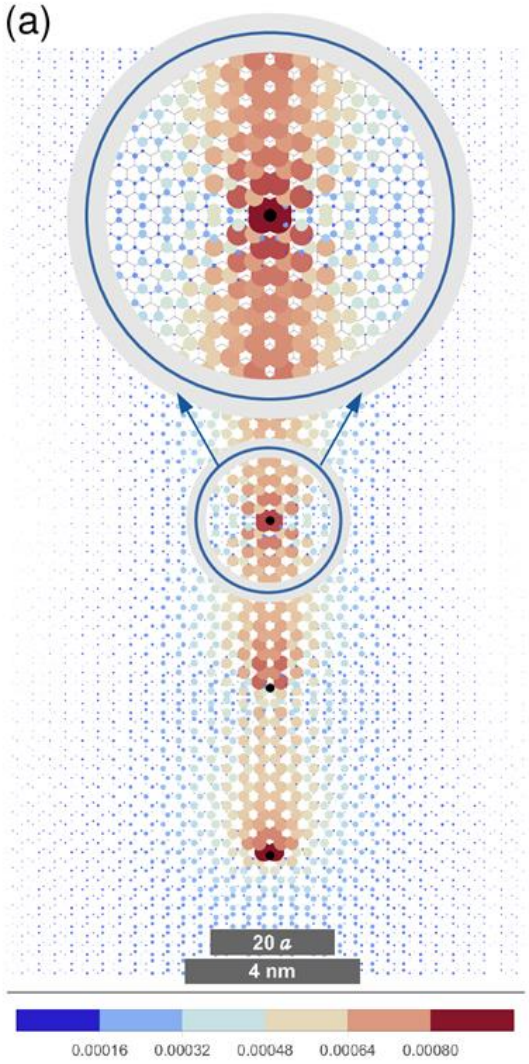

Figure 5.5: Theoretical modeling of supercritical state wave function and explanation of charging ring. Density plot of the wavefunction associated with a supercritical resonant state in graphene ($E_R \simeq 8$ meV above the Dirac point) obtained from exact diagonalization of the electronic Hamiltonian discussed in the main text. Black dots mark the positions of the 5 Coulomb centers used in the calculation and the colored disks reflect the state's local probability density both through their size and the color scale shown in the bottom. The charges are separated by 3.8 nm, as in the experimental array of period "2*a*", and the system has 16,000 carbon atoms spanning about 19×21 nm^2 (on account of the horizontal decay we clipped out the outer horizontal domain to improve the visibility of the central region). In the upper part we show a close-up of the circular region outlined around the central charge, where the rapid decay is visible against the underlying honeycomb lattice.

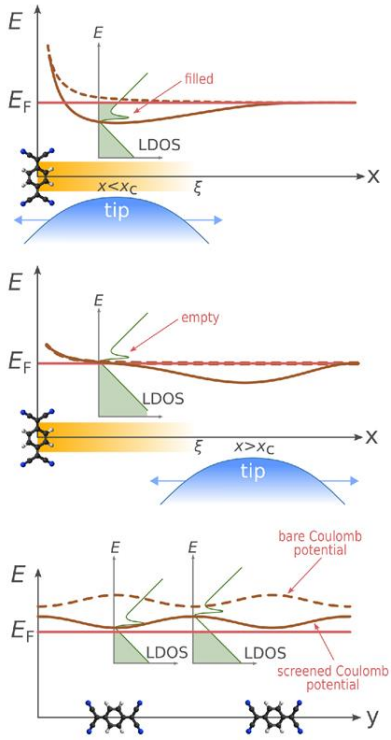

Figure 5.6: Interpretation of supercritical charging ring. (b,c) Schematic position dependent energy diagrams to illustrate the band bending arising from the interplay between tip and the nearby negatively charged F4-TCNQ molecules. The horizontal axis represents distance from the molecule for displacements perpendicular to the molecular array. The horizontal red line marks the Fermi level of graphene, the brown-dashed line indicates the band bending induced by the molecule when the resonance is unfilled and the tip is absent, and the solid brown line illustrates the combined effect of the latter with the local down-bending created by the tip when positively biased with respect to the sample ($V_S < 0$). The fading orange strip overlapping the horizontal axis represents the decay of the supercritical states away from the molecule positions. (d) Simplified illustration of the local electrostatic potential along a direction parallel to the charged array when the leading supercritical resonance is empty. While the bare potential (dashed) is stronger right in front of each molecule, the emptying of the hole-like resonance promotes screening of the negative molecular charges. Since from (a) these states have higher probability amplitude near the charges, the effect is likely to be stronger there leading, through self-consistency, to a screened potential as depicted by the solid line and the corresponding local band-bending illustrated by the LDOS diagrams. When the STM tip approaches under negative sample bias, the additional band bending it induces (not represented in this figure) can lead to the charging of the supercritical states;.this will occur first at the places right in front of the molecules, since the resonant level is closer to E_F there. Panels (b-d) combined explain the appearance of the chargin rings shown in Fig. 3(d) and the pinning of their centers at a finite distance right beside each molecule.

The charging rings observed in Fig. 5.4b are due to a corresponding threshold behavior as a function of the distance between the tip and the localized state under constant bias. We note, first, that the rings observed here are unusual in that they are centered at locations where there is no significant feature in graphene; this is in contrast with the common observation of charging rings centered at impurity positions. We attribute it to an interplay between the electrostatic potential of each molecule and of the tip, schematically illustrated in Figs. 5.6a,b. When the tip lies directly above the center of a charging ring, the resonant states will be occupied as long as $V_S < V_C$. This is illustrated in the energy-vs-position diagram of Fig. 5.6a, where the solid brown line represents the local placement of E_D and its variation as a function of distance from the molecule. When the resonant state is filled, as drawn, the molecular charge is less efficiently screened (see the discussion in the next section). As this charge is negative, it causes an upward band bending at the shortest distances to a molecule (for reference, the dashed line represents such band bending due solely to the unscreened molecular charge, when the tip is not present). Since the potential of the tip is higher than that of graphene, it promotes the down-bending of the local electronic spectrum in the regions directly underneath. This counters the up-bending from the molecules and creates the spatial profile qualitatively illustrated by the solid line. If the tip is displaced at constant V_S closer to the molecule, where the up-bending dominates, the resonant level rises above E_F and becomes empty. This discharging event corresponds to the edge of the ring closer to the molecule. When the tip is moved in the opposite direction, away from the molecule, its compensating down-bending effect that keeps the state filled is progressively reduced until, at a threshold distance x_C, the level crosses E_F again and becomes empty (Fig. 5.6c). This causes the outer edge of the charging ring to appear at x_C. Whereas this picture is consistent with the existence of two threshold distances for charging and discharging whenever the tip is moved from afar towards one molecule, it does not account for the fact that these threshold distances close into a ring pinned to the outside of each molecule. It is very likely that the self-consistent screening of the molecular charge that is in effect when the supercritical resonance is empty pulls more positive induced charge in graphene right in front of each molecule because that's where the bare Coulomb potential is the strongest. The result of this would be more up-bending of the spectrum in any vertical direction away from the line that intersects the molecule perpendicularly to the array; this is consistent with the closure of the threshold charging distance into a ring pinned to the outside of every molecule, as seen in Fig. 5.4b.

5.6 Frustrated supercritical collapse

Our STM measurements address the fundamental question of whether an array of undercritical charges placed on top of graphene and separated by more than 30 lattice constants can become supercritical, and what conditions are necessary for that regime to be established. Without loss of generality, this question can be analyzed from the simpler perspective of one pair of equal charges separated by a distance d, which is easier to visualize. Consider the ideal case of undoped graphene in vacuum and ignore the RPA corrections to the dielectric, which assumptions don't impact the validity of the following arguments. If each charge has nominal valence Z, it becomes supercritical when $Z\alpha_0 > 1/2$, where $\alpha_0 \equiv e^2/\hbar v_F$ is the effective fine

structure constant in graphene and $v_F \equiv 3ta/2$ the Fermi velocity ($a \equiv 0.142$ nm is the inter-carbon distance)[6, 23, 139]. We now suppose that $Z < Z_C \equiv 1/2\alpha_0$ so that each of the charges in the pair is undercritical. In undoped graphene, the absence of screening means that the potential created by each charge remains of the Coulomb form all the way to infinity. Hence, when observed from large distances ($r \gg d$), the potential is well approximated by the dominant multipole term which, since the charges are equal, is the monopole term. As a result, the potential seen there is that of a point Coulomb charge with effective total valence $Z_{\text{eff}} = 2Z$, which is an obvious expectation. Consequently, in the far-field, the pair of charges will look as supercritical when $Z_{\text{eff}} > Z_C$, or $Z > Z_C/2$ (obviously, for N identical charges the supercritical threshold in the far-field occurs when $Z > Z_C/N$). This defines the far-field of the charge pair.

In the semi-classical picture of the carrier motion in graphene under such (repulsive) potential, the supercritical regime is characterized by the existence of a radial potential barrier that allows electrons at its far end to tunnel into hole states on the charge side of the barrier; this barrier is absent for undercritical couplings[6, 143]. For a single supercritical impurity, these holes describe elliptical collapsing orbits that fall singularly towards the center of the potential[6, 144]. In the full quantum mechanical solution, the necessary (and physically correct) regularization of the potential's short distance divergence stabilizes an infinite number of quasi-bound states localized on the scale of the potential regularization, r_0 [6, 23, 54, 139, 145]. The effect of these quasi-bound states, or their counterpart collapsing orbits in the classical picture, is the screening at very short distances of the potential so that the system heals itself of the singularity caused by the overly strong potential by bringing the charge self-consistently down to the supercritical threshold[6, 139, 141, 145]. In other words, the emergence of the supercritical states permits the self-consistent screening of the Coulomb charge so that, in the end, it never exceeds Z_C at distances beyond the supercritical screening cloud (itself of the order of r_0).

We now return to the pair of charges and reason semi-classically assuming that $Z_C/2 < Z < Z_C$, and that both sides of the supercritical potential barrier reside in the far-field. Spontaneous electron-hole pairs are created again and the hole begins its collapsing trajectory towards the potential center. However, when it reaches the near field, the potential is nowhere supercritical and, as a result, no collapsing orbit exists (e.g., if the orbit brings the hole towards one of the charges, it cannot collapse in any way because $Z < Z_C$, by assumption). In this sense, the collapse into the center of the potential has been frustrated by the regular behavior of the potential in the near field. The full quantum version does not have an exact solution, unlike the case of a single charge. However, it is amenable to analytic approximations on the basis of which Sobol et al. suggest that the supercritical regime of a pair of charges in ideal graphene obtains for $Z > Z_C/2$.[144] This might appear contradictory with the semi-classical picture, and also with the fact that asymptotically near each charge the potential is always undercritical. This begs the clarification of the precise meaning of the supercritical regime in a system of individually undercritical charges separated by finite distances.

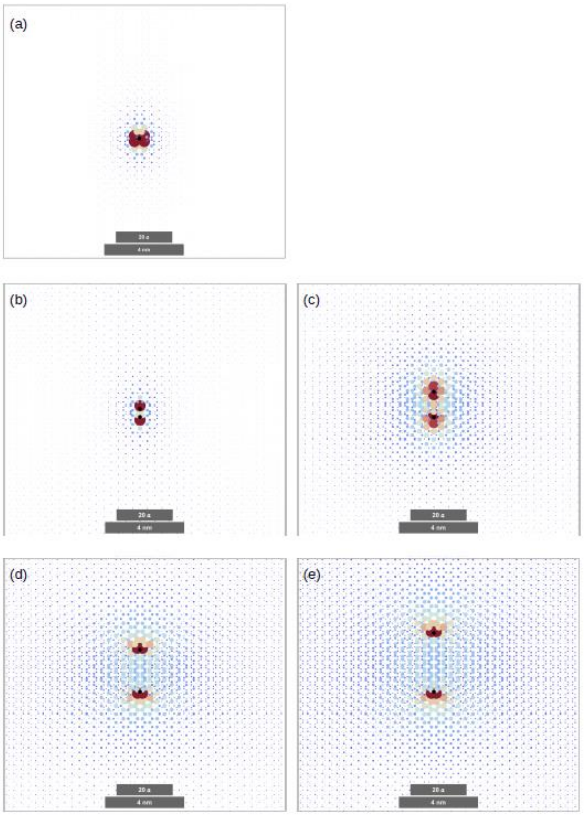

Figure 5.7: Eigenfunction of the most bound supercritical state of a pair of charges as a function of charge separation. (unscreened potential, Q = 0:6, only the central region of our 160 X 100 atom system is shown for clarity). Black dots mark the positions of the point charges, and the size of the colored disks is proportional the local probability density. (a) d = 0 nm (E = 0.067t), (b) d = 3a ≈0.4 nm (E = 0.054t), (c) d = 9a≈1.3 nm (E = 0.015t), (d) d = 15a≈ 2.1 nm (E = 0.013t), (e) d = 21a≈ 3.0 nm (E = 0.011t). Notice how the spatial extent of the wavefunction is similar in (a) and (b) but increasing the charge separation d makes the wavefunction spread over increasingly large areas, with a characteristic linear dimension that is roughly of the same order of d.

A simple scale invariance argument allows one to vividly illustrate this. As the Dirac wave equation that governs electrons at the relevant energies in graphene involves only the first derivative with respect to the space coordinates, the kinetic and potential terms in the Hamiltonian have the same scaling. One consequence is that the coupling parameter to the Coulomb field, $Z\alpha_0$, remains unchanged under any scale transformation $r \rightarrow \Lambda r$. For an array of N charges separated by d, this entails that $d \rightarrow d/\Lambda$, under such scale transformation. Hence, if $\Lambda \gg 1$ so that $d/\Lambda \sim a$, the total potential at any distance will be the one of a point charge with effective valence $Z_{\text{eff}} = N Z$, and one expects the supercritical threshold to occur when $Z > Z_C / N$ (this tallies, of course, with our discussion above of the effective potential seen in the far-field). Therefore, an array with a large number ($N \gg 1$) of charges shall be supercritical for an arbitrarily small value of the nominal valence of each, Z. There is, however, an important detail.

We know that, for a single charge, the most tightly bound supercritical state is localized within a distance of the order of $\sim a$ from the center [7,24]. The scale invariance then dictates that the corresponding supercritical state in an array shall be localized at $\Lambda a \sim (d / a)\, a = d$: the most bound state therefore resides at a typical distance from the array that is of the same order as the inter-charge separation (in other words, the dominant supercritical states are always spread within the characteristic regularization distance of the potential). We have verified that this indeed holds by direct inspection of the exact numerical wavefunction of the dominant supercritical state as a function of charge separation. It is also consistent with the spread of the state shown in Fig. 4(a), which is mostly concentrated within a horizontal distance similar to the charge separation, and conforms with the fact that, in our experiments, charging rings appear always confined within those same distances from the array.

A crucial detail for the observability of these supercritical states in real samples is, of course, the degree to which electrons screen the Coulomb field, in particular, the magnitude of the screening length, λ_S. Obviously, the supercritical regime of the array should disappear whenever $\lambda_S \ll d$ since, then, the combined potential of any pair of different charges can never be of the Coulomb form. In addition, according to the argument above, the tightest supercritical states are pushed out so that they spread to distances that are also $\sim d$ away from the array. In order for these states to remain in the presence of screening, one must have at least $\lambda_S \gtrsim d$ to ensure they still constitute a solution of the wave equation in all the regions $r \lesssim \lambda_S$. Furthermore, in contrast to the unscreened case where there is a formally large number of resonant supercritical states "localized" within increasingly outer regions of space, a finite λ_S necessarily implies a finite number of such states since they cannot be supported when their natural localization radius is larger than the screening distance. The suppression of the supercritical regime with increasing screening is also verified explicitly from the exact spectrum and wavefunctions studied under in different values of d, Z and λ_S. In our measurements, this physics is borne out by the fact that the resonant supercritical signature in the dI/dV curves of Figs. 5.3e-h is seen to fade away for $d \sim 10$ nm (the "5a" arrays), despite the fact that, under ideal and undoped conditions, our array with $N \gg 1$ would be expected to remain supercritical.

6 Two-dimensional self-assembled molecular islands on graphene

Strong electron acceptor molecules like F_4TCNQ allow non-covalent functionalization of graphene and the generation of charge patterns without altering the structure and electronic properties of graphene. In comparison to lithography-based patterns, the charge pattern induced by molecular dopants is atomically sharp and uniform. The large charge density induced by the molecular islands creates a sharp P-N junction on graphene, which can be used to implement graphene electron optics [8].

This chapter presents our investigations into two-dimensional self-assembled molecular islands and graphene P-N junctions. As we deposit F_4TCNQ onto a graphene/BN surface, the charged F_4TCNQ molecules are observed to self-assemble into a tightly bounded planar molecular island. Here we explain the mechanism of molecular self-assembly due to work function heterogeneity and support it by *ab initio* calculation. The content here is based on our published paper: H.-Z. Tsai et al., "Molecular Self-Assembly in a Poorly Screened Environment: F4TCNQ on Graphene/BN", *ACS Nano* 9, 12168 (2015).

6.1 Introduction

Surface functionalization via molecular self-assembly is a potentially useful technique for tuning the properties of graphene layers.[146-148] Previous studies have shown that functionalization via tetrafluoro-tetracyanoquinodimethane (F_4TCNQ) adsorbates is particularly effective at p-doping graphene through the transfer of electrons from graphene to the adsorbed molecules.[61, 64, 71, 149] These studies, however, were performed using spatially averaging techniques and so were not able to determine local molecular self-assembly characteristics. Locally resolved scanning tunneling microscopy (STM) measurements of F_4TCNQ molecules deposited onto graphene/Ru(0001) also indicate charge transfer of electrons from graphene to F_4TCNQ and provide some structural information.[116] These measurements reveal that F_4TCNQ molecules on graphene/metal do not assemble into islands, but rather repel each other due to interaction between electronegative constituents (e.g., F and CN).[116, 117] The graphene used in these STM measurements, however, was supported by a bulk metal and so created a highly screened environment where long-range Coulomb interactions were damped. The local behavior of charged molecules on a poorly screened graphene surface that supports long-range Coulomb interactions has not been explored.

Here we report a combined STM, non-contact atomic force microscopy (nc-AFM), and theoretical investigation into the self-assembly characteristics of F_4TCNQ molecules on a graphene substrate supported by insulating hexagonal boron nitride (BN). This provides a nearly ideal setting to study molecular self-assembly on isolated graphene in a poorly screened environment since BN is a wide-bandgap insulator that interacts with graphene only weakly.[13,

14, 39, 40] We observe that, unlike previous measurements of F_4TCNQ on graphene supported by metals, F_4TCNQ molecules on graphene/BN assemble into tightly packed 2D islands. This unexpected result can be explained by a unique self-assembly mechanism that is based on heterogeneous lateral charge transfer driven by local work function differences.

6.2 Results and discussions

F_4TCNQ molecules (figure 6.1a) were deposited onto graphene/BN in ultrahigh vacuum (UHV) using a Knudsen cell evaporator. Molecular deposition was performed while electrically grounding the graphene layer at room temperature. The sample was then cooled to 4.5 K and imaged with both STM and nc-AFM using a CO-molecule functionalized tip. The nc-AFM, which detects the frequency shift of a qPlus resonator in constant height mode, allows high-resolution imaging of individual chemical bonds and atomic-scale structure.[33, 150]

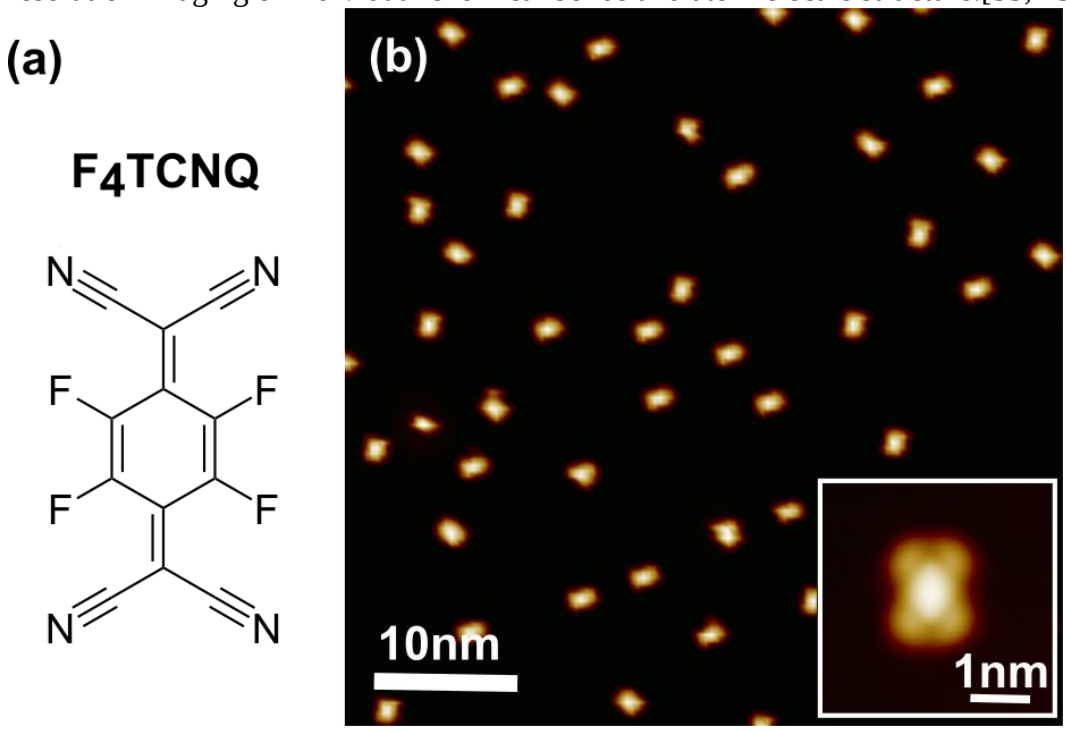

Figure 6.1: Schematics and topography of the F_4TCNQ molecule. (a) Chemical structure of F_4TCNQ molecule. (b) STM topography of F_4TCNQ molecules deposited onto graphene/BN at low coverage (below 0.1 monolayer). Inset shows close-up view of a single F_4TCNQ molecule. STM tunneling parameters are $V_s = 2$ V, $I_t = 5$ pA, T = 4.5 K.

At low molecular coverage (below 0.1 monolayer (ML)), the majority of molecules deposited on graphene are isolated and typically separated from each other by more than 4 nm, as shown in the STM topographic image in figure 6.1b. This observation is consistent with earlier studies of F_4TCNQ deposited onto graphene/metal.[116, 117] However, at higher coverage (above 0.2 ML), we observe that molecular adsorbates can coalesce into close-packed islands (figure 6.2a). High-resolution nc-AFM imaging (figure 6.2b) shows that F_4TCNQ

molecules within such islands are oriented in a planar rectangular geometry parallel to the underlying graphene (the molecular island unit cell is 1.25 ± 0.03 nm x 0.78 ± 0.03 nm). Molecular packing in the island is about 50 times denser than when the molecules are isolated at 0.1 ML coverage. Faint lines observed between adjacent molecules are likely caused by tilting of the CO molecule at the tip apex, as described in previous work.[124, 125]

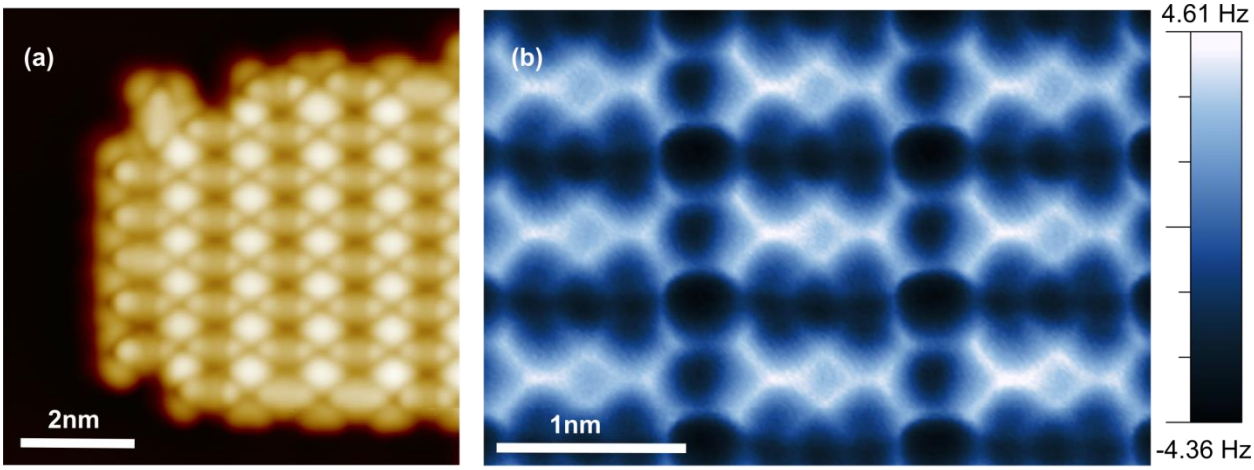

Figure 6.2: Structure of the 2D molecular island. (a) STM and (b) nc-AFM images of an F_4TCNQ 2D island on graphene/BN. The nc-AFM image resolves individual chemical bonds within the F_4TCNQ molecules and shows that molecules within the island lie flat on the surface in a close-packed rectangular lattice. Measurement parameters are f_0 = 28.7 kHz, amplitude = 60 pm, Q = 10^5, T = 4.5 K.

We now discuss the mechanism for F_4TCNQ island assembly in 2D. We first used density functional theory (DFT) to confirm the known 3D crystal structure of bulk F_4TCNQ. Our calculation agrees well with the crystal structure determined previously using X-ray diffraction[151, 152], and reveals a large binding energy between molecular units in the 3D bulk crystal (1.6 eV per molecule, as shown in figure 6.3a). A natural assumption would be that the same attraction mechanism that works for the bulk (driven by electrostatic and van der Waals interactions) is responsible for the formation of self-assembled 2D islands. To test this assumption we used DFT to calculate the total energy of F_4TCNQ molecules in the absence of a substrate constrained to the same 2D planar geometry that we observed in our nc-AFM images (figure 6.2b). Surprisingly, we found that the calculated interaction between molecules under these conditions is repulsive rather than cohesive. This can be seen in figure 6.3b, which shows the total energy per molecule of a 2D island as a function of intermolecular distance. This curve exhibits a negative energy-vs-distance slope, thus implying that 2D island formation is energetically unfavorable for F_4TCNQ under these conditions.

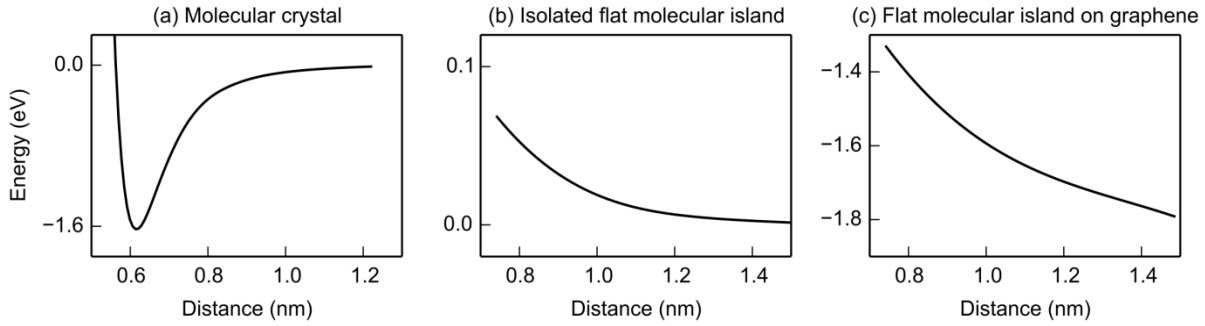

Figure 6.3: Calculated total energy per F4TCNQ molecule as a function of the shortest distance between molecules for (a) a bulk molecular crystal, (b) an isolated, flat 2D molecular island having the same structure as in figure 2b, and (c) same as (b) but with a graphene substrate.

This result indicates that the graphene substrate must play an important role in 2D island formation for F_4TCNQ molecules. In order to understand the effect of the graphene substrate, we performed an ab initio DFT calculation of the total energy of a 2D F_4TCNQ island supported by a single layer of graphene (i.e., homogeneous molecular coverage in a periodic array). Inclusion of graphene in the simulation results in partial electron transfer from the graphene to the F_4TCNQ molecules. Each molecule in an island thus forms an electric dipole with the electron-depleted patch of graphene directly underneath the molecule (the dipole points down into the plane). The resulting dipole-dipole interactions between neighboring molecule-graphene complexes are repulsive and island formation becomes even less favorable than without graphene, as seen in the calculated energy-vs-distance curve of figure 6.3c. Despite this repulsion, electron transfer from graphene into the molecules results in very strong binding of the molecules to the graphene (more than 1.8 eV per molecule, as shown in figure 6.3c).

The calculations discussed so far were performed under fixed-electron-number conditions, a common constraint for DFT calculations. However, in a real molecular island surrounded by pristine graphene, the total number of electrons per molecule is not necessarily constant since island formation creates work function heterogeneity and leads to lateral transfer of screening charge (i.e., electrons flow from low work function areas to regions having higher work function[153-155]). As a result, the real experimental system is better described within a fixed-electrochemical-potential picture. Here the electrically grounded graphene sheet surrounding the island acts as an electron reservoir at fixed electrochemical potential.

While ab initio techniques cannot directly treat this case of a large island surrounded by pristine graphene (as pictured in figure 6.2a), they can be used to treat homogeneous systems having different overall electron density and work functions. We can thus model the real heterogeneous (i.e., not periodic) system by comparing different homogeneous (i.e., periodic) systems with varying work functions. We applied this technique by simulating homogeneous systems where graphene was subjected to different molecular coverages and where the overall charge carrier density was varied by hand (each individual calculation had a fixed number of

electrons). This provides a method for taking into account the fact that (since F_4TCNQ molecules p-dope graphene) the local work function increases as islands assemble, thus causing electrons to flow into an island as molecules are packed more densely (in order to keep the electrochemical potential constant).

To illustrate this technique we performed two separate DFT calculations of the work function above F_4TCNQ molecules on graphene as a function of intermolecular separation (shown in figure 6.4a), each with a different number of charge carriers. In the first calculation (black curve) each molecule-graphene complex is charge neutral. In the second calculation (red curve) each complex has an excess of electrons that are allowed to redistribute within the entire molecule-graphene assembly until reaching the ground state (one extra electron per each 36 carbon atoms in graphene, roughly one extra electron per molecule at full coverage). Here the vacuum energy above the island is set to zero and so the work function is equivalent to the negative of the electrochemical potential. As expected, the work function above an island strongly increases for both the neutral and charged cases as the molecules are brought closer to each other (a similar dependence has been found earlier and was assigned to depolarization effects[156, 157]). The work function in the charged case is overall lower compared to neutral case, reflecting the increase in electrochemical potential that occurs as carrier density of the molecule-graphene complex is increased.

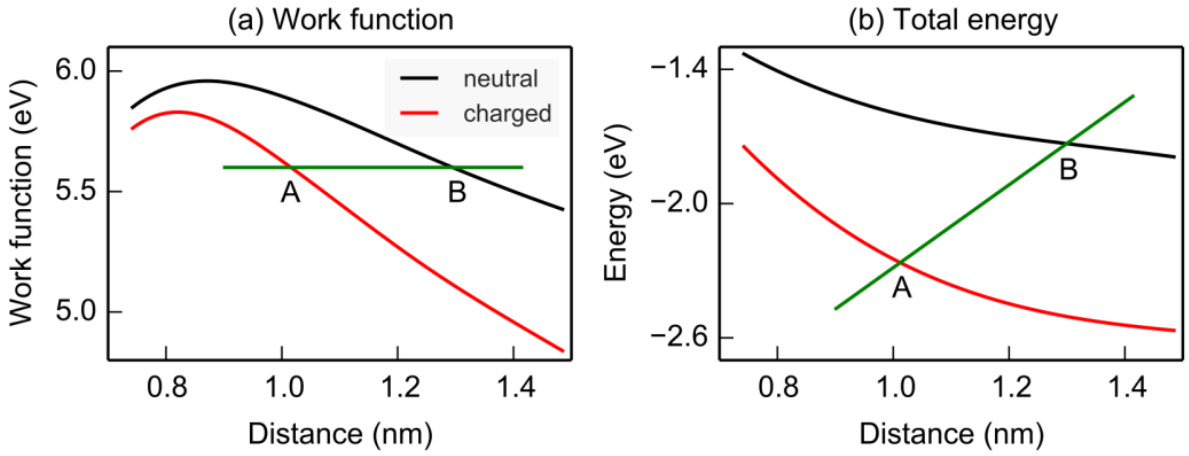

Figure 6.4: Calculated work function and total energy as a function of distance between molecules (a) Calculated work function relative to the vacuum level above an F_4TCNQ molecular assembly on graphene as a function of the shortest distance between molecules for both the neutral case (black line) and the electron-doped case (red line). (b) Calculated total energy per F_4TCNQ molecule on graphene as a function of the shortest distance between molecules for both the neutral case (black line) and the electron-doped case (red line). Green line shows hypothetical constant electrochemical potential (see text).

Figure 6.4b shows the calculated total energy of the F_4TCNQ molecules versus molecule-molecule separation for the same neutral and doped systems. The neutral case is identical to what is shown in figure 6.3c and results in overall binding of the molecules to graphene (negative

energy) but an increasing energy with increased molecular density. For the doped case we see similar behavior, except that there is a net decrease in the total energy, reflecting the increased binding energy of the molecule-graphene complex as electrons are added to the system.

The origin of the attractive force driving island assembly of charged molecules on isolated graphene can be deduced from the curves shown in figure 6.4. To see this it is useful to imagine F_4TCNQ molecules on a graphene surface with a particular fixed hypothetical electrochemical potential, as indicated by the green line (the island formation mechanism is not sensitive to the precise value of the electrochemical potential). To achieve this particular electrochemical potential at a large intermolecular distance as indicated by point B in figure 6.4a, the island has to be charge neutral since the green line crosses the neutral-island configuration (black line) at B. However, at a shorter intermolecular distance (point A) the island has to absorb excess electrons from the reservoir and becomes charged (red line) in order to achieve the same electrochemical potential as at B (as required by thermodynamic equilibrium). Since the total energy of a molecule-graphene complex is lower at the corresponding charge state and distance of A than at B (figure 6.4b), we conclude that within a fixed electrochemical potential picture it is energetically favorable for the molecules to be closer to each other and to form a stable island (this can also be seen from the positive energy-vs.-distance slope of the line connecting point A to point B in figure 6.4b).

The island cohesion mechanism demonstrated in figure 6.4 for fixed electrochemical potential can intuitively be understood as follows: as negatively charged molecules coalesce into an island there is an increase in the local work function above the island (figure 6.4a) that causes additional electrons to flow into the island. These additional electrons cause the total energy of the molecule-graphene complexes to decrease (figure 6.4b), resulting in island cohesion. This mechanism is not applicable to adsorbates on highly metallic substrates because of the high density of states in these substrates compared to graphene. In these systems electric fields induced by charge transfer are screened, and charge transfer induced by work function differences does not lead to reduced total energy. This explains why close-packed island formation has not been seen for F_4TCNQ molecules adsorbed onto graphene/Ru(0001).[116]

In conclusion, we find that F_4TCNQ molecules aggregate into close-packed islands on graphene/insulator, unlike their behavior on graphene/metal. This behavior is explained by a new type of island formation mechanism driven by lateral charge screening induced by long-range Coulomb interactions. We expect this island formation mechanism to apply to other molecular adsorbate systems that exhibit charge transfer in poorly screened environments. For such systems the work function above deposited molecules will strongly vary with intermolecular distance, causing additional charge transfer and increased binding as island density increases.

Bibliography

1. Hwang, E.H. and S. Das Sarma, *Acoustic phonon scattering limited carrier mobility in two-dimensional extrinsic graphene.* Physical Review B, 2008. **77**(11): p. 115449.
2. Dean, C.R., et al., *Boron nitride substrates for high-quality graphene electronics.* 2010. **5**: p. 722.
3. Bolotin, K.I., et al., *Ultrahigh electron mobility in suspended graphene.* Solid State Communications, 2008. **146**(9): p. 351-355.
4. Han, W., et al., *Graphene spintronics.* Nature Nanotechnology, 2014. **9**: p. 794.
5. Zomer, P.J., et al., *Long-distance spin transport in high-mobility graphene on hexagonal boron nitride.* Physical Review B, 2012. **86**(16): p. 161416.
6. Shytov, A.V., M.I. Katsnelson, and L.S. Levitov, *Atomic Collapse and Quasi-Rydberg States in Graphene.* Physical Review Letters, 2007. **99**(24): p. 246802.
7. Wang, Y., et al., *Observing Atomic Collapse Resonances in Artificial Nuclei on Graphene.* Science, 2013. **340**(6133): p. 734-737.
8. Chen, S., et al., *Electron optics with p-n junctions in ballistic graphene.* Science, 2016. **353**(6307): p. 1522-1525.
9. Mao, H.Y., et al., *Manipulating the electronic and chemical properties of graphene via molecular functionalization.* Progress in Surface Science, 2013. **88**(2): p. 132-159.
10. Liu, H., Y. Liu, and D. Zhu, *Chemical doping of graphene.* Journal of Materials Chemistry, 2011. **21**(10): p. 3335-3345.
11. Garnica, M., et al., *Long-range magnetic order in a purely organic 2D layer adsorbed on epitaxial graphene.* Nat Phys, 2013. **9**(6): p. 368-374.
12. Mao, J., et al., *Tunability of Supramolecular Kagome Lattices of Magnetic Phthalocyanines Using Graphene-Based Moiré Patterns as Templates.* Journal of the American Chemical Society, 2009. **131**(40): p. 14136-14137.
13. Järvinen, P., et al., *Molecular Self-Assembly on Graphene on SiO2 and h-BN Substrates.* Nano Letters, 2013. **13**(7): p. 3199-3204.
14. Riss, A., et al., *Imaging and Tuning Molecular Levels at the Surface of a Gated Graphene Device.* ACS Nano, 2014. **8**(6): p. 5395-5401.
15. Wallace, P.R., *The Band Theory of Graphite.* Physical Review, 1947. **71**(9): p. 622-634.
16. Novoselov, K.S., et al., *Electric Field Effect in Atomically Thin Carbon Films.* Science, 2004. **306**(5696): p. 666-669.
17. Castro Neto, A.H., et al., *The electronic properties of graphene.* Reviews of Modern Physics, 2009. **81**(1): p. 109-162.
18. R Saito , G.D., M S Dresselhaus *Physical Properties of Carbon Nanotubes*. 1998: Imperial College Press.
19. Perelomov, A.M. and V.S. Popov, *"Fall to the center" in quantum mechanics.* Theoretical and Mathematical Physics, 1970. **4**(1): p. 664-677.

20. Popov, V., *COLLAPSE TO CENTER AT Z GREATER THAN 137 AND CRITICAL NUCLEAR CHARGE.* SOVIET JOURNAL OF NUCLEAR PHYSICS-USSR, 1971. **12**(2): p. 235.
21. Zeldovich, Y.B. and V.S. Popov, *Electronic structure of superheavy atoms.* Physics-Uspekhi, 1972. **14**(6): p. 673-694.
22. Shytov, A.V., M.I. Katsnelson, and L.S. Levitov, *Vacuum Polarization and Screening of Supercritical Impurities in Graphene.* Physical Review Letters, 2007. **99**(23): p. 236801.
23. Pereira, V.M., J. Nilsson, and A.H. Castro Neto, *Coulomb Impurity Problem in Graphene.* Physical Review Letters, 2007. **99**(16): p. 166802.
24. Binnig, G., et al., *Tunneling through a controllable vacuum gap.* Applied Physics Letters, 1982. **40**(2): p. 178-180.
25. Binnig, G., et al., *Surface Studies by Scanning Tunneling Microscopy.* Physical Review Letters, 1982. **49**(1): p. 57-61.
26. Bardeen, J., *Tunnelling from a Many-Particle Point of View.* Physical Review Letters, 1961. **6**(2): p. 57-59.
27. Tersoff, J. and D.R. Hamann, *Theory of the scanning tunneling microscope.* Physical Review B, 1985. **31**(2): p. 805-813.
28. Chen., C.J., *Introduction to Scanning Tunneling Microscopy*. 2nd edition. ed. 2008: Oxford University Press.
29. Yamachika, R.T., *Probing atomic-scale properties of organic and organometallic molecules by scanning tunneling spectroscopy*. 2009, University of California, Berkeley.
30. Binnig, G., C.F. Quate, and C. Gerber, *Atomic Force Microscope.* Physical Review Letters, 1986. **56**(9): p. 930-933.
31. Giessibl, F.J., *High-speed force sensor for force microscopy and profilometry utilizing a quartz tuning fork.* Applied Physics Letters, 1998. **73**(26): p. 3956-3958.
32. Giessibl, F.J., et al., *Subatomic Features on the Silicon (111)-(7×7) Surface Observed by Atomic Force Microscopy.* Science, 2000. **289**(5478): p. 422-425.
33. Gross, L., et al., *The Chemical Structure of a Molecule Resolved by Atomic Force Microscopy.* Science, 2009. **325**(5944): p. 1110-1114.
34. Emmrich, M., et al., *Subatomic resolution force microscopy reveals internal structure and adsorption sites of small iron clusters.* Science, 2015. **348**(6232): p. 308-311.
35. Brar, V.W., et al., *Gate-controlled ionization and screening of cobalt adatoms on a graphene surface.* Nat Phys, 2011. **7**(1): p. 43-47.
36. Zhang, Y., et al., *Giant phonon-induced conductance in scanning tunnelling spectroscopy of gate-tunable graphene.* Nat Phys, 2008. **4**(8): p. 627-630.
37. Wehling, T.O., et al., *Phonon-Mediated Tunneling into Graphene.* Physical Review Letters, 2008. **101**(21): p. 216803.
38. Jung, H.S., et al., *Fabrication of Gate-tunable Graphene Devices for Scanning Tunneling Microscopy Studies with Coulomb Impurities.* JoVE (Journal of Visualized Experiments), 2015(101): p. e52711-e52711.
39. Xue, J., et al., *Scanning tunnelling microscopy and spectroscopy of ultra-flat graphene on hexagonal boron nitride.* 2011. **10**: p. 282.

40. Decker, R., et al., *Local Electronic Properties of Graphene on a BN Substrate via Scanning Tunneling Microscopy.* Nano Letters, 2011. **11**(6): p. 2291-2295.
41. Yan, Z., et al., *Toward the Synthesis of Wafer-Scale Single-Crystal Graphene on Copper Foils.* ACS Nano, 2012. **6**(10): p. 9110-9117.
42. Zhang, B., et al., *Low-Temperature Chemical Vapor Deposition Growth of Graphene from Toluene on Electropolished Copper Foils.* ACS Nano, 2012. **6**(3): p. 2471-2476.
43. Li, X., et al., *Large-Area Synthesis of High-Quality and Uniform Graphene Films on Copper Foils.* Science, 2009. **324**(5932): p. 1312-1314.
44. Zhang, Y., L. Zhang, and C. Zhou, *Review of Chemical Vapor Deposition of Graphene and Related Applications.* Accounts of Chemical Research, 2013. **46**(10): p. 2329-2339.
45. Ishigami, M., et al., *Atomic Structure of Graphene on SiO2.* Nano Letters, 2007. **7**(6): p. 1643-1648.
46. Reina, A., et al., *Transferring and Identification of Single- and Few-Layer Graphene on Arbitrary Substrates.* The Journal of Physical Chemistry C, 2008. **112**(46): p. 17741-17744.
47. Suk, J.W., et al., *Transfer of CVD-Grown Monolayer Graphene onto Arbitrary Substrates.* ACS Nano, 2011. **5**(9): p. 6916-6924.
48. Regan, W., et al., *A direct transfer of layer-area graphene.* Applied Physics Letters, 2010. **96**(11): p. 113102.
49. Dan, Y., et al., *Intrinsic Response of Graphene Vapor Sensors.* Nano Letters, 2009. **9**(4): p. 1472-1475.
50. Wang, Y., et al., *Mapping Dirac quasiparticles near a single Coulomb impurity on graphene.* Nat Phys, 2012. **8**(9): p. 653-657.
51. Saito, R., et al., *Raman spectroscopy of graphene and carbon nanotubes.* Advances in Physics, 2011. **60**(3): p. 413-550.
52. Novoselov, K.S., et al., *Two-dimensional gas of massless Dirac fermions in graphene.* Nature, 2005. **438**(7065): p. 197-200.
53. Biswas, R.R., S. Sachdev, and D.T. Son, *Coulomb impurity in graphene.* Physical Review B, 2007. **76**(20): p. 205122.
54. Novikov, D.S., *Elastic scattering theory and transport in graphene.* Physical Review B, 2007. **76**(24): p. 245435.
55. Schedin, F., et al., *Detection of individual gas molecules adsorbed on graphene.* 2007. **6**: p. 652.
56. Sojoudi, H., et al., *Creating Graphene p–n Junctions Using Self-Assembled Monolayers.* ACS Applied Materials & Interfaces, 2012. **4**(9): p. 4781-4786.
57. Peimyoo, N., et al., *Photocontrolled Molecular Structural Transition and Doping in Graphene.* ACS Nano, 2012. **6**(10): p. 8878-8886.
58. Lee, B., et al., *Modification of Electronic Properties of Graphene with Self-Assembled Monolayers.* Nano Letters, 2010. **10**(7): p. 2427-2432.
59. Kim, M., et al., *Light-Driven Reversible Modulation of Doping in Graphene.* Nano Letters, 2012. **12**(1): p. 182-187.

60. Georgakilas, V., et al., *Functionalization of Graphene: Covalent and Non-Covalent Approaches, Derivatives and Applications.* Chemical Reviews, 2012. **112**(11): p. 6156-6214.
61. Coletti, C., et al., *Charge neutrality and band-gap tuning of epitaxial graphene on SiC by molecular doping.* Physical Review B, 2010. **81**(23): p. 235401.
62. Zhang, Z., et al., *Tailoring Electronic Properties of Graphene by π–π Stacking with Aromatic Molecules.* The Journal of Physical Chemistry Letters, 2011. **2**(22): p. 2897-2905.
63. Wei, P., et al., *Tuning the Dirac Point in CVD-Grown Graphene through Solution Processed n-Type Doping with 2-(2-Methoxyphenyl)-1,3-dimethyl-2,3-dihydro-1H-benzoimidazole.* Nano Letters, 2013. **13**(5): p. 1890-1897.
64. Wang, X., et al., *Quantitative Analysis of Graphene Doping by Organic Molecular Charge Transfer.* The Journal of Physical Chemistry C, 2011. **115**(15): p. 7596-7602.
65. Jobst, J., et al., *Transport properties of high-quality epitaxial graphene on 6H-SiC(0001).* Solid State Communications, 2011. **151**(16): p. 1061-1064.
66. Tadich, A., et al., *Tuning the charge carriers in epitaxial graphene on SiC(0001) from electron to hole via molecular doping with C60F48.* Applied Physics Letters, 2013. **102**(24): p. 241601.
67. Choi, J., et al., *Chemical Doping of Epitaxial Graphene by Organic Free Radicals.* The Journal of Physical Chemistry Letters, 2010. **1**(2): p. 505-509.
68. Yang, H., et al., *STM imaging, spectroscopy and manipulation of a self-assembled PTCDI monolayer on epitaxial graphene.* Physical Chemistry Chemical Physics, 2013. **15**(14): p. 4939-4946.
69. Loh, K.P., et al., *The chemistry of graphene.* Journal of Materials Chemistry, 2010. **20**(12): p. 2277-2289.
70. Yan, L., et al., *Chemistry and physics of a single atomic layer: strategies and challenges for functionalization of graphene and graphene-based materials.* Chemical Society Reviews, 2012. **41**(1): p. 97-114.
71. Chen, W., et al., *Surface Transfer p-Type Doping of Epitaxial Graphene.* Journal of the American Chemical Society, 2007. **129**(34): p. 10418-10422.
72. Nair, R.R., et al., *Dual origin of defect magnetism in graphene and its reversible switching by molecular doping.* 2013. **4**: p. 2010.
73. Ling, X., et al., *Probing the Effect of Molecular Orientation on the Intensity of Chemical Enhancement Using Graphene-Enhanced Raman Spectroscopy.* Small, 2012. **8**(9): p. 1365-1372.
74. Liu, J., J. Tang, and J.J. Gooding, *Strategies for chemical modification of graphene and applications of chemically modified graphene.* Journal of Materials Chemistry, 2012. **22**(25): p. 12435-12452.
75. Zhao, X., et al., *Nonlinear optical and optical limiting properties of graphene hybrids covalently functionalized by phthalocyanine.* Chemical Physics Letters, 2013. **577**(Supplement C): p. 62-67.
76. Xue, T., et al., *Graphene-Supported Hemin as a Highly Active Biomimetic Oxidation Catalyst.* Angewandte Chemie International Edition, 2012. **51**(16): p. 3822-3825.

77. Wang, Q.H., et al., *Understanding and controlling the substrate effect on graphene electron-transfer chemistry via reactivity imprint lithography.* 2012. **4**: p. 724.
78. Xiao, K., et al., *Surface-Induced Orientation Control of CuPc Molecules for the Epitaxial Growth of Highly Ordered Organic Crystals on Graphene.* Journal of the American Chemical Society, 2013. **135**(9): p. 3680-3687.
79. Wang, Q.H. and M.C. Hersam, *Room-temperature molecular-resolution characterization of self-assembled organic monolayers on epitaxial graphene.* 2009. **1**: p. 206.
80. Huang, H., et al., *Structural and Electronic Properties of PTCDA Thin Films on Epitaxial Graphene.* ACS Nano, 2009. **3**(11): p. 3431-3436.
81. Lauffer, P., et al., *Molecular and electronic structure of PTCDA on bilayer graphene on SiC(0001) studied with scanning tunneling microscopy.* physica status solidi (b), 2008. **245**(10): p. 2064-2067.
82. Hossain, M.Z., M.A. Walsh, and M.C. Hersam, *Scanning Tunneling Microscopy, Spectroscopy, and Nanolithography of Epitaxial Graphene Chemically Modified with Aryl Moieties.* Journal of the American Chemical Society, 2010. **132**(43): p. 15399-15403.
83. Wang, Y.-L., et al., *Selective adsorption and electronic interaction of F16CuPc on epitaxial graphene.* Physical Review B, 2010. **82**(24): p. 245420.
84. Ying Mao, H., et al., *Chemical vapor deposition graphene as structural template to control interfacial molecular orientation of chloroaluminium phthalocyanine.* Applied Physics Letters, 2011. **99**(9): p. 093301.
85. Zhou, S.Y., et al., *Metal to Insulator Transition in Epitaxial Graphene Induced by Molecular Doping.* Physical Review Letters, 2008. **101**(8): p. 086402.
86. Brar, V.W., et al., *Observation of Carrier-Density-Dependent Many-Body Effects in Graphene via Tunneling Spectroscopy.* Physical Review Letters, 2010. **104**(3): p. 036805.
87. Grimme, S., *Semiempirical GGA-type density functional constructed with a long-range dispersion correction.* Journal of Computational Chemistry, 2006. **27**(15): p. 1787-1799.
88. Barone, V., et al., *Role and effective treatment of dispersive forces in materials: Polyethylene and graphite crystals as test cases.* Journal of Computational Chemistry, 2009. **30**(6): p. 934-939.
89. Qiu, X.H., G.V. Nazin, and W. Ho, *Vibronic States in Single Molecule Electron Transport.* Physical Review Letters, 2004. **92**(20): p. 206102.
90. Pavliček, N., et al., *Symmetry Dependence of Vibration-Assisted Tunneling.* Physical Review Letters, 2013. **110**(13): p. 136101.
91. Wang, S., et al., *Vibronic state assisted resonant transport in molecules strongly anchored at an electrode.* Physical Review B, 2011. **83**(11): p. 115431.
92. Wickenburg, S., et al., *Tuning charge and correlation effects for a single molecule on a graphene device.* 2016. **7**: p. 13553.
93. Aviram, A. and M.A. Ratner, *Molecular rectifiers.* Chemical Physics Letters, 1974. **29**(2): p. 277-283.
94. Tao, N.J., *Electron transport in molecular junctions.* Nat Nano, 2006. **1**(3): p. 173-181.

95. Sun, L., et al., *Single-molecule electronics: from chemical design to functional devices.* Chemical Society Reviews, 2014. **43**(21): p. 7378-7411.
96. Aradhya, S.V. and L. Venkataraman, *Single-molecule junctions beyond electronic transport.* Nat Nano, 2013. **8**(6): p. 399-410.
97. McCreery, R.L. and A.J. Bergren, *Progress with Molecular Electronic Junctions: Meeting Experimental Challenges in Design and Fabrication.* Advanced Materials, 2009. **21**(43): p. 4303-4322.
98. Perrin, M.L., E. Burzuri, and H.S.J. van der Zant, *Single-molecule transistors.* Chemical Society Reviews, 2015. **44**(4): p. 902-919.
99. Moth-Poulsen, K. and T. Bjornholm, *Molecular electronics with single molecules in solid-state devices.* Nat Nano, 2009. **4**(9): p. 551-556.
100. Joachim, C., J.K. Gimzewski, and A. Aviram, *Electronics using hybrid-molecular and mono-molecular devices.* Nature, 2000. **408**(6812): p. 541-548.
101. Jia, C., et al., *Covalently bonded single-molecule junctions with stable and reversible photoswitched conductivity.* Science, 2016. **352**(6292): p. 1443-1445.
102. Liang, W., et al., *Kondo resonance in a single-molecule transistor.* Nature, 2002. **417**(6890): p. 725-729.
103. Haiss, W., et al., *Precision control of single-molecule electrical junctions.* Nat Mater, 2006. **5**(12): p. 995-1002.
104. Martinez-Blanco, J., et al., *Gating a single-molecule transistor with individual atoms.* Nat Phys, 2015. **11**(8): p. 640-644.
105. Perrin, M.L., et al., *Large tunable image-charge effects in single-molecule junctions.* Nat Nano, 2013. **8**(4): p. 282-287.
106. Reed, M.A., et al., *Conductance of a Molecular Junction.* Science, 1997. **278**(5336): p. 252-254.
107. Xu, B. and N.J. Tao, *Measurement of Single-Molecule Resistance by Repeated Formation of Molecular Junctions.* Science, 2003. **301**(5637): p. 1221-1223.
108. Park, H., et al., *Nanomechanical oscillations in a single-C60 transistor.* Nature, 2000. **407**(6800): p. 57-60.
109. Song, H., et al., *Observation of molecular orbital gating.* Nature, 2009. **462**(7276): p. 1039-1043.
110. Schull, G., et al., *Atomic-scale engineering of electrodes for single-molecule contacts.* Nat Nano, 2011. **6**(1): p. 23-27.
111. Cui, X.D., et al., *Reproducible Measurement of Single-Molecule Conductivity.* Science, 2001. **294**(5542): p. 571-574.
112. Yamachika, R., et al., *Controlled Atomic Doping of a Single C60 Molecule.* Science, 2004. **304**(5668): p. 281-284.
113. Fernández-Torrente, I., et al., *Gating the Charge State of Single Molecules by Local Electric Fields.* Physical Review Letters, 2012. **108**(3): p. 036801.
114. Lee, D.H. and J.A. Gupta, *Tunable Field Control Over the Binding Energy of Single Dopants by a Charged Vacancy in GaAs.* Science, 2010. **330**(6012): p. 1807-1810.
115. Pinto, H., et al., *p-type doping of graphene with F4-TCNQ.* Journal of Physics: Condensed Matter, 2009. **21**(40): p. 402001.

116. Stradi, D., et al., *Controlling the spatial arrangement of organic magnetic anions adsorbed on epitaxial graphene on Ru(0001).* Nanoscale, 2014. **6**(24): p. 15271-15279.
117. Barja, S., et al., *Self-organization of electron acceptor molecules on graphene.* Chemical Communications, 2010. **46**(43): p. 8198-8200.
118. Chi, M. and Y.-P. Zhao, *First principle study of the interaction and charge transfer between graphene and organic molecules.* Computational Materials Science, 2012. **56**: p. 79-84.
119. Sun, J.T., et al., *Linear tuning of charge carriers in graphene by organic molecules and charge-transfer complexes.* Physical Review B, 2010. **81**(15): p. 155403.
120. Alaboson, J.M.P., et al., *Templating Sub-10 nm Atomic Layer Deposited Oxide Nanostructures on Graphene via One-Dimensional Organic Self-Assembled Monolayers.* Nano Letters, 2013. **13**(12): p. 5763-5770.
121. de Oteyza, D.G., et al., *Direct Imaging of Covalent Bond Structure in Single-Molecule Chemical Reactions.* Science, 2013. **340**(6139): p. 1434-1437.
122. Gross, L., et al., *Organic structure determination using atomic-resolution scanning probe microscopy.* Nat Chem, 2010. **2**(10): p. 821-825.
123. Gross, L., et al., *Bond-Order Discrimination by Atomic Force Microscopy.* Science, 2012. **337**(6100): p. 1326-1329.
124. Hapala, P., et al., *Mechanism of high-resolution STM/AFM imaging with functionalized tips.* Physical Review B, 2014. **90**(8): p. 085421.
125. Hämäläinen, S.K., et al., *Intermolecular Contrast in Atomic Force Microscopy Images without Intermolecular Bonds.* Physical Review Letters, 2014. **113**(18): p. 186102.
126. Zhang, J., et al., *Real-Space Identification of Intermolecular Bonding with Atomic Force Microscopy.* Science, 2013. **342**(6158): p. 611-614.
127. Marczinowski, F., et al., *Effect of charge manipulation on scanning tunneling spectra of single Mn acceptors in InAs.* Physical Review B, 2008. **77**(11): p. 115318.
128. Nazin, G.V., X.H. Qiu, and W. Ho, *Charging and Interaction of Individual Impurities in a Monolayer Organic Crystal.* Physical Review Letters, 2005. **95**(16): p. 166103.
129. Story, S.M., et al., *Cumulant expansion for phonon contributions to the electron spectral function.* Physical Review B, 2014. **90**(19): p. 195135.
130. Wu, S.W., et al., *Control of Relative Tunneling Rates in Single Molecule Bipolar Electron Transport.* Physical Review Letters, 2004. **93**(23): p. 236802.
131. Neaton, J.B., M.S. Hybertsen, and S.G. Louie, *Renormalization of Molecular Electronic Levels at Metal-Molecule Interfaces.* Physical Review Letters, 2006. **97**(21): p. 216405.
132. Torrente, I.F., K.J. Franke, and J.I. Pascual, *Spectroscopy of C 60 single molecules: the role of screening on energy level alignment.* Journal of Physics: Condensed Matter, 2008. **20**(18): p. 184001.
133. Kubatkin, S., et al., *Single-electron transistor of a single organic molecule with access to several redox states.* Nature, 2003. **425**(6959): p. 698-701.
134. Novikov, D.S., *Numbers of donors and acceptors from transport measurements in graphene.* Applied Physics Letters, 2007. **91**(10): p. 102102.
135. Chen, J.H., et al., *Charged-impurity scattering in graphene.* Nat Phys, 2008. **4**(5): p. 377-381.

136. Katsnelson, M.I., *Nonlinear screening of charge impurities in graphene.* Physical Review B, 2006. **74**(20): p. 201401.
137. Ando, T., *Screening Effect and Impurity Scattering in Monolayer Graphene.* Journal of the Physical Society of Japan, 2006. **75**(7): p. 074716.
138. Hwang, E.H. and S. Das Sarma, *Dielectric function, screening, and plasmons in two-dimensional graphene.* Physical Review B, 2007. **75**(20): p. 205418.
139. Kotov, V.N., et al., *Electron-Electron Interactions in Graphene: Current Status and Perspectives.* Reviews of Modern Physics, 2012. **84**(3): p. 1067-1125.
140. Popov, V., *Position Production in a Coulomb Field with Z= 137.* Soviet Journal of Experimental and Theoretical Physics, 1971. **32**.
141. W. Greiner, B.M., and J. Rafelski, *Quantum Electrodynamics of Strong Fields*. 2nd ed. 1985, Berlin, Heidelberg: Springer Berlin Heidelberg.
142. Pradhan, N.A., et al., *Atomic Scale Conductance Induced by Single Impurity Charging.* Physical Review Letters, 2005. **94**(7): p. 076801.
143. Gamayun, O.V., E.V. Gorbar, and V.P. Gusynin, *Supercritical Coulomb center and excitonic instability in graphene.* Physical Review B, 2009. **80**(16): p. 165429.
144. Boyer, T.H., *Unfamiliar trajectories for a relativistic particle in a Kepler or Coulomb potential.* American Journal of Physics, 2004. **72**(8): p. 992-997.
145. Terekhov, I.S., et al., *Screening of Coulomb Impurities in Graphene.* Physical Review Letters, 2008. **100**(7): p. 076803.
146. Hong, G., et al., *Recent progress in organic molecule/graphene interfaces.* Nano Today, 2013. **8**(4): p. 388-402.
147. MacLeod, J.M. and F. Rosei, *Molecular Self-Assembly on Graphene.* Small, 2014. **10**(6): p. 1038-1049.
148. Mali, K.S., et al., *Nanostructuring graphene for controlled and reproducible functionalization.* Nanoscale, 2015. **7**(5): p. 1566-1585.
149. Song, J., et al., *A general method for transferring graphene onto soft surfaces.* Nat Nano, 2013. **8**(5): p. 356-362.
150. Schuler, B., et al., *Adsorption Geometry Determination of Single Molecules by Atomic Force Microscopy.* Physical Review Letters, 2013. **111**(10): p. 106103.
151. Emge, T.J., et al., *Solution and Solid State Studies of Tetrafluoro-7,7,8,8-Tetracyano-p-Quinodimethane, TCNQF4. Evidence for Long-Range Amphoteric Intermolecular Interactions and Low-Dimensionality in the Solid State Structure.* Molecular Crystals and Liquid Crystals, 1981. **65**(3-4): p. 161-178.
152. Goetz, K.P., et al., *Freezing-in orientational disorder induces crossover from thermally-activated to temperature-independent transport in organic semiconductors.* 2014. **5**: p. 5642.
153. Ishii, H., et al., *Energy Level Alignment and Interfacial Electronic Structures at Organic/Metal and Organic/Organic Interfaces.* Advanced Materials, 1999. **11**(8): p. 605-625.
154. Xu, Y., et al., *Space-Charge Transfer in Hybrid Inorganic-Organic Systems.* Physical Review Letters, 2013. **111**(22): p. 226802.

155. Ashcroft, N.W.M., N. D., *Solid State Physics*. 1976, Brooks/Cole, Cengage Learning. p. 354.
156. Natan, A., et al., *Electrostatic Properties of Ideal and Non-ideal Polar Organic Monolayers: Implications for Electronic Devices.* Advanced Materials, 2007. **19**(23): p. 4103-4117.
157. Chen, Z., et al., *Physical Adsorption and Charge Transfer of Molecular Br2 on Graphene.* ACS Nano, 2014. **8**(3): p. 2943-2950.